To the Graduate Council:

I am submitting herewith a dissertation by Zhiying Zhang entitled "Elastic properties of bulk-metallic glasses studied by resonant ultrasound spectroscopy". I have examined the final electronic copy of this dissertation for form and content and recommend that it be accepted in partial fulfillment of the requirements for the degree of Doctor of Philosophy, with a major in Materials Science and Engineering.

Veerle Keppens

Major Professor

We have read this dissertation

And recommend its acceptance:

Takeshi Egami

Peter K. Liaw

James R. Thompson

Accepted for the Council:

Carolyn R. Hodges,

Vice Provost and Dean of the Graduate School

(Original signatures are on file with official student records.)

ELASTIC PROPERTIES OF BULK-METALLIC GLASSES STUDIED BY RESONANT ULTRASOUND SPECTROSCOPY

A Dissertation

Presented for the

Doctor of Philosophy

Degree

The University of Tennessee, Knoxville

Zhiying Zhang

August 2008

DEDICATION

This dissertation is dedicated to my father Qiusheng Zhou, my mother Xiangjiao Hu, my sister Lanfang Zhang and the rest of my family for their support.

ACKNOWLEDGEMENTS

First of all, I would like to thank my advisor Dr. Veerle Keppens for the guidance and help throughout my Ph. D. study. What I learned from her will benefit my whole life. It is my honor to have Dr. Takeshi Egami, Dr. Peter K. Liaw and Dr. James R. Thompson on my Ph. D. committee. I would like to thank them for their valuable advice and help.

I would like to thank Mr. Girish Upreti, Dr. Raphael P. Hermann, Dr. Sriparna Bhatracharya, Ms. Yanbing Luan, Mr. Michael Koehler, Mr. Tim Cagle, Mr. Ben Davis, Mr. Christ Agee and Mr. David McCarthy for the help with analyzing the data, maintaining the equipments and making my Ph. D. study easier. It is a great pleasure to be in the same group as them.

I would like to thank Dr. Yoshihiko Yokoyama and Dr. Akihisa Inoue from Tohoku University, Dr. Oleg N. Senkov from UES Inc., Dr. Daniel B. Miracle from Air Force Research Laboratory, Dr. Joseph Poon from University of Virginia, Dr. Chain T. Liu, Ms. Lu Huang, Ms. Dongchun Qiao, Dr. Mark Morrison, Ms. Bandice Green, Mr. Feng Jiang, Dr. Gongyao Wang, Mr. Andrew Chuang, Dr. Guojiang Fan, and Dr. Cang Fan for providing samples for my research. I also benefit a lot from the discussions with them.

I would like to thank Dr. Josh Gladden and Mr. Guangyan Li from University of Mississippi for the help with the high temperature measurement of elastic constants. Dr. Yandong Wang and Mr. Feng Jiang have kindly done the experiments of high energy synchrotron X-ray diffraction, which provides valuable support for my research. I would like to thank Ms. Dongchun Qiao and Mr. Jiawan Tian for the help with differential scanning calorimetry.

At last, I would like to thank Dr. David G. Mandrus and Dr. Rongying Jin from Oak Ridge National Laboratory, and Dr. Shiliang Li for the help with maintaining the physical property measurement system.

ABSTRACT

The elastic properties of a solid are of considerable interest to both science and technology. Not only do they contain fundamental information about the nature of the inter-atomic bonding in the material, but they also determine the mechanical behavior of solids. In the past few years, considerable effort has been devoted to the study of elastic properties of bulk metallic glasses (BMGs), a relatively new class of metallic materials that display a unique combination of mechanical and physical properties. Our research has focused on Zr-based, Cu-based and Ca-based metallic glasses. Zr-based BMGs are known to have superior glass forming ability and high strength, but their ductility is too low for wide-spread practical applications. Cu-based BMGs recently received wide interest because of their low cost and good mechanical properties. Ca-based BMGs have low glass transition temperature T_g, around 390 K, which make them very attractive to be studied near T_g.

In this work, resonant ultrasound spectroscopy (RUS) has been applied to study the elastic properties of above mentioned BMGs from 5 K to their glass transition temperature T_g. RUS is a novel technique for determining the elastic moduli of solids, based on the measurement of the resonances of a freely vibrating body. In an RUS experiment, the mechanical resonances of a freely vibrating solid of known shape are measured, and an iteration procedure is used to "match" the measured lines with the calculated spectrum. This allows determination of all elastic constant of the solid from a single frequency scan.

Below T_g, the elastic constants of the BMGs under investigation show "normal" behavior, i.e. with increasing temperature, all moduli decrease and Poisson ratio increases. Above T_g changes in the trends occur due to structural relaxation and crystallization. We confirmed the suggested link between ductility and Poisson ratio: BMGs showing good ductility display high Poisson ratio. By increasing palladium content in $Zr_{50}Cu_{40-x}Al_{10}Pd_x$ alloys, BMGs with high Poisson ratio and thus good ductility have been obtained. In addition, we developed a simple model to provide fast and good estimate of the

temperature dependence of elastic constants of BMGs from room temperature measurements.

Keywords: Elastic properties; Bulk metallic glasses (BMGs); Resonant ultrasound spectroscopy (RUS); Internal friction.

TABLE OF CONTENTS

Introduction 1
1. Literature Review 3
1.1 Development of BMGs 3
1.2 Glass Forming Ability 5
1.3 Elastic Properties of BMGs 15
1.3.1 Effects of temperature, pressure and composition on elastic properties 16
1.3.2 Relationship between elastic constants and mechanical properties 21
1.3.3 Correlation of elastic constants with T_g and GFA 26
1.3.4 The physics of elastic properties 33
2. Experimental Details 37
3. Zirconium Based and Copper Based Bulk Metallic Glasses 47
3.1 Zr-Based BMGs 48
3.1.1 ZrCuAl and ZrCuAlNi (Ta, Y, Ti) BMGs 48
3.1.2 ZrCuAlPd BMGs 52
3.2 Cu-Based BMGs 64
4. Calcium Based Bulk Metallic Glasses 70
5. Model to Predict the Temperature Dependence of Elastic Moduli 80
6. Correlation with Other Work and Perspectives for Future Work 86
Conclusions 90
Bibliography 92
Vita 105

LIST OF TABLES

Table 1.1: Application fields for BMGs (Inoue, 2000) (Wang, 2004 c)……6

Table 3.1: Glass transition temperature T_g, crystallization temperature T_x, liquidus temperature T_l, supercooled liquid region ΔT_x, reduced glass transition temperature T_{rg}, Hruby factor K_{gl}, γ and γ_m of Zr-based BMGs…..……..49

Table 3.2: Room temperature elastic constants for various Zr-based BMGs……..…….51

Table 3.3: Density ρ, shear modulus G, longitudinal modulus L, bulk modulus B, Young's modulus E, Poisson ratio ν and Debye temperature θ_D of $Zr_{50}Cu_{40-x}Al_{10}Pd_x$ (x=0, 1, 2, 3, 5, 6, 7, 9, 12 and 15 at.%) alloys……57

Table 3.4: Density and elastic moduli of the elements Zr, Cu, Al and Pd (http://www.webelements.com/webelements/elements/).....58

Table 3.5: Glass transition temperature T_g, crystallization temperature T_x, liquidus temperature T_l, supercooled liquid region ΔT_x, reduced glass transition temperature T_{rg}, Hruby factor K_{gl}, γ and γ_m of Cu-based BMGs……..66

Table 3.6: Density and room temperature elastic constants for various Cu-based BMGs……...…….……66

Table 4.1: Glass transition temperature T_g, crystallization temperature T_x, liquidus temperature T_l, supercooled liquid region ΔT_x, reduced glass transition temperature T_{rg}, Hruby factor K_{gl}, γ, γ_m, and critical casting thickness d_{max} for Ca-based BMGs, determined by differential scanning calorimetry (DSC) with the heating rate at 0.667 K/s…….……..……..71

Table 4.2: Dependence of glass transition temperature T_g and crystallization temperature T_x on the heating rate for $Ca_{65}Mg_{15}Zn_{20}$…….……..74

Table 4.3: Atomic volume, V_A, density, ρ and elastic constants of elements (http://www.webelements.com/webelements/elements/).....75

Table 4.4: Comparison of measured elastic constants (meas.) at room temperature with the calculated values based on atomic fraction ($cal_{at.}$) and volume fraction ($cal_{vol.}$) of components……..……..……..75

Table 4.5: Density and room temperature elastic constants for various Ca-based BMGs……78
Table 5.1: Averaged melting temperature T_m, density ρ, shear modulus at room temperature $G(T_{RT})$, bulk modulus at room temperature $B(T_{RT})$, Debye temperature θ_D, s_G and s_B for Zr-based, Cu-based and Ca-based BMGs…….82
Table 6.1: Fracture strength, fatigue limit and Vickers hardness of Zr-based, Cu-based and Ca-based BMGs……..……86

LIST OF FIGURES

Figure 1.1: Evolution of the critical casting thickness for bulk metallic glasses over the past forty years (Loffler, 2003)……..……..……5

Figure1.2: Relation among the critical cooling rate R_c, maximum sample thickness t_{max} and supercooled liquid region ΔT_x for typical bulk glassy alloys (Inoue, 1999)……..……8

Figure 1.3: Scaled viscosity data for glass-forming liquids showing range of behavior from "strong" characteristic of open tetrahedral network liquids, to "fragile" typical of ionic and molecular liquids. ZBLA is $(ZrF_4)_{0.53}(BaF_2)_{0.20}(LaF_3)_{0.04}(AlF_3)_{0.03}(NaF)_{0.20}$ (Angell, 1985)…....……10

Figure 1.4: Angell plot of the viscosities of Mg-based, Zr-based BMGs and several nonmetallic glasses (Busch, 1998)……..……..……11

Figure 1.5: Correlation of the inverse of the critical cooling rate R_c^{-1} with the fragility parameter D (Tanaka, 2005)……..……..11

Figure 1.6: The calculated difference in the Gibbs free energy between the liquid and the crystalline states for a number of glass forming alloys (Glade, 2000)...……12

Figure 1.7: Correlation between parameter γ and critical cooling rate R_c for representative metallic glasses (Lu, 2002)……..…..……..13

Figure 1.8: Dependence of the glass forming ability parameter F_1 on the fragility index m at three different T_{rg} values (Senkov, 2007)……..……..14

Figure 1.9: Correlation between the critical cooling rate R_c and the glass forming ability parameter F_1 for several glass forming systems. Solid circles correspond to the bulk metallic glasses and open diamonds correspond to the nonmetallic glasses (Senkov, 2007)……..……..15

Figure 1.10: Dependence of shear modulus G and Debye temperature θ_D on annealing temperature (Wang, 2000)……..……16

Figure 1.11: Changes in the elastic constants in the heating and cooling processes (Ichitsubo, 2003)……..……..17

Figure 1.12: Changes in the ultrasonic-attenuation coefficients in the heating and cooling processes (Ichitsubo, 2003)……..……18

Figure 1.13: Variation of elastic constants C of $Zr_{41}Ti_{14}Cu_{12.5}Ni_9Be_{22.5}C_1$ with pressure P. C is normalized by $(C-C_0)/C_0$, where C_0 is a normal modulus at ambient P_0 (Wang, 1999)……..……19
Figure 1.14: Dependence of Debye temperature on the pressure in $Zr_{41}Ti_{14}Cu_{12.5}Ni_9Be_{22.5}C_1$ (Wang, 1999)……...……19
Figure 1.15: Microhardness versus temperature for $Cu_{60}Zr_{20}Hf_{10}Ti_{10}$ BMG (Wesseling, 2004)……..……22
Figure 1.16: Fracture toughness or strength response to the plastic process zone size (Xi, 2005)…….…….……23
Figure 1.17: The correlation of fracture energy G_f with Poisson ratio ν for metallic glasses (as-cast and annealed) and oxide glasses (Lewandowski, 2005)...…24
Figure 1.18: Correlation of fracture strength σ and Vickers hardness H_v with Young's modulus E for various BMGs (Wang, 2005)……25
Figure 1.19: Relationship between mechanical properties of typical BMGs with Young's modulus E. (a) Tensile fracture strength vs. E; (b) Vickers hardness vs. E (Inoue, 2002)…….…….27
Figure 1.20: Experimental shear stress at yielding, τ_Y vs. shear modulus G at room temperature for ~30 bulk metallic glasses (Johnson, 2005)……..27
Figure 1.21: Glass transition temperature T_g multiplied by $k_B/(2BV)$ as a function of Poisson ratio for various metallic glasses. The solid line indicates $\frac{2(1-2\nu)(\varepsilon_v^{T,crit})^2}{3(1-\nu)}$ with $\varepsilon_v^{T,crit}$=0.095 (Egami, 2007)……...……29
Figure 1.22: Correlation between glass transition temperature T_g and Young's modulus E for various BMGs (Wang, 2005)…….……..29
Figure 1.23: The correlation of elastic constants with T_g and T_x for rare-earth based BMGs (Wang, 2006)……..……...……..30
Figure 1.24: Correlation of fragility with the ratio of the bulk and shear moduli in the glassy state (Novikov, 2004)……..……31
Figure 1.25: Correlation between fragility of liquids m and the ratio of instantaneous bulk to shear modulus B/G for metallic glasses (Wang, 2006)…...……..32

Figure 1.26: Correlation between fragility of liquids m and the ratio of instantaneous bulk to shear modulus *B/G* of respective glasses. Circles – data for nonmetallic glass formers. Triangles – data for metallic glass formers. Solid lines – linear fits (Novikov, 2006)……..32
Figure 1.27: Dependence of force *F* and potential energy *U* on interatomic distance r. (a) *F* vs. *r*. (b) *U* vs. *r* (Kittel, 1986) (Shelby, 1997)……..……..…….34
Figure 1.28: Schematic relationship between potential energy *U* and interatomic distance *r* at different temperatures (Mohazzabi, 1997)……...……..35
Figure 2.1: An illustration of several vibrational eigenmodes for a rectangular parallelepiped (Leisure, 1997)……..……38
Figure 2.2: Schematic setup of resonant ultrasound spectroscopy (Chu, 1995)……...….42
Figure 2.3: a typical RUS scan……..……43
Figure 2.4: RUS probe for corner-mounting…….……43
Figure 2.5: Schematic of the sample flat-mounted between the transducers……...…..44
Figure 2.6: RUS probe for flat-mounting…….……45
Figure 2.7: High temperature apparatus……45
Figure 3.1: Microstructures of $Zr_{63.8}Ni_{16.2}Cu_{15}Al_5$. (a) Scanning electron microscopy image of the etched as-cast microstructure with the inserted X-ray diffraction pattern. (b) and (c) Transmission electron microscopy bright-field image. (d) High resolution electron microscopy image of the interface marked in (c) (Du, 2007b)……..48
Figure 3.2: Shear modulus *G* as a function of temperature. (a) For two samples of $Zr_{50}Cu_{30}Ni_{10}Al_{10;}$ (b) For $Zr_{50}Cu_{30}Ni_{10}Al_{10}$ (□), $Zr_{50}Cu_{40}Al_{10}$ (◇), and $Zr_{52.5}Cu_{17.9}Ni_{14.6}Al_{10}Ti_5$ (△). The solid lines represent a fit using the Varshni model, with parameters *s*= 0.7 GPa and *t* = 100 K. c^0=36.0 GPa and 35.9 GPa for $Zr_{50}Cu_{30}Ni_{10}Al_{10}$, c^0=35.7 GPa for $Zr_{50}Cu_{40}Al_{10}$, and c^0=34.0 GPa for $Zr_{52.5}Cu_{17.9}Ni_{14.6}Al_{10}Ti_5$……..……..50
Figure 3.3: Longitudinal modulus *L*, bulk modulus *B* and Young's modulus *E* as a function of temperature for $Zr_{50}Cu_{30}Ni_{10}Al_{10}$ (□), $Zr_{50}Cu_{40}Al_{10}$ (◇), and $Zr_{52.5}Cu_{17.9}Ni_{14.6}Al_{10}Ti_5$ (△)……..…….……51

Figure 3.4: The ratio of bulk modulus to shear modulus *B/G* and the Poisson ratio ν as a function of temperature for $Zr_{50}Cu_{30}Ni_{10}Al_{10}$ (□), $Zr_{50}Cu_{40}Al_{10}$ (◇), and $Zr_{52.5}Cu_{17.9}Ni_{14.6}Al_{10}Ti_5$ (△)……53

Figure 3.5: Longitudinal modulus *L* and bulk modulus *B* as a function of temperature for $Zr_{59}Cu_{18}Al_{10}Ni_8Ta_5$ (▽), $Zr_{60}Cu_{30}Al_{10}$ (□), $Zr_{63.8}Ni_{16.2}Cu_{15}Al_5$ (O), $Zr_{65}Cu_{17.5}Ni_{10}Al_{7.5}$ (△)……53

Figure 3.6: Shear modulus *G* and Young's modulus *E* as a function of temperature for $Zr_{59}Cu_{18}Al_{10}Ni_8Ta_5$ (▽), $Zr_{60}Cu_{30}Al_{10}$ (□), $Zr_{63.8}Ni_{16.2}Cu_{15}Al_5$ (O) and $Zr_{65}Cu_{17.5}Ni_{10}Al_{7.5}$ (△)……54

Figure 3.7: Ratio of bulk modulus to shear modulus *B/G* and Poisson ratio ν as a function of temperature for $Zr_{59}Cu_{18}Al_{10}Ni_8Ta_5$ (▽), $Zr_{60}Cu_{30}Al_{10}$ (□), $Zr_{63.8}Ni_{16.2}Cu_{15}Al_5$ (O) and $Zr_{65}Cu_{17.5}Ni_{10}Al_{7.5}$ (△)……..54

Figure 3.8: Dependence of longitudinal modulus *L*, shear modulus *G* and Poisson ratio ν on the casting diameter of the samples for $Zr_{50}Cu_{40-x}Al_{10}Pd_x$ (x=0, 3, 6, 9, 12 and 15 at.%) alloys. Pd: 0 at.% (□), 3 at.% (O), 6 at.% (△), 9 at.% (▽), 12 at.% (◇) and 15 at.% (◁)……56

Figure 3.9: Dependence of bulk modulus *B* and Young's modulus *E* on the casting diameter of the samples for $Zr_{50}Cu_{40-x}Al_{10}Pd_x$ (x=0, 3, 6, 9, 12 and 15 at.%) alloys. Pd: 0 at.% (□), 3 at.% (O), 6 at.% (△), 9 at.% (▽), 12 at.% (◇) and 15 at.% (◁)……56

Figure 3.10: Dependence of longitudinal modulus *L*, bulk modulus *B* and Poisson ratio ν on the Pd content for $Zr_{50}Cu_{40-x}Al_{10}Pd_x$ alloys……57

Figure 3.11: Dependence of shear modulus *G* and Young's modulus *E* on the Pd content for $Zr_{50}Cu_{40-x}Al_{10}Pd_x$ alloys……58

Figure 3.12: Longitudinal modulus *L* as a function of temperature for $Zr_{50}Cu_{40-x}Al_{10}Pd_x$ BMGs……59

Figure 3.13: Shear modulus *G* as a function of temperature for $Zr_{50}Cu_{40-x}Al_{10}Pd_x$ BMGs……59

Figure 3.14: Bulk modulus *B* as a function of temperature for $Zr_{50}Cu_{40-x}Al_{10}Pd_x$ BMGs……60

Figure 3.15: Young's modulus E as a function of temperature for $Zr_{50}Cu_{40-x}Al_{10}Pd_x$ BMGs……60
Figure 3.16: Poisson ratio ν as a function of temperature for $Zr_{50}Cu_{40-x}Al_{10}Pd_x$ BMGs……..……..61
Figure 3.17: Temperature dependence of internal friction Q^{-1} for $Zr_{50}Cu_{40-x}Al_{10}Pd_x$ BMGs…….……62
Figure 3.18: Temperature dependence of shear modulus G, Young's modulus E and Poisson ratio ν of $Zr_{50}Cu_{25}Al_{10}Pd_{15}$ up to the glass transition temperature……...……63
Figure 3.19: Temperature dependence of longitudinal modulus L and bulk modulus B of $Zr_{50}Cu_{25}Al_{10}Pd_{15}$ up to the glass transition temperature……..……63
Figure 3.20: Diffraction image of $Zr_{50}Cu_{25}Al_{10}Pd_{15}$ using high energy Synchrotron X-ray diffraction. (a) as-cast sample (300 K). (b) heated sample (730 K) using the wavelength λ=0.0107480 nm. (Jiang, unpublished)…….……65
Figure 3.21: High energy Synchrotron X-ray diffraction of $Zr_{50}Cu_{25}Al_{10}Pd_{15}$ as-cast sample (300K) and heated sample (730 K) using the wavelength λ=0.0107480 nm. (Jiang, unpublished)……65
Figure 3.22: Longitudinal modulus L as a function of temperature for Cu-based BMGs $Cu_{53.9}Zr_{39.2}Al_{4.9}Er_2$ (■), $Cu_{47.5}Zr_{47.5}Al_5$ (●), $Cu_{47.5}Zr_{38}Hf_{9.5}Al_5$ (▲) and $Cu_{47}Zr_{47}Al_6$ (▼)……...……..67
Figure 3.23: Shear modulus G as a function of temperature for Cu-based BMGs $Cu_{53.9}Zr_{39.2}Al_{4.9}Er_2$ (■), $Cu_{47.5}Zr_{47.5}Al_5$ (●), $Cu_{47.5}Zr_{38}Hf_{9.5}Al_5$ (▲) and $Cu_{47}Zr_{47}Al_6$ (▼)……67
Figure 3.24: Bulk modulus B as a function of temperature for Cu-based BMGs $Cu_{53.9}Zr_{39.2}Al_{4.9}Er_2$ (■), $Cu_{47.5}Zr_{47.5}Al_5$ (●), $Cu_{47.5}Zr_{38}Hf_{9.5}Al_5$ (▲) and $Cu_{47}Zr_{47}Al_6$ (▼)…….……..……..68
Figure 3.25: Young's modulus E as a function of temperature for Cu-based BMGs $Cu_{53.9}Zr_{39.2}Al_{4.9}Er_2$ (■), $Cu_{47.5}Zr_{47.5}Al_5$ (●), $Cu_{47.5}Zr_{38}Hf_{9.5}Al_5$ (▲) and $Cu_{47}Zr_{47}Al_6$ (▼)……68

Figure 3.26: Poisson ratio ν as a function of temperature for Cu-based BMGs $Cu_{53.9}Zr_{39.2}Al_{4.9}Er_2$ (■), $Cu_{47.5}Zr_{47.5}Al_5$ (●), $Cu_{47.5}Zr_{38}Hf_{9.5}Al_5$ (▲) and $Cu_{47}Zr_{47}Al_6$ (▼)……69
Figure 4.1: Longitudinal modulus L as a function of temperature for $Ca_{50}Mg_{20}Cu_{30}$ (■), $Ca_{55}Mg_{18}Zn_{11}Cu_{16}$ (●) and $Ca_{65}Mg_{15}Zn_{20}$ (▲)……71
Figure 4.2: Shear modulus G as a function of temperature for $Ca_{50}Mg_{20}Cu_{30}$ (■), $Ca_{55}Mg_{18}Zn_{11}Cu_{16}$ (●) and $Ca_{65}Mg_{15}Zn_{20}$ (▲)……72
Figure 4.3: Bulk modulus B as a function of temperature for $Ca_{50}Mg_{20}Cu_{30}$ (■), $Ca_{55}Mg_{18}Zn_{11}Cu_{16}$ (●) and $Ca_{65}Mg_{15}Zn_{20}$ (▲)……72
Figure 4.4: Young's modulus E as a function of temperature for $Ca_{50}Mg_{20}Cu_{30}$ (■), $Ca_{55}Mg_{18}Zn_{11}Cu_{16}$ (●) and $Ca_{65}Mg_{15}Zn_{20}$ (▲)……73
Figure 4.5: Poisson ratio ν as a function of temperature for $Ca_{50}Mg_{20}Cu_{30}$ (■), $Ca_{55}Mg_{18}Zn_{11}Cu_{16}$ (●) and $Ca_{65}Mg_{15}Zn_{20}$ (▲)……73
Figure 4.6: Internal friction Q^{-1} as a function of temperature for $Ca_{50}Mg_{20}Cu_{30}$ (■), $Ca_{55}Mg_{18}Zn_{11}Cu_{16}$ (●) and $Ca_{65}Mg_{15}Zn_{20}$ (▲)……76
Figure 4.7: Heat capacity as a function of temperature for $Ca_{50}Mg_{20}Cu_{30}$ (■), $Ca_{55}Mg_{18}Zn_{11}Cu_{16}$ (●) and $Ca_{65}Mg_{15}Zn_{20}$ (▲). (a) 3-300 K. (b) 295-398 K……77
Figure 4.8: Dependence of bulk modulus B, shear modulus G, Young's modulus E and longitudinal modulus L on glass transition temperature T_g for Zr-based, Cu-based and Ca-based BMGs……79
Figure 4.9: Dependence of bulk modulus B, shear modulus G, Young's modulus E and longitudinal modulus L on crystallization temperature T_x for Zr-based, Cu-based and Ca-based BMGs……79
Figure 5.1: Temperature dependence of shear modulus for Zr-based BMGs, $Zr_{50}Cu_{30}Ni_{10}Al_{10}$ (□), $Zr_{50}Cu_{40}Al_{10}$ (■), $Zr_{52.5}Cu_{17.9}Ni_{14.6}Al_{10}Ti_5$ (○), $Zr_{50}Cu_{35}Al_{10}Pd_5$ (▲), $Zr_{50}Cu_{33}Al_{10}Pd_7$ (◊) and $Zr_{50}Cu_{31}Al_{10}Pd_9$ (▽), Cu-based BMGs, $Cu_{47.5}Zr_{47.5}Al_5$ (Δ) and $Cu_{47.5}Zr_{38}Hf_{9.5}Al_5$ (▼) and Ca-based BMGs, $Ca_{55}Mg_{18}Zn_{11}Cu_{16}$ (◀) and $Ca_{65}Mg_{15}Zn_{20}$ (▶). The solid line is the model calculation……81

Figure 5.2: Temperature dependence of bulk modulus for Zr-based BMGs, $Zr_{50}Cu_{30}Ni_{10}Al_{10}$ (□), $Zr_{50}Cu_{40}Al_{10}$ (■), $Zr_{52.5}Cu_{17.9}Ni_{14.6}Al_{10}Ti_5$ (○), $Zr_{50}Cu_{35}Al_{10}Pd_5$ (▲), $Zr_{50}Cu_{33}Al_{10}Pd_7$ (◊) and $Zr_{50}Cu_{31}Al_{10}Pd_9$ (▽), Cu-based BMGs, $Cu_{47.5}Zr_{47.5}Al_5$ (Δ) and $Cu_{47.5}Zr_{38}Hf_{9.5}Al_5$ (▼) and Ca-based BMGs, $Ca_{55}Mg_{18}Zn_{11}Cu_{16}$ (◄) and $Ca_{65}Mg_{15}Zn_{20}$ (►). The solid line is the model calculation……84

Figure 5.3: Temperature dependence of longitudinal modulus for Zr-based BMGs, $Zr_{50}Cu_{30}Ni_{10}Al_{10}$ (□), $Zr_{50}Cu_{40}Al_{10}$ (■), $Zr_{52.5}Cu_{17.9}Ni_{14.6}Al_{10}Ti_5$ (○), $Zr_{50}Cu_{35}Al_{10}Pd_5$ (▲), $Zr_{50}Cu_{33}Al_{10}Pd_7$ (◊) and $Zr_{50}Cu_{31}Al_{10}Pd_9$ (▽), Cu-based BMGs, $Cu_{47.5}Zr_{47.5}Al_5$ (Δ) and $Cu_{47.5}Zr_{38}Hf_{9.5}Al_5$ (▼) and Ca-based BMGs, $Ca_{55}Mg_{18}Zn_{11}Cu_{16}$ (◄) and $Ca_{65}Mg_{15}Zn_{20}$ (►). The solid line is the model calculation……84

Figure 5.4: Temperature dependence of Young's modulus for Zr-based BMGs, $Zr_{50}Cu_{30}Ni_{10}Al_{10}$ (□), $Zr_{50}Cu_{40}Al_{10}$ (■), $Zr_{52.5}Cu_{17.9}Ni_{14.6}Al_{10}Ti_5$ (○), $Zr_{50}Cu_{35}Al_{10}Pd_5$ (▲), $Zr_{50}Cu_{33}Al_{10}Pd_7$ (◊) and $Zr_{50}Cu_{31}Al_{10}Pd_9$ (▽), Cu-based BMGs, $Cu_{47.5}Zr_{47.5}Al_5$ (Δ) and $Cu_{47.5}Zr_{38}Hf_{9.5}Al_5$ (▼) and Ca-based BMGs, $Ca_{55}Mg_{18}Zn_{11}Cu_{16}$ (◄) and $Ca_{65}Mg_{15}Zn_{20}$ (►). The solid line is the model calculation……85

Figure 5.5: Temperature dependence of Poisson ratio for Zr-based BMGs, $Zr_{50}Cu_{30}Ni_{10}Al_{10}$ (□), $Zr_{50}Cu_{40}Al_{10}$ (■), $Zr_{52.5}Cu_{17.9}Ni_{14.6}Al_{10}Ti_5$ (○), $Zr_{50}Cu_{35}Al_{10}Pd_5$ (▲), $Zr_{50}Cu_{33}Al_{10}Pd_7$ (◊) and $Zr_{50}Cu_{31}Al_{10}Pd_9$ (▽), Cu-based BMGs, $Cu_{47.5}Zr_{47.5}Al_5$ (Δ) and $Cu_{47.5}Zr_{38}Hf_{9.5}Al_5$ (▼) and Ca-based BMGs, $Ca_{55}Mg_{18}Zn_{11}Cu_{16}$ (◄) and $Ca_{65}Mg_{15}Zn_{20}$ (►). The solid line is the model calculation……85

Figure 6.1: Correlation of elastic moduli with fracture strength……87

Figure 6.2: Correlation of elastic moduli with fatigue limit……87

Figure 6.3: Correlation of elastic moduli with Vickers hardness……88

Figure 6.4: The dependence of fatigue limit and fracture strength on the Poisson ratio...88

Figure 6.5: The dependence of the ratio of fatigue limit to fracture strength on the Poisson ratio……89

LIST OF ABBREVIATIONS

BMG	bulk metallic glass
DSC	differential scanning calorimetry
DTA	differential thermal analysis
FWHM	full width at half maximum
GFA	glass forming ability
HREM	high resolution electron microscopy
RP	rectangular parallelepipeds
RE	rare earth
RUS	resonant ultrasound spectroscopy
SEM	scanning electron microscopy
TEM	transmission electron microscopy
XRD	X-ray diffraction

LIST OF SYMBOLS

a_0	nearest neighbor distance
B	bulk modulus
B_{el}	free electron contribution to bulk modulus
B_{lat}	lattice contribution to bulk modulus
C	elastic constant of BMGs
C_i	elastic constant of constituent element of BMGs
C_0	elastic constant at ambient pressure and ambient temperature
c_{ijkl}	elastic constant tensor
c_{ij}^0	elastic constant at 0 K
C_P	specific heat at constant pressure
D	fragility parameter
d_c	critical casting diameter
E	Young's modulus
E_a	high temperature activation energy
E_{el}	energy of free electron
f	resonant frequency
F	force
F_1	GFA parameter
G	shear modulus
G_0	static shear modulus
G_r	fracture energy
h	Planck constant
H_v	Vickers hardness
K	stress intensity
K_{Ic}	fracture toughness
k_B	Boltzmann constant
K_{gl}	Hruby factor
L	longitudinal modulus
m	fragility index

M	molecular mass
M_a	average atomic mass
N_A	Avogadro's number
P	pressure
P_0	ambient pressure
q	number of atoms in the chemical formula
Q	quality factor
R	gas constant
R_c	critical cooling rate
s	fitting parameter in Varshni Equation
t	fitting parameter in Varshni Equation
T	temperature
T_g	glass transition temperature
T_l	liquidus temperature
T_x	onset crystallization temperature
T_{rg}	reduced glass transition temperature
u	oscillation displacement
U	potential energy
V	volume
V_A	atomic volume
v_l	longitudinal acoustic velocity
V_m	molar volume
v_t	transverse acoustic velocity
x_{ai}	atomic fraction of the constituent element of BMGs
α	linear expansion coefficient
ν	Poisson ratio
ρ	physical density
θ_D	Debye temperature
ΔT_{xg}	supercooled liquid region
γ	GFA parameter

γ_c	critical shear strain
γ_G	Grüneisen constant
γ_m	modified GFA parameter
$\dot{\gamma}$	strain rate
η	viscosity
τ	shear stress
τ_Y	shear stress at yielding
σ	fracture strength
$\dot{\varepsilon}$	strain rate
ε_v^{crit}	critical volume strain
$\varepsilon_v^{T,crit}$	critical transformation volume strain
λ	wavelength
ω	angular frequency

INTRODUCTION

Bulk metallic glasses (BMGs), displaying a unique combination of mechanical and physical properties, have emerged over the past few years as a new class of metallic materials. The structural use of BMGs, however, encounters a technical difficulty in that most BMGs exhibit low ductility during plastic deformation under tension. In order to solve this material problem, considerable effort has been devoted to the alloy development of "ductile" BMGs. Whereas the brittleness of crystalline metals is known to be correlated to the ratio of the elastic shear modulus to the bulk modulus, *G/B* (Pugh, 1954), a similar assessment for metallic glasses was not available until recently, when a universal correlation between the energy of fracture and the Poisson ratio for bulk metallic glasses was reported, with ductile glasses displaying a high Poisson ratio (Lewandowski, 2005). This confirms earlier results from Schroers *et al.* who concluded that a large Poisson ratio and a low glass transition temperature might be used as a means of identifying ductile BMGs (Schroers, 2004). The importance of the Poisson ratio in the study of glasses was also pointed out by Novikov and Sokolov (Novikov, 2004), who showed that the ratio of instantaneous shear to bulk modulus *G/B* in glasses, or, alternatively, the Poisson ratio ν, is linked to the fragility of the glass-forming liquid, an important parameter used to evaluate the glass forming ability (GFA) of glasses. Even though this finding is still controversial (Wang, 2006) (Battezzati, 2005) (Yannopoulos, 2006) (Johari, 2006), it suggests that a systematic study of the elastic properties and thus the Poisson ratio of metallic glasses is expected to yield important information about their mechanical properties.

Zr-based BMGs have superior glass forming ability (GFA) and high strength, but their ductility needs to be improved. Ca-based BMGs have low glass transition temperatures ($T_g \approx 390$ K), which make them very attractive to be studied near T_g. Cu-based BMGs recently have received wide interest because of their low cost and good mechanical properties. In this work, we have applied Resonant Ultrasound Spectroscopy (RUS) to study the elastic properties of these BMGs. Elastic properties provide valuable

information about mechanical properties, physical properties and thermodynamic properties.

In Chapter 1, we will give a brief summary of the literature. The development of BMGs, the parameters used to evaluate glass forming ability of BMGs, and recent studies of elastic properties of BMGs will be reviewed. Chapter 2 describes the experimental details on the RUS technique, sample preparation and data analysis. In Chapter 3, the elastic properties of Zr-based and Cu-based BMGs are reported. The temperature dependence of elastic constants and internal friction was studied up to their glass transition temperature (T_g ≈710 K). By increasing Pd content in $Zr_{50}Cu_{40-x}Al_{10}Pd_x$, BMGs with high Poisson ratio and thus better ductility were obtained. The effects of casting diameter on the elastic moduli have also been investigated. The newly developed two-phase $Zr_{63.8}Ni_{16.2}Cu_{15}Al_5$ alloy was found to have a very high Poisson ratio ~0.39. In Chapter 4, the temperature dependence of elastic constants, internal friction, and heat capacity of Ca-based BMGs were investigated up to their glass transition temperature (T_g ≈390 K). In Chapter 5, a simple model is proposed to predict the temperature dependence of the elastic moduli for BMGs based on room temperature measurements. The validity of the model is tested using our own database of experimental data obtained on a large variety of BMGs. In Chapter 6, correlation with other work and perspective for future work is discussed.

CHAPTER 1

LITERATURE REVIEW

Bulk metallic glasses (BMGs) have very high yield strength, high hardness, good corrosion resistance and wear resistance, low melting temperature T_m and net-shape casting capability. They are used as industrial coatings, electronic casings, fine jewelry, medical devices, sporting goods, as well as hinge applications (http://www.liquidmetal.com). However, their applications as structural materials encounter difficulty because of the low ductility, high cost and small critical casting diameter.

1.1 Development of BMGs

The formation of the first metallic glass, $Au_{75}Si_{25}$ was reported by Klement, Willens and Duwez at Caltech in 1960, using the rapid quenching technique at ultra-high cooling rate (10^5-10^6 K/s) to prevent the formation of crystalline structures (Klement, 1960). The technique allows the preparation of large quantities of glassy alloys. However, the ultra-high cooling rate limits the geometry of the glassy alloys to samples with thin cross-section (ribbons, wires, droplets etc.). The first bulk metallic glass, ternary Pd-Cu-Si alloy, was prepared by Chen in 1974 (Chen, 1974). Cylinders with diameter 1-3 mm were prepared using suction-casting methods with the cooling rate less than 10^3 K/s. In 1982, Lee et al. prepared spheres of metallic glass $Au_{55}Pb_{22.5}Sb_{22.5}$ with diameter up to 1.5 mm (Lee, 1982). Drehman et al. produced spheroids of $Pd_{40}Ni_{40}P_{20}$ glass with diameters of 5-9 mm at the cooling rate of 1 K/s, under the condition that the alloy was kept very clean to inhibit heterogeneous nucleation (Drehman, 1982) (Drehman, 1984). Kui et al. obtained Pd-Ni-P glass ingot of centimeter size at a cooling rate of 10 K/s, using a boron oxide (Kui, 1984). Even though these achievements are exciting, the high cost of Au and Pd metals has limited the interest for these alloys to academic research.

Inoue's group in Tohoko University of Japan succeeded in finding new multicomponent alloys without the expensive noble metals. Amorphous $La_{55}Al_{25}Ni_{20}$ ribbon (Inoue, 1989)

and $Zr_{60}Al_{20}Ni_{20}$ ribbon (Inoue, 1990a) were formed by melt-spinning. The high thermal stability of the supercooled liquid was believed to result from optimum bonding and packing states of the constituent atoms. In 1990, amorphous $La_{55}Al_{25}Ni_{20}$ rods and bars with critical casting diameter of 2-3 mm were prepared by low pressure casting the alloy melt into a water-cooled copper mold (Inoue, 1990 b). In 1992, amorphous $Mg_{65}Cu_{25}Y_{10}$ cylinder with diameter of 7 mm was prepared using a high-pressure die casting process (Inoue, 1992). In 1993, bulk amorphous $Zr_{65}Cu_{17.5}Ni_{10}Al_{7.5}$ rods with diameter up to 16 mm were formed by water quenching the alloy melt in a quartz tube (Inoue, 1993a). It indicated the possibility of forming BMGs by conventional casting processes.

Johnson's group in Caltech recognized the significance of research in BMGs and started to search for new compositions. In 1993, Peker and Johnson developed a highly processable metallic glass $Zr_{41.2}Ti_{13.8}Cu_{12.5}Ni_{10.0}Be_{22.5}$, in the form of rods up to 14 mm in diameter by casting in silica containers with critical cooling rate in the order of 10 K/s or less (Peker, 1993). Inoue's group continued the significant work devoted to BMGs. In 1996, Inoue's group formed bulk glassy $Pd_{40}Cu_{30}P_{20}Ni_{10}$ alloys of 40 mm in diameter by water quenching (Inoue, 1996). Using a B_2O_3 flux treatment to suppress the heterogeneous nucleation, amorphous $Pd_{40}Cu_{30}P_{20}Ni_{10}$ alloys with maximum thickness up to 75 mm were prepared with a low critical cooling rate of 0.1 K/s (Inoue, 1997a) (Inoue, 1997b). Co-based and Fe-based BMGs, $Co_{56}B_{20}Fe_{16}B_8$, $Fe_{56}B_{20}Zr_{10}Co_7Ni_7$, $Fe_{56}B_{20}Zr_8Co_7Ni_7Nb_2$ and $Fe_{60}B_{15}Zr_{10}Co_8Mo_5W_2$ with maximum casting diameter of 1 mm to 6 mm were prepared by arc melting a mixture of the components in an argon atmosphere followed by injection casting of the molten alloy into copper mold. These BMGs exhibited good soft magnetic properties characterized by low coercive force and high permeability (Inoue, 1998). Cu-based BMGs $Cu_{60}Zr_{30}Ti_{10}$ and $Cu_{60}Hf_{25}Ti_{15}$ with diameter 4 mm were formed by copper mold casting method and they showed high fracture strength, above 2 GPa (Inoue, 2001a).

Many researchers are devoted to the study of BMGs, as is reflected by the annual symposia on BMGs organized by The Materials Research Society and The Mineral,

Metals and Materials Society as well as the biannual BMG conference. Figure 1.1 shows how the critical casting thickness of BMGs has increased three-orders of magnitude over the past forty years (Loffler, 2003). The potential applications of BMGs are summarized in Table 1.1 (Inoue, 2000) (Wang 2004c).

1.2 Glass Forming Ability

The Glass Forming Ability (GFA) reflects how easy a liquid vitrifies on cooling. It is often considered as a dynamic competition between cooling rate and crystallization kinetics. It is related to the glass's resistance against devitrification on heating (Nascimento, 2005). Above the critical cooling rate R_c, no crystallization occurs during solidification. BMGs with high GFA can be vitrified with low critical cooling rate R_c and into geometries with large critical casting diameter d_c. However, R_c is not easily measured.

It is a time-consuming process since solidification trials with various cooling rates are needed. Various criteria have been proposed to evaluate the GFA of alloys based on the

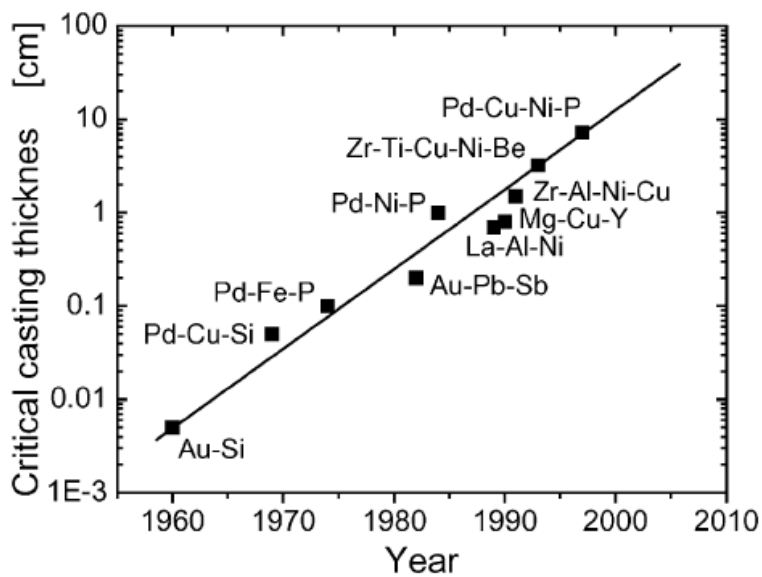

Figure 1.1: Evolution of the critical casting thickness for bulk metallic glasses over the past forty years (Loffler, 2003).

Table 1.1: Application fields for BMGs (Inoue, 2000) (Wang, 2004 c).

Properties	Application field
High strength	Machinery structural materials
High hardness	Cutting materials
High fracture toughness	Die materials
High impact fracture energy	Tool materials
High fatigue strength	Bonding materials
High elastic energy	Sporting goods materials
High corrosion resistance	Corrosion resistance materials
High wear resistance	Writing application materials
High reflection ratio	Optical precision materials
High viscous flowability	Ornamental materials
High wear resistance and manufacturability	Medical devices materials

characteristic temperatures, easily obtained by differential thermal calorimetry and/or differential thermal analysis.

In 1969, the first criterion was proposed by Turnbull, using the reduced glass transition temperature T_{rg},

$$T_{rg}=T_g/T_l \tag{1.1}$$

with T_g the glass transition temperature and T_l the liquidus temperature (Turnbull, 1969). Turnbull predicted that a liquid with $T_{rg}\geq 2/3$ becomes very sluggish on laboratory time scale and can only crystallize within a very narrow temperature range, and thus can be readily undercooled into the glassy state with a low cooling rate. Larger T_{rg} indicates better GFA because of smaller temperature range from melt to glassy solid state during the solidification, leading to easier freezing of the glassy state. Turnbull's criterion has played a crucial role in the early development of BMGs (Inoue, 1989) (Inoue, 1990a). Nowadays it is still widely used to find BMGs of new compositions and good glass formers (Waniuk, 2001) (Inoue, 2001a). Lu et al. reported that T_g/T_l showed better

correlation with GFA than T_g/T_m (with T_m the melting temperature) after examining various BMGs, including Mg-Ni-Nd, Zr-Al-Cu-Ni, Ti-Zr-Cu-Ni, La-Al-Ni-Cu, Pd-Cu-Si, Pd-Cu-Ni-P, Nd (Pr, Sm, Y)-Fe-Al etc. (Lu, 2002).

Since the late 1980s, the supercooled liquid region ΔT_x has been used to evaluate the GFA of BMGs:

$$\Delta T_x = T_x - T_g \tag{1.2}$$

with T_x the onset crystallization temperature (Inoue, 1989) (Inoue, 1990a) (Zhang, 1991) (Inoue, 1996) (Inoue, 1997a) (Inoue, 1999). Large ΔT_x indicates good GFA, since it implicates that the supercooled liquid can exist in a wide temperature range without crystallization and the resistance to the transition from solid glassy state to crystalline state during the heating is high. Inoue et al. investigated a number of Fe-, Pd-, Pt-, La-, Zr- and Mg-based BMGs and proved the correlation among the critical cooling rate R_c, maximum sample thickness t_{max} and supercooled liquid region ΔT_x as shown in Figure 1.2 (Inoue, 1999). Not shown in the figure is the additional correlation that was found between R_c, t_{max} and the reduced glass transition temperature T_{rg}.

Although both T_{rg} and ΔT_x have been widely used to evaluate GFA of BMGs, they show different trends versus GFA in some alloy system. For instance, Waniuk et al. reported that for Zr-Ti-Cu-Ni-Be BMGs only T_{rg} correlated well with GFA (Waniuk, 2001). Inoue et al. showed that for Cu-Zr-Ti and Cu-Hf-Ti alloys GFA correlated better with T_{rg} than with ΔT_x (Inoue, 2001a) (Inoue, 2001b). On the other hand, it was reported that for $Pd_{40}Ni_{40-x}Fe_xP_{20}$ (Shen, 1999a), Fe-(Co, Cr, Mo, Ga, Sb)-P-B-C (Shen, 1999b), and $Mg_{65}Cu_{15}M_{10}Y_{10}$ (M=Ni, Al, Zn, Mn) (Murty, 2000), ΔT_x, rather than T_{rg}, provided good gauge for the optimization of GFA.

In 1972, the Hruby factor K_{gl} was proposed to evaluate GFA of non-polymer glasses, such as As-Te-Si, As-Te-Tl, As-Te-Ge, Cd-Ge-As-P (Hruby, 1972). Defined as

$$K_{gl} = (T_x - T_g)/(T_l - T_x) \tag{1.3}$$

with T_x, T_g and T_l as defined above, this factor is also used to evaluate GFA of BMGs and

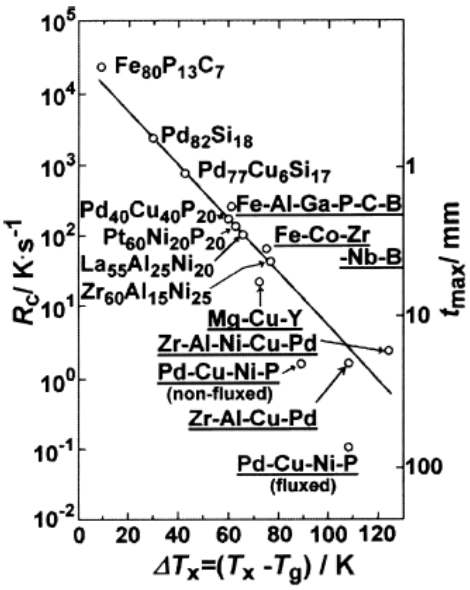

Figure1.2: Relation among the critical cooling rate R_c, maximum sample thickness t_{max} and supercooled liquid region ΔT_x for typical bulk glassy alloys (Inoue, 1999).

it was reported that K_{gl} is more suitable than ΔT_x and T_{rg} in the evaluation of GFA of Zr-Cu-Al alloys (Yokoyama, 2004).

The "confusion principle" indicates that when more elements are involved, there is smaller chance that the alloy can select viable crystal structures, leading to a greater chance of glass forming (Greer, 1993). It is believed that large glass forming ability results from a combined effect of the difficulty of long-range atomic redistribution required for the precipitation of the compounds, the rapid increase of viscosity with decreasing temperature and the large liquidus-solidus interfacial energy stemming from the optimally bonding and packing states due to large negative heat of mixing and large atomic size ratios (Inoue, 1993b). The empirical criteria are summarized as follows:

(1) multicomponent alloy of three or more elements with a composition close to the deep eutectic;

(2) atomic radius mismatch between the components is greater than 12%;

(3) large negative heat of mixing between the main components (Inoue, 1995) (Inoue, 1998).

Lin et al. proposed that the critical cooling rate R_c can be estimated from the critical casting diameter d_c,

$$R_c = \frac{10}{d_c^2} \tag{1.4}$$

with R_c in the unit of K/s and d_c in the unit of cm (Lin, 1995).

In supercooled liquids, the movement of atoms slows down upon supercooling, which is illustrated by the increase in the viscosity η of the liquid. The Vogel-Fulcher-Tammann equation,

$$\eta = \eta_0 \exp\left(\frac{A}{T - T_0}\right) \tag{1.5}$$

with η_0 the high temperature limit of viscosity and T_0 the VFT temperature at which the barrier to flow goes to infinity, was proposed to describe the temperature dependence of the viscosity η (Vogel, 1921) (Fulcher, 1925) (Tammann, 1925). The concept of the fragility of a glass forming liquid was proposed by Angell, who modified the Vogel-Fulcher-Tammann equation into

$$\eta = \eta_0 \exp\left(\frac{DT_0}{T - T_0}\right) \tag{1.6}$$

with D the fragility parameter (Angell, 1985) (Angell, 1995). A large D value indicates a strong liquid and thus a good glass former, showing an Ahrrenius temperature dependence of the viscosity in the supercooled melt,

$$\eta = \eta_0 \exp(E_a / T) \tag{1.7}$$

with E_a the high temperature activation energy. Small D values indicate a fragile liquid, and thus a bad glass former, showing non-Ahrrenius temperature dependence of viscosity. The viscosity is typically normalized to the glass transition temperature T_g, where the viscosity is 10^{13} poise, i.e. 10^{12} Pa·s, as shown in Figure 1.3.

The fragility index m is defined as

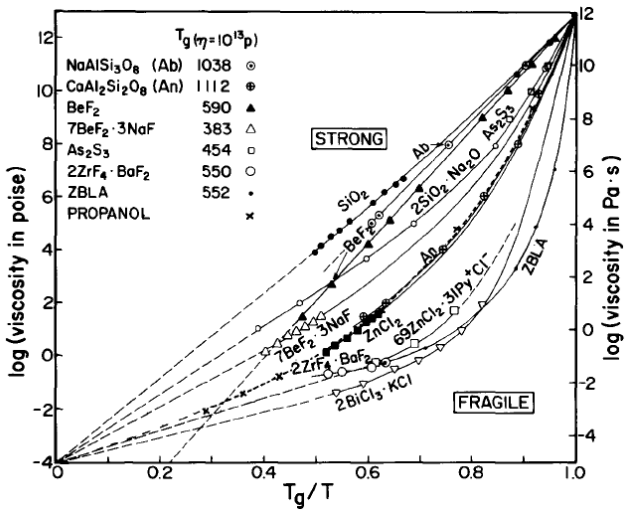

Figure 1.3: Scaled viscosity data for glass-forming liquids showing range of behavior from "strong" characteristic of open tetrahedral network liquids, to "fragile" typical of ionic and molecular liquids. ZBLA is $(ZrF_4)_{0.53}(BaF_2)_{0.20}(LaF_3)_{0.04}(AlF_3)_{0.03}(NaF)_{0.20}$ (Angell, 1985).

$$m = \left.\frac{\partial \log \eta(T)}{\partial (T_g / T)}\right|_{T=T_g} \tag{1.8}$$

(Angell, 1985) (Novikov, 2004). Large *m* values indicate a fragile liquid, and thus a bad glass former. The Angell plot of the viscosities of Mg-based, Zr-based BMGs and several nonmetallic glasses is shown in Figure 1.4 (Busch, 1998). It indicates that BMGs are moderately strong liquids. *D* usually ranges from 3 (for fragile liquids, such as pure metals) to 40 (for strong liquids, such as silica). For BMGs, *D* is typically 15-25 (Busch, 2001). Tanaka studied a number of Mg-, Zr-, Cu-, Pd-, La-based BMGs and proved the correlation between GFA (indicated by the critical cooling rate R_c) and fragility parameter *D*, as shown in Figure 1.5 (Tanaka, 2005).

In general, the lower the Gibbs free energy difference ΔG between the liquid and the crystalline states, the better the glass forming ability of the alloy. Glade et al. calculatedΔG for some Zr-based, Cu-based and Mg-based metallic glasses and gave a qualitative evaluation of the GFA, as shown in Figure 1.6 (Glade, 2000).

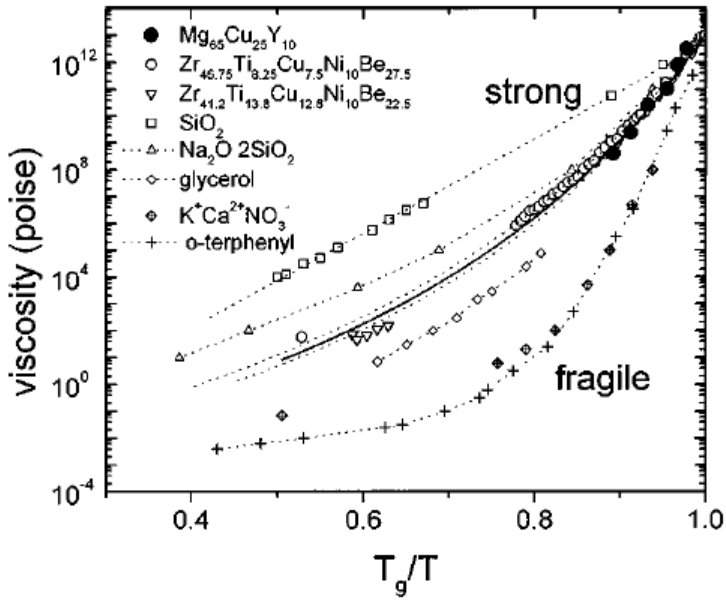

Figure 1.4: Angell plot of the viscosities of Mg-based, Zr-based BMGs and several nonmetallic glasses (Busch, 1998).

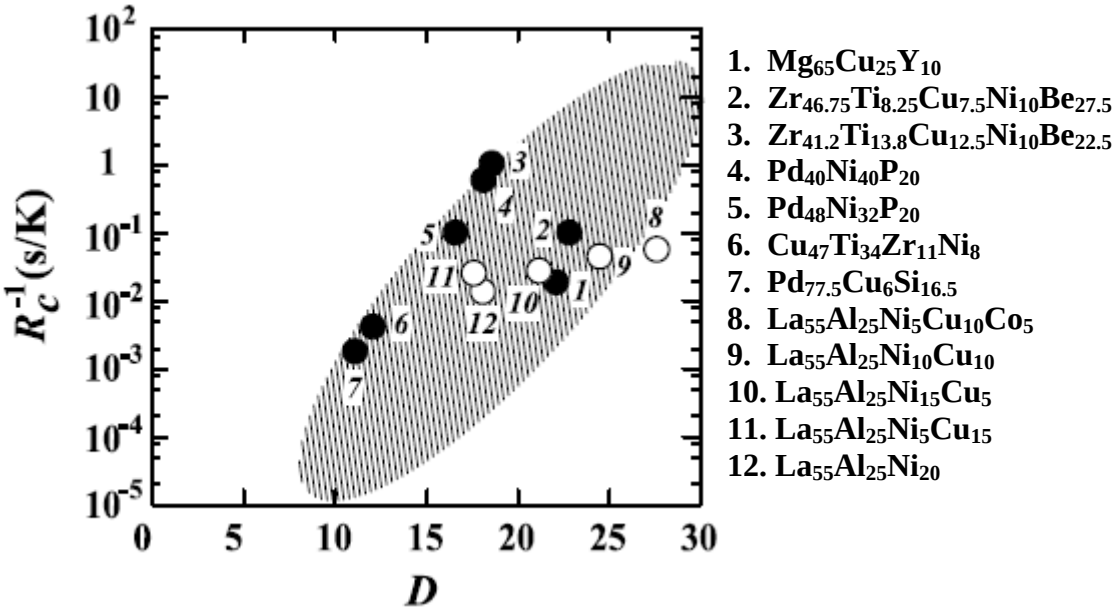

Figure 1.5: Correlation of the inverse of the critical cooling rate R_c^{-1} with the fragility parameter D (Tanaka, 2005).

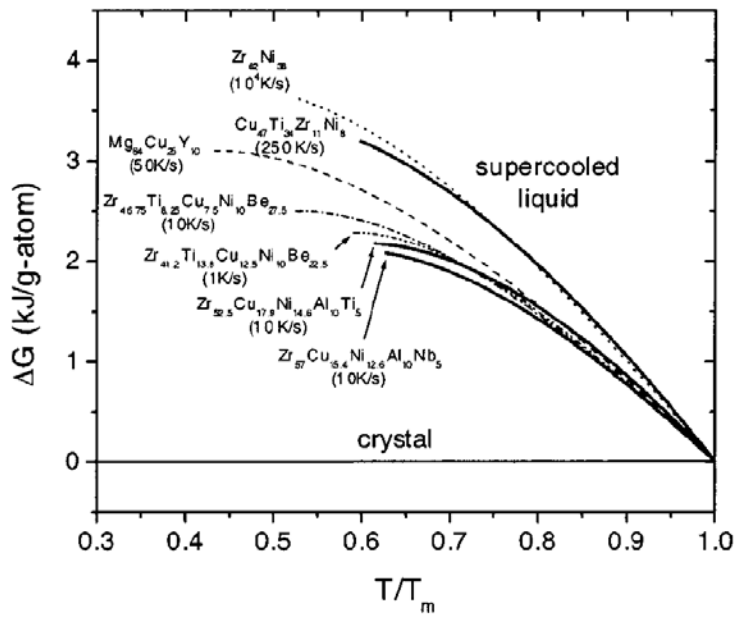

Figure 1.6: The calculated difference in the Gibbs free energy between the liquid and the crystalline states for a number of glass forming alloys (Glade, 2000).

Lu and Liu proposed a parameter γ to indicate the GFA of BMGs based on crystallization processes during cooling and reheating of the supercooled liquid (Lu, 2002) (Lu, 2003).

$$\gamma = T_x/(T_g+T_l) \tag{1.9}$$

The maximum value of γ is 0.5. Larger γ indicates better GFA. After examining 49 metallic glasses, including Mg-based, Zr-based, La-based, Pd-based, Nd-based, Cu-based and Ti-based metallic glasses, an exponential relationship was found between R_c and γ,

$$\log_{10} R_c = 21.71 - 50.9\gamma \tag{1.10}$$

as shown in Figure 1.7. The statistical correlation factor R^2 of the fit is as high as 0.91, implying a strong correlation between R_c and γ. The critical casting diameter d_c as a function of γ for typical BMGs shows also an exponential relationship,

$$\log_{10} d_c = -6.55 + 18.11\gamma \tag{1.11}$$

but with a lot of scattering (R^2=0.57).

Du et al. proposed a modified γ parameter (Du, 2007a), defined as

$$\gamma_m = (2T_x - T_g)/T_l \tag{1.12}$$

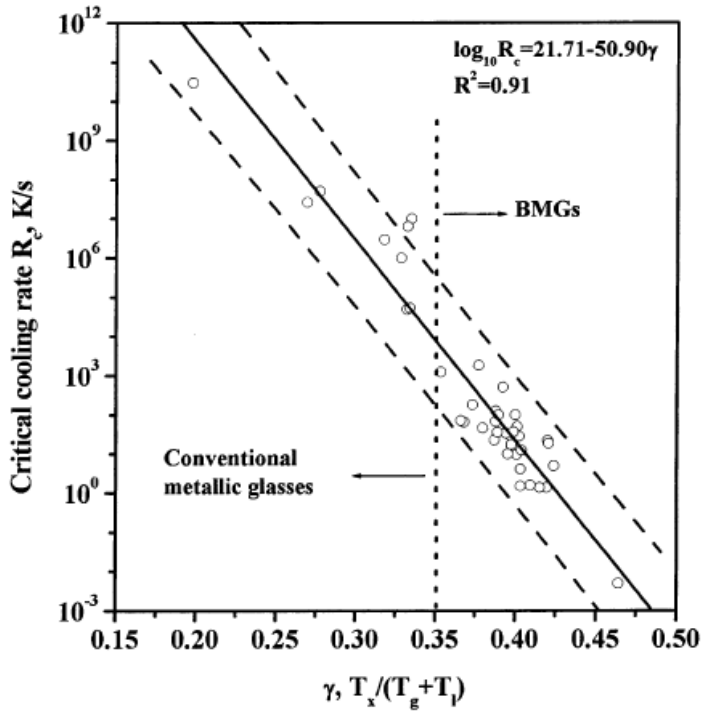

Figure 1.7: Correlation between parameter γ and critical cooling rate R_c for representative metallic glasses (Lu, 2002).

with increasing γ_m, R_c is lower, indicating better GFA.

Gorsse et al. performed thermodynamic analysis of GFA in Ca-Mg-Zn BMGs and proposed that the combination of low onset driving forces, high solid/liquid interfacial energy and strong liquid behavior lead to better GFA (Gorsse, 2006). Senkov proposed the parameter F_1,

$$F_1 = \frac{2}{\frac{m}{m_{\min}}\left(\frac{1}{T_{rg}} - 1\right) + 2} \tag{1.13}$$

where m is the fragility index and T_{rg} is the reduced glass transition temperature, to evaluate GFA of glasses (Senkov, 2007). Small m values indicate a strong glass forming liquid and thus a good glass former. The extremely strong liquid shows Arrhenius behavior and has the minimum m value, $m_{min}\approx 16$. The extremely fragile liquid has m value close to infinity. F_1 is close to zero for an extremely fragile liquid, and it is equal to

$2T_{rg} / (1+T_{rg})$ for an extremely strong liquid. With increasing T_{rg} and decreasing m, F_1 increases and the critical cooling rate R_c decreases, as shown in Figure 1.8. An exponential relationship between F_1 and R_c,

$$F_1 = 0.54 - 0.047 \log_{10} R_c \tag{1.14}$$

was identified and verified by available experimental data for metallic Mg-, Pd-, Cu-, Zr-, La-based glasses and nonmetallic glasses, as shown in Figure 1.9. F_1, a function of T_{rg} and m, has better correlation with R_c than T_{rg} and m individually.

The various approaches to estimate the glass forming ability are further complicated by the fact that the characteristic temperatures, e.g. T_g, T_x and T_l, depend on the heating rate (Debenedetti, 2001). For instance, when the cooling rate changes by one order of magnitude, the change in T_g is 3-5 K. When GFA is evaluated using the above parameters, the heating rate needs to be considered. Lu et al. examined some BMGs and reported that when the heating rate is changed from 10 K/min to 40 K/min, the change in γ value is less than 5% (Lu, 2003). With the development of new BMGs and other glasses, research efforts are devoted to the search of a better GFA parameter.

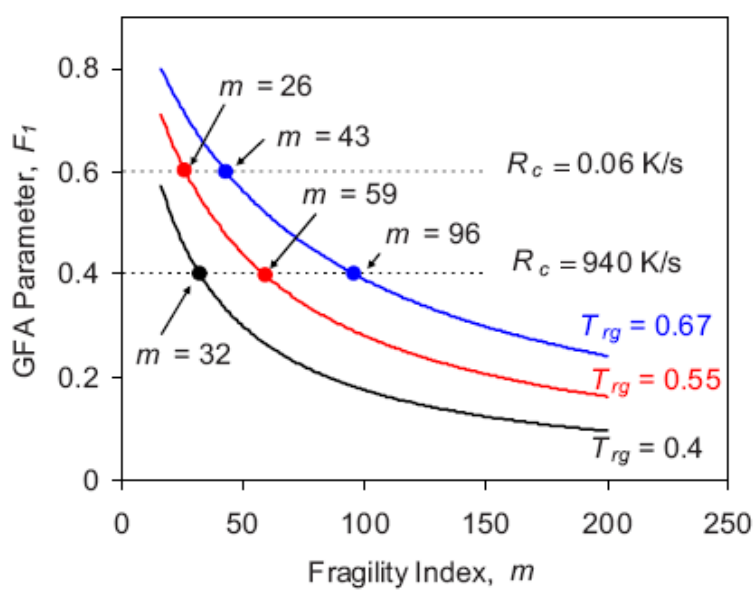

Figure 1.8: Dependence of the glass forming ability parameter F_1 on the fragility index m at three different T_{rg} values (Senkov, 2007).

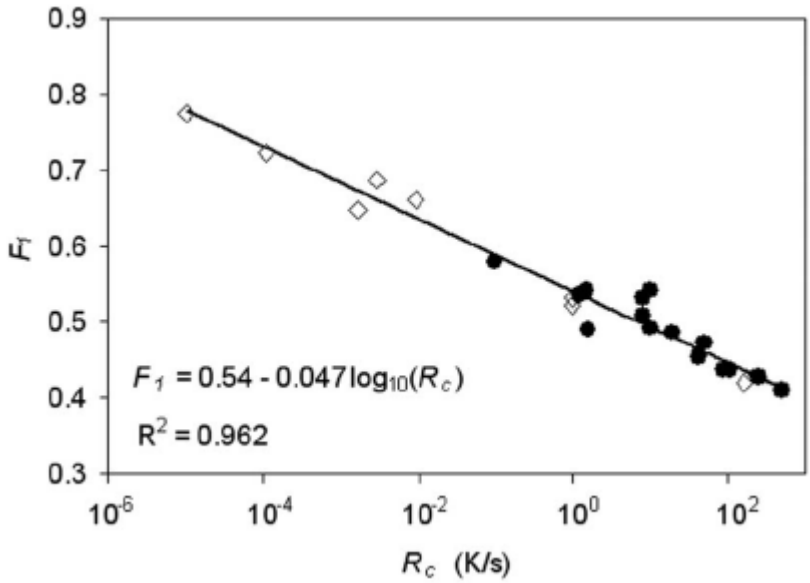

Figure 1.9: Correlation between the critical cooling rate R_c and the glass forming ability parameter F_1 for several glass forming systems. Solid circles correspond to the bulk metallic glasses and open diamonds correspond to the nonmetallic glasses (Senkov, 2007).

1.3 Elastic Properties of BMGs

The elastic properties of a solid describe how the material responds to stress and are of considerable interest to both science and technology. Not only do they contain fundamental information about the nature of the interatomic bonding in the material, they determine the mechanical behavior of solids, and are therefore essential parameters to determine potential failure of an object in a given application. In the past few years, significant research efforts have been devoted to the study of the elastic properties of bulk metallic glasses (BMGs) (Wang, 2006) (Tarumi, 2007) (Duan, 2008). Knuyt et al. calculated the difference between the moduli of the amorphous and crystalline phases using a Gaussian distribution for the nearest-neighbor distance and a two-particle inter-atomic potential (Knuyt, 1991). It was demonstrated that the anharmonic part of the inter-atomic potential and local relative atomic displacements lead to the lower moduli in the amorphous phase. According to the computer simulation, the bulk modulus is 4% lower and the shear modulus is 30% lower in the amorphous solid compared to its crystalline counterpart, in agreement with a number of experimental data (Golding, 1972) (Chen,

1978) (Knuyt, 1986). Section 1.3.1 will focus on the effects of temperature, pressure and composition on the elastic properties. Section 1.3.2 will concentrate on the relationship between elastic constants and mechanical properties. Section 1.3.3 will focus on the correlation of elastic constants with the glass transition temperature T_g and with the glass forming ability (GFA). Section 1.3.4 will concentrate on the physics of elastic properties.

1.3.1 Effects of temperature, pressure and composition on elastic properties

Wang et al. measured the elastic moduli of $Pd_{39}Ni_{10}Cu_{30}P_{21}$ BMG (with T_g=564 K and T_x=637 K) as a function of annealing temperature as shown in Figure 1.10 (Wang, 2000). With increasing annealing temperature, both the density and the elastic moduli increase due to the progressive ordering while the sample stepwise undergoes structural relaxation and crystallization. After crystallization, Young's modulus E increases 25.1%, the shear modulus G increases 27.3% and the Debye temperature θ_D increases 12.3%. On the other hand, the bulk modulus B increases only 1.25% and the density ρ increases 0.62%. The large increase in G and θ_D is mainly attributed to the strong interactions among atoms,

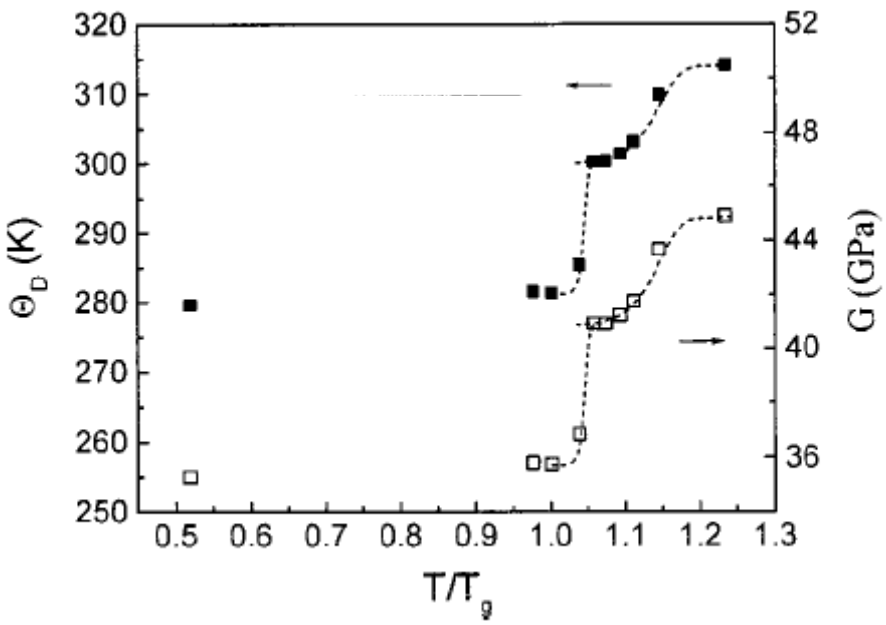

Figure 1.10: Dependence of shear modulus G and Debye temperature θ_D on annealing temperature (Wang, 2000).

rather than densification. Harms et al. investigated the effect of annealing and plastic deformation on the density and moduli of $Pd_{40}Cu_{30}P_{20}Ni_{10}$ and also found that the relative change in the shear modulus is much larger than that in the density (Harms, 2003).

Ichitsubo et al. investigated the elastic properties of $Zr_{55}Cu_{30}Al_{10}Ni_5$ BMG at high temperatures (Ichitsubo, 2003). As shown in Figure 1.11, the elastic constants of as-cast samples decrease monotonically upon warming and then jump up around T_g due to structural relaxation in the heating process. Such jump does not occur in the cooling and subsequent heating processes. The temperature dependence of the ultrasonic attenuation is shown in Figure 1.12. Upon heating, a prominent attenuation peak occurs near T_g due to atomic movements.

Wang's group in China studied the pressure dependence of the elastic response of various BMGs, including Zr-based (Wang, 1999), Pd-based (Wang, 2003a), Nd-based (Zhang, 2003) and Ce-based BMGs (Zhang, 2005). Zr-based, Pd-based and Nd-base BMGs show normal behavior, i.e. the elastic constants and Debye temperature increase slightly with

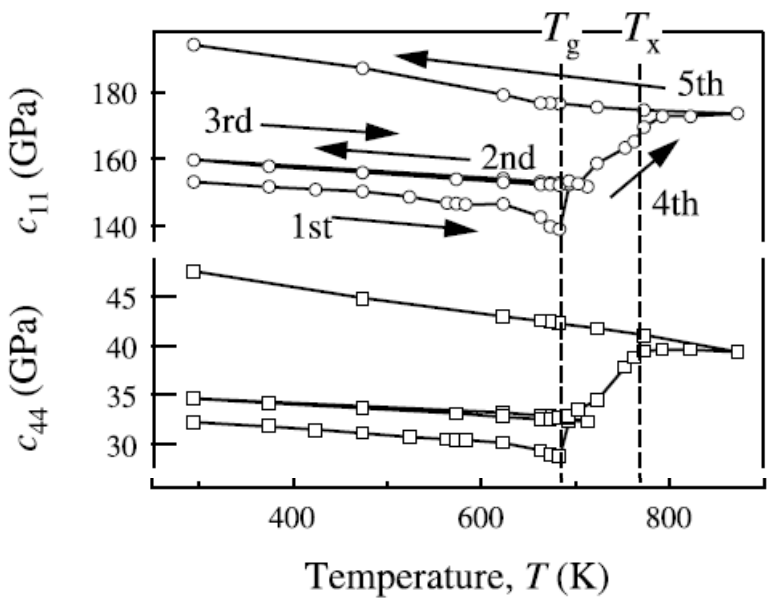

Figure 1.11: Changes in the elastic constants in the heating and cooling processes (Ichitsubo, 2003).

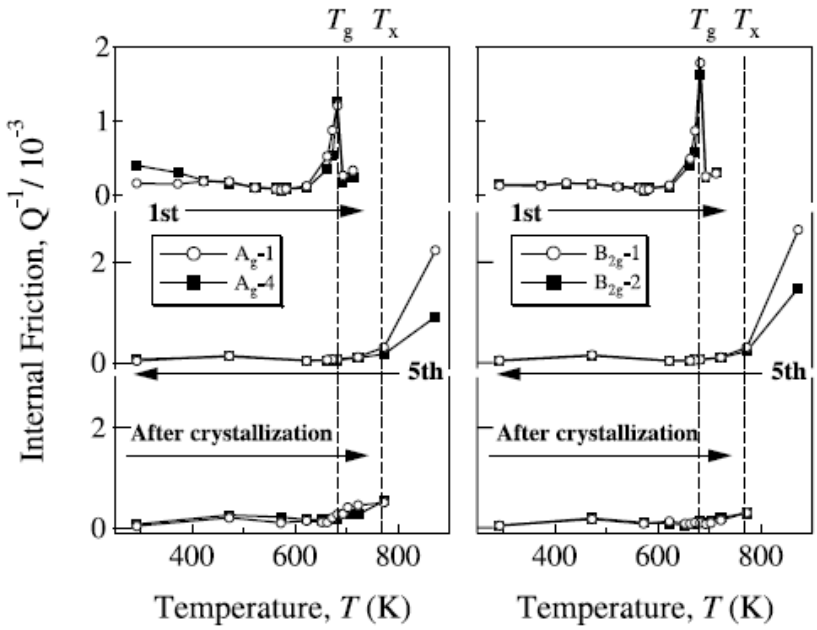

Figure 1.12: Changes in the ultrasonic-attenuation coefficients in the heating and cooling processes (Ichitsubo, 2003).

increasing pressure, as shown in Figure 1.13 and Figure 1.14, respectively (Wang, 1999). The increase in elastic constants is attributed to the denser packing of the metallic glasses. On the other hand, Ce-based BMGs show unusual behavior (Zhang, 2005): with increasing pressure, shear modulus increases, but bulk modulus and Poisson ratio decrease. It is suggested that in the Ce-based BMGs, the local structure typical of regular BMGs may coexist with the covalent bonding structure typical of oxide glasses.

The composition dependence of the elastic properties has been widely studied (Wang, 2006) (Gu, 2006) (Duan, 2007) (Zhang, 2007a) (Duan, 2008). Recent attempts to "predict" the elastic moduli of novel BMGs have explored to what extent the elastic constants of the glasses can be regarded as a weighted average of the moduli of the constituent crystalline elements. These calculations are based on the concept of the property of a glass being an average, restricting consideration to systems in which all the constituent elements are metallic. The averages of the moduli can be obtained by atomic fraction or volume fraction.

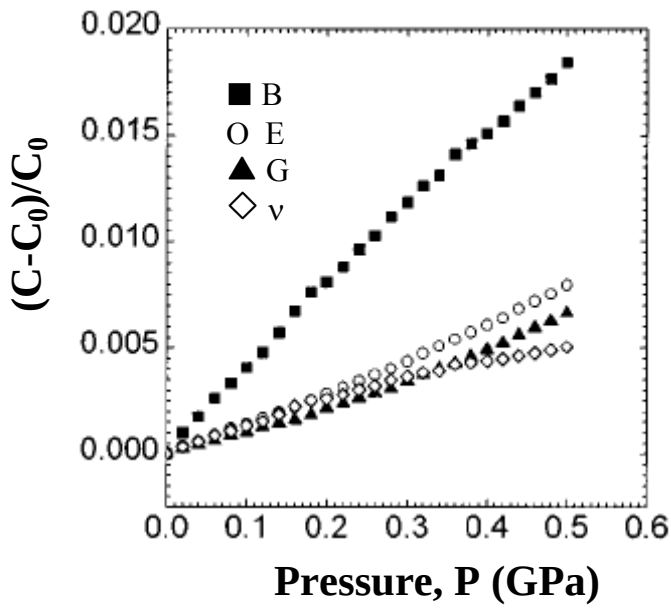

Figure 1.13: Variation of elastic constants C of $Zr_{41}Ti_{14}Cu_{12.5}Ni_9Be_{22.5}C_1$ with pressure *P*. *C* is normalized by $(C-C_0)/C_0$, where C_0 is a normal modulus at ambient P_0 (Wang, 1999).

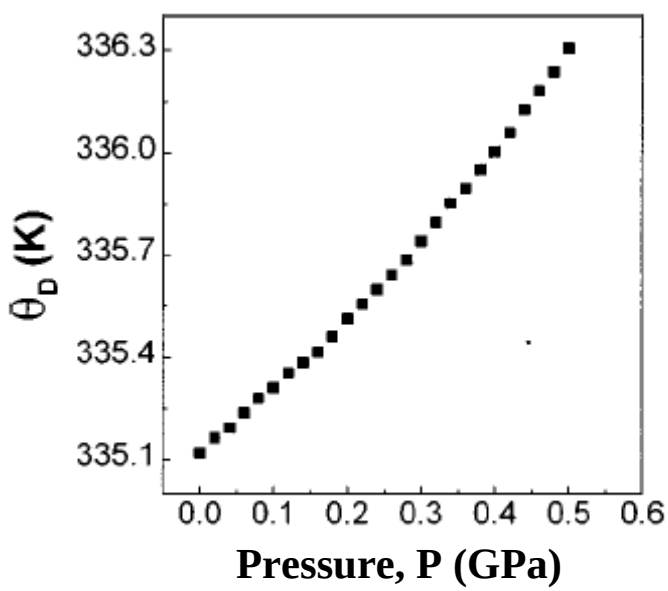

Figure 1.14: Dependence of Debye temperature on the pressure in $Zr_{41}Ti_{14}Cu_{12.5}Ni_9Be_{22.5}C_1$ (Wang, 1999).

Wang's group in China showed that the elastic constants of BMGs can be estimated using

$$C = \frac{1}{\sum x_{ai} C_i^{-1}} \tag{1.15}$$

where the sum is taken over all constituent elements of the BMG, x_{ai} is the atomic fraction of the constituent element and C_i is elastic constant of the corresponding constituent element of the material (Zhang, 2003) (Zhang, 2004) (Wang, 2006). Based on the evaluation of 21 BMGs, including Zr-, Nd-, Pd-, La-, Cu-, Pr-, Mg-, Gd-, Ni-, Ce-, and Er-based BMGs, the ratio of calculated elastic constants to experimental results was found to be in the range of 0.93 to 1.2. It provides useful guidelines for the development of BMGs with desirable properties by properly selecting constituents.

Based on composite mechanics, Zhang and Greer proposed that the elastic constants of BMGs can be estimated by averaging the elastic constant of the constituent elements by volume fraction (Zhang, 2007a). Assuming uniform strain, the elastic constants of BMGs can be estimated using

$$C = \sum x_{vi} C_i \tag{1.16}$$

where the sum is taken over all constituent elements of the BMG, x_{vi} is the volume fraction of the constituent element and C_i is elastic constant of the corresponding constituent element of the material. It is expected to give an upper limit for the expected elastic constants of a given BMG. On the other hand, assuming uniform stress, the elastic constants of BMGs can be estimated using

$$C = \frac{1}{\sum x_{vi} C_i^{-1}} \tag{1.17}$$

with x_{vi} and C_i as defined above. It is expected to give a lower limit for the expected elastic constants of a given BMG. Good correlations between the estimated elastic moduli and the measured values have been found. However, the averaging techniques have to be used with caution, as it has been shown that they sometimes fail to provide an accurate estimate for BMGs (Gu, 2006).

1.3.2 Relationship between elastic constants and mechanical properties

The ductility of crystalline materials is known to be correlated to the ratio of the elastic shear modulus to the bulk modulus *G/B*, which is in turn related to the Poisson ratio ν (Pugh, 1954) (Kelly, 1967) (Rice, 1974) (Hecker, 1978). In crystalline materials, plastic deformation involves the motion of dislocations on close-packed planes. The bulk modulus *B* is related to the surface energy, which in turn is related to the brittle fracture strength (Elliott, 1947). In crystalline materials, brittle fracture involves the tensile separation of non-close-packed atomic planes caused by the propagation of cracks through grains or along the grain boundaries. A low *G/B*, or high ν, is a good phenomenological indicator of inherent ductility. For ideally brittle materials, the fracture energy G_f, i.e. the energy required to create two new fracture surfaces, is twice the surface energy per unit area. Under plane strain, the fracture energy G_f is

$$G_f = \frac{K^2(1-\nu^2)}{E} \tag{1.18}$$

where K is the stress intensity, E is the Young's modulus and ν is the Poisson ratio (Irwin, 1957) (Knott, 1973).

A similar assessment for metallic glasses was not available until recently. The fracture toughness K_{Ic} of BMGs was first reported in 1997 (Conner, 1997) (Gilbert, 1997). $K_{Ic} \approx$ 55 MPa·m$^{1/2}$ for amorphous $Zr_{41.2}Ti_{13.8}Cu_{12.5}Ni_{10}Be_{22.5}$, comparable to that of high strength steel and aluminum alloys. After heat treatment at temperatures above T_g, crystallization occurred, leading to drastic reduction of K_{Ic} to ~1 MPa·m$^{1/2}$ (Gilbert, 1997). Wesseling et al. investigated $Cu_{60}Zr_{20}Hf_{10}Ti_{10}$ BMG and reported that K_{Ic}> 65 MPa·m$^{1/2}$ (Wesseling, 2004). At temperatures between $0.7T_g$ and $0.8T_g$, significant softening occurs, indicated by a drastic decrease in hardness, as shown in Figure 1.15 (Wesseling, 2004). It is expected that homogeneous deformation of metallic glasses occurs at $T > 0.6T_g$.

Schroers and Johnson prepared $Pt_{57.5}P_{22.5}Cu_{14.7}Ni_{5.3}$ BMG, which showed 20% plastic strain in compression, more than 3% strain to failure during bending, and a high fracture toughness, $K_{Ic} \approx$ 80 MPa·m$^{1/2}$ (Schroers, 2004). The large ductility is caused by the

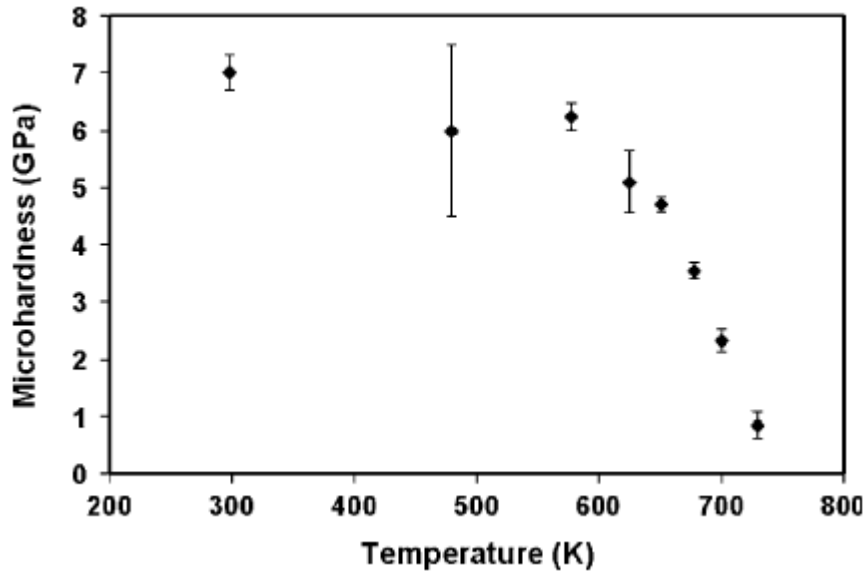

Figure 1.15: Microhardness versus temperature for $Cu_{60}Zr_{20}Hf_{10}Ti_{10}$ BMG (Wesseling, 2004).

formation of very dense shear bands. The high Poisson ratio, ν=0.42, leads to the extension of a shear band, rather than the initiation of a crack. Therefore, deformation is achieved by the formation of multiple shear bands, resulting in large global ductility and high fracture toughness. The deformation changes from inhomogeneous to homogenous during heating and large plasticity is exhibited in the vicinity of the glass transition temperature T_g. BMGs with low T_g (ie. close to room temperature where mechanical properties are typically determined), are more likely to exhibit room temperature ductility. It has been suggested that a large Poisson ratio and a low glass transition temperature might be regarded as indicators of the ductile character of a bulk metallic glass and could therefore be used as a means of identifying ductile BMGs.

Xi et al. reported a correlation between the fracture toughness K_{Ic} and the plastic zone size w for various BMGs, as shown in Figure 1.16 (Xi, 2005). The plastic zone size w can be calculated using

$$w = 0.025\left(\frac{K_{Ic}}{\sigma_y}\right)^2 \tag{1.19}$$

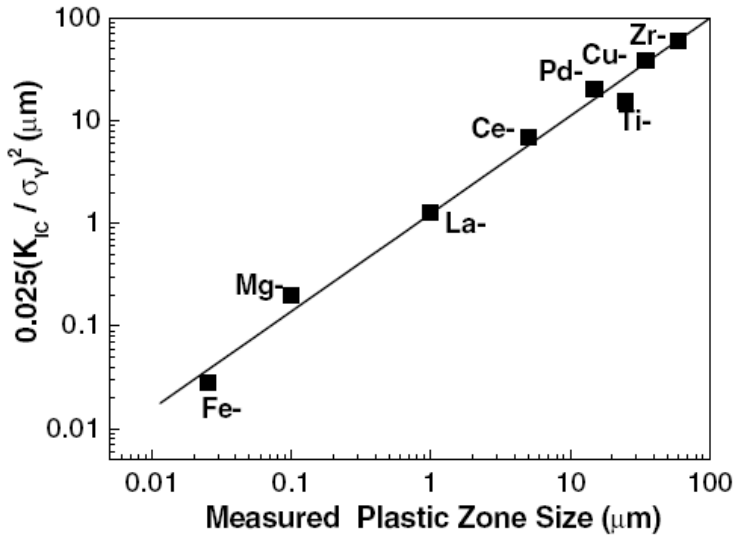

Figure 1.16: Fracture toughness or strength response to the plastic process zone size (Xi, 2005).

where σ_y is the yield strength. K_{Ic} is ~10 MPa·m$^{1/2}$ for $Ce_{70}Al_{10}Ni_{10}Cu_{10}$ and ~2 MPa·m$^{1/2}$ for $Mg_{65}Cu_{25}Tb_{10}$. With increasing K_{Ic}, w increases, indicating better ductility. It was shown that the fracture in brittle glasses also proceeds by the local softening mechanism, similar to the tough glasses, but at different length scales.

Lewandowski *et al.* reported a universal correlation between the fracture energy G_f and the Poisson ratio ν for metallic glasses (including Mg-, Ce-, Fe-, Zr-, Cu-, Pd-, and Pt-based BMGs) and oxide glasses as shown in Figure 1.17, with ductile glasses displaying a high Poisson ratio (Lewandowski, 2005). The transition from tough to brittle regimes is in the range ν=0.31-0.32.

The mechanical and physical properties of 35 BMGs, including Zr-, Ti-, Cu-, Pd-, Fe-, Ni-, Co-, W-, Mg-, La-, Ce-, Nd-, Pt-, Al- and Ca-based BMGs, were examined (Wang, 2005). Good correlation of fracture strength σ and Vickers hardness H_v with Young's modulus E were found with $\sigma \approx E/50$ and $H_v \approx E/20$, as shown in Figure 1.18. The fracture strength of BMGs ~ $E/50$ is close to the theoretical strength ~ $E/5 - E/10$ (Greer, 1995) and higher than that of crystalline materials (Wang, 2005).

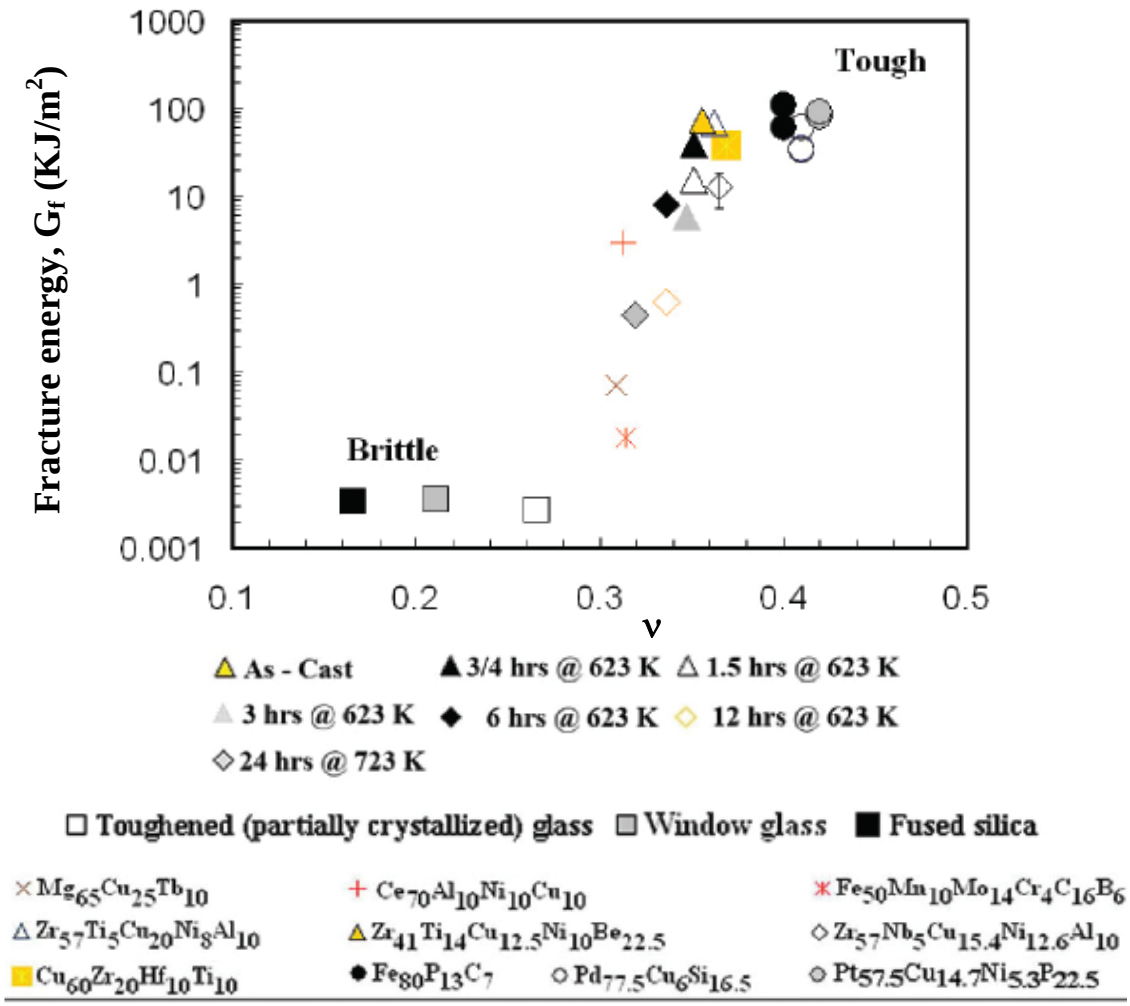

Figure 1.17: The correlation of fracture energy G_f with Poisson ratio ν for metallic glasses (as-cast and annealed) and oxide glasses (Lewandowski, 2005).

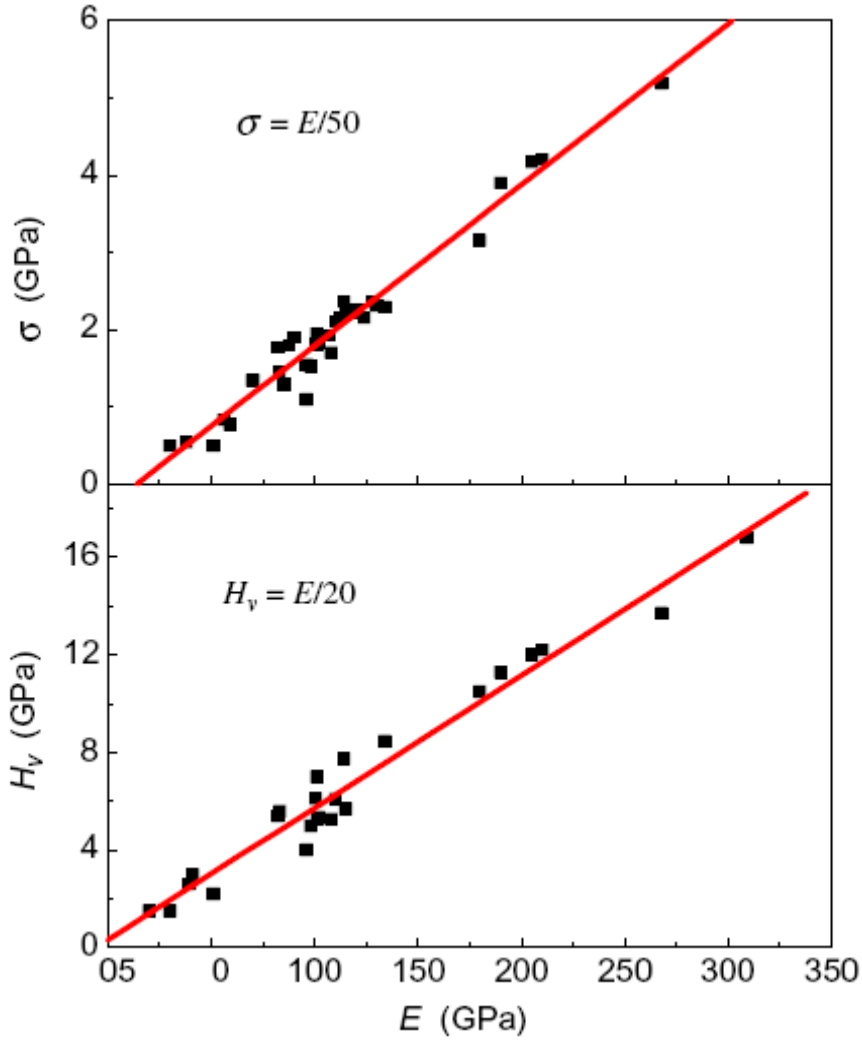

Figure 1.18: Correlation of fracture strength σ and Vickers hardness H_v with Young's modulus E for various BMGs (Wang, 2005).

Inoue et al. compared Cu-, Zr-, Pd-, Mg-, La-based BMGs with conventional structural materials, including Ti alloy, Mg alloy, stainless steel, super high strength steel and Duralumin in terms of σ/E and H_v/E and found that BMGs have higher values, as shown in Figure 1.19 (Inoue, 2002). Based on room temperature elastic constants and compressive yield stresses for ~30 metallic glasses including Zr-, Pd-, Ni-, Cu-, Pd-, Pt-, Mg-, Ce-, Cu-, Fe- and Au-based BMGs, Johnson et al. reported that yielding can be described by a critical shear strain $\gamma_C = \tau_Y / G = 0.0267 \pm 0.0020$ with τ_Y the shear stress at yielding and G the shear modulus (Figure 1.20) (Johnson, 2005). Based on the concept of inherent states and potential energy landscapes, a cooperative shear model was developed, leading to a universal criterion for plastic yielding of metallic glasses with $\gamma_C \propto (T/T_g)^{2/3}$.

Using molecular dynamics simulations, the dependence of the elastic properties on configurational changes in Cu–Zr BMGs was studied (Duan, 2006). The simulation results are consistent with the experimental results reported by Lind et al. (Lind 2006), who measured the isoconfigurational elastic constants of $Zr_{46.25}Ti_{8.25}Cu_{7.5}Ni_{10}Be_{27.5}$ using the pulse-echo overlap technique. The samples were isothermally annealed and quenched near the glass transition temperature. It was found that the shear modulus G has a strong dependence on annealing temperatures and, thus, on the specific configurational potential energy of the equilibrium liquid.

1.3.3 Correlation of elastic constants with Tg and GFA

Egami proposed a correlation between the glass transition temperature T_g and the bulk modulus B, as

$$\frac{T_g k_B}{2BV} = (\varepsilon_v^{crit})^2 \tag{1.20}$$

where V is the average local volume, k_B is Boltzmann constant and ε_v^{crit} is the critical volume strain ~0.0554, assuming that the atomic level stresses are totally localized and the stresses at neighboring sites are uncorrelated (Egami, 1984) (Egami, 1997). When the system is frozen, a long-range stress field is produced and the glass transition temperature

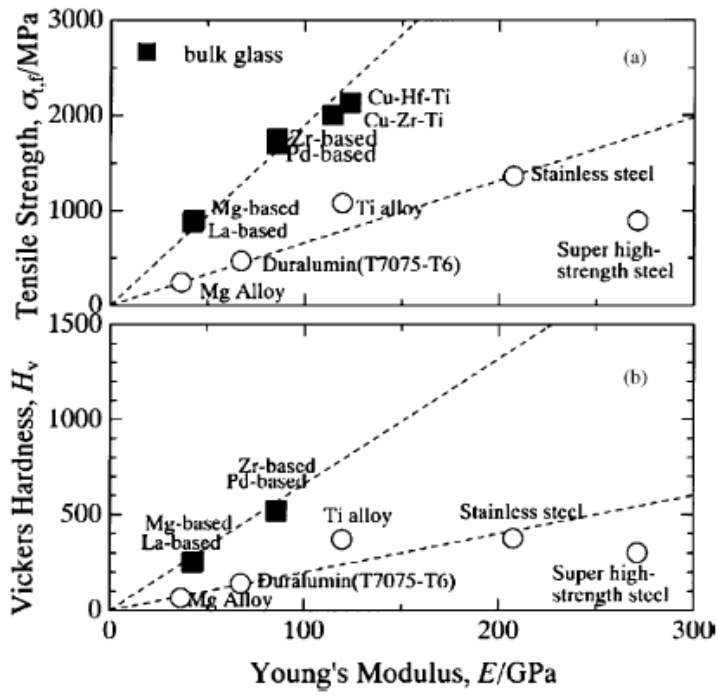

Figure 1.19: Relationship between mechanical properties of typical BMGs with Young's modulus E. (a) Tensile fracture strength vs. E; (b) Vickers hardness vs. E (Inoue, 2002).

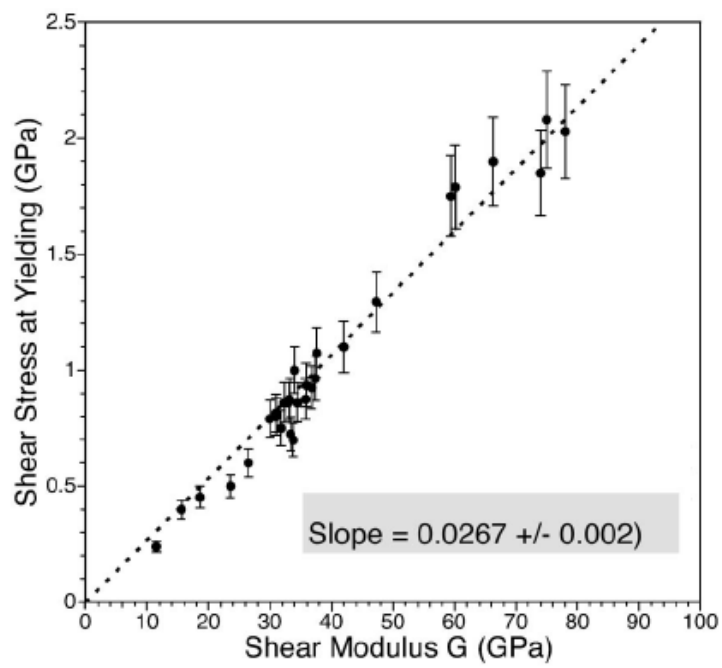

Figure 1.20: Experimental shear stress at yielding, τ_Y vs. shear modulus G at room temperature for ~30 bulk metallic glasses (Johnson, 2005).

T_g depends not only on bulk modulus B but also on Poisson ratio ν,

$$\frac{T_g k_B}{2BV} = \frac{2(1-2\nu)(\varepsilon_v^{T,crit})^2}{3(1-\nu)} \tag{1.21}$$

where $\varepsilon_v^{T,crit}$ is the critical transformation volume strain ~0.095 (Egami, 2007). The predicted glass transition temperature using Equation 1.21 is in good agreement with experimental results in metallic glasses, as shown in Figure 1.21. An empirical linear relationship between T_g and Young's modulus E for 35 metallic glasses, shown in Figure 1.22, was reported by Wang (Wang, 2005). A correlation between T_g or T_x and the elastic constants E, B and G has been reported for rare earth based BMGs, as shown in Figure 1.23 (Wang, 2006) (Li, 2008).

According to the Lindemann melting criterion, T_m is related to Debye temperature θ_D

$$T_m = M_a k_B \theta_D^2 < u^2 > /(9h^2) \tag{1.22}$$

where M_a is the average atomic mass, h is Planck constant and u is the oscillation displacement. Correlation of T_m and T_g with θ_D^2 was reported, and a relationship between T_g and the shear modulus G was shown for 32 metallic glasses (Wang, 2003b).

Novikov and Sokolov analyzed a large number of glasses, including covalent and hydrogen-bonded, Van der Waals, and ionic glasses, and reported the ratio of instantaneous bulk to shear bulk modulus B/G in glasses (or Poisson ratio ν) is linked to the fragility of the glass-forming liquid, as shown in Figure 1.24 (Novikov, 2004). With increasing B/G or ν, the fragility index m increases, indicating larger fragility and poorer glass forming ability. Novikov and Sokolov's work is quite controversial. It was shown that when more glasses are examined, including organic, inorganic and metallic glasses, the correlation between melt fragility and elastic properties is poor (Battezzati, 2005) (Yannopoulos, 2006) and that increasing m will lead to a decreasing Poisson ratio (Johari, 2006).

Wang investigated 18 metallic glasses, including Zr-, Cu-, Pd-, Pt-, Ce-, Pr-, Gd-, La-,

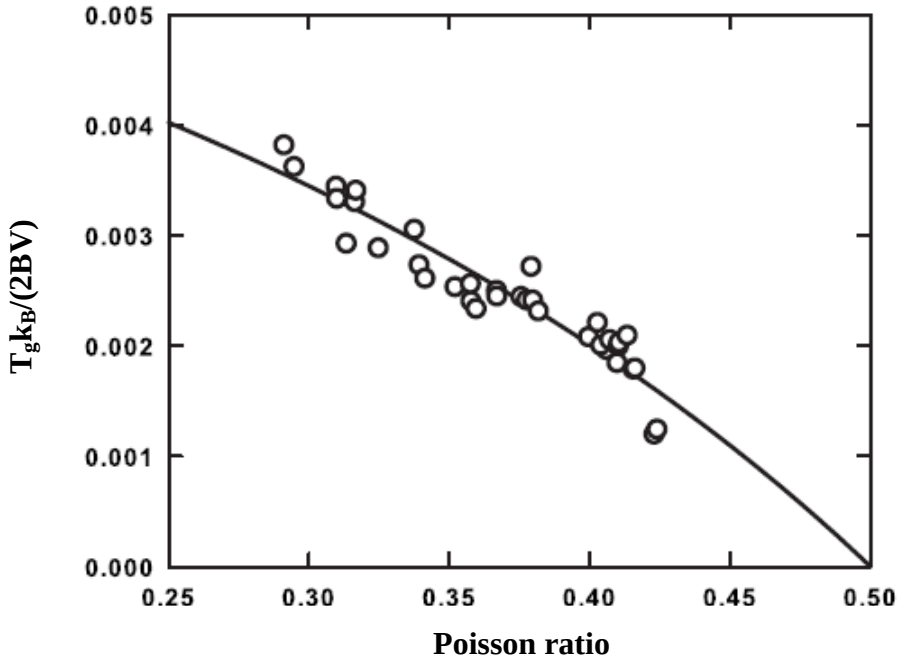

Figure 1.21: Glass transition temperature T_g multiplied by $k_B/(2BV)$ as a function of Poisson ratio for various metallic glasses. The solid line indicates $\frac{2(1-2\nu)(\varepsilon_v^{T,crit})^2}{3(1-\nu)}$ with $\varepsilon_v^{T,crit}$=0.095 (Egami, 2007).

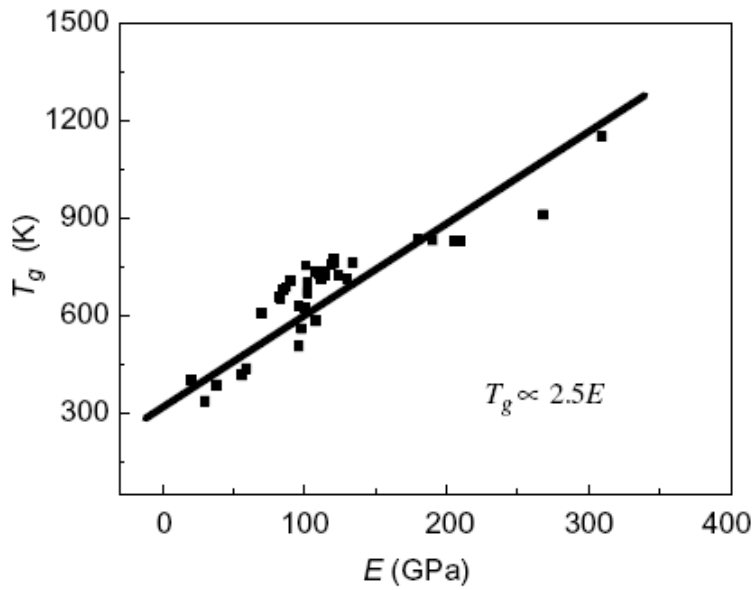

Figure 1.22: Correlation between glass transition temperature T_g and Young's modulus E for various BMGs (Wang, 2005).

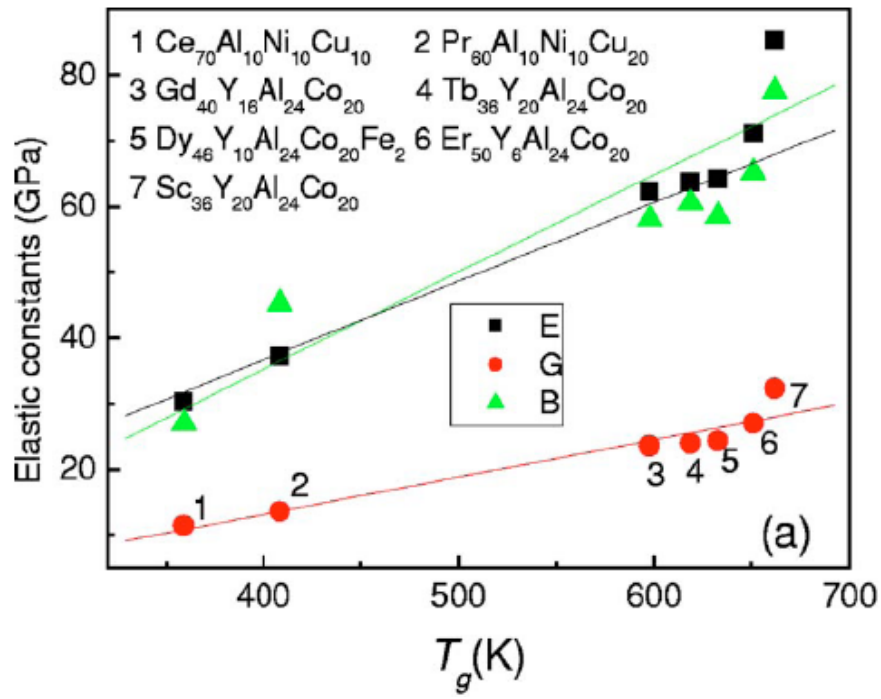

(a)

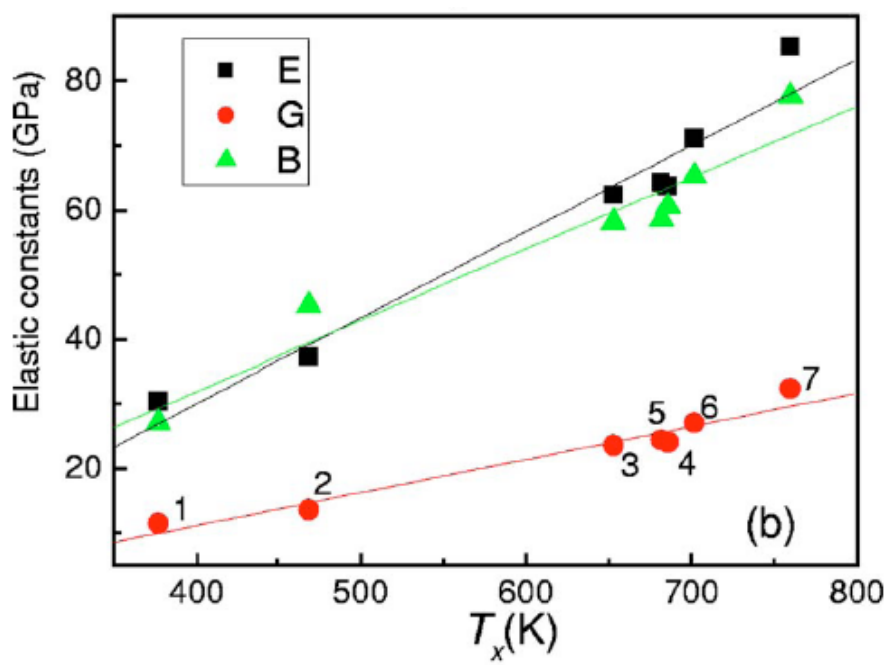

(b)

Figure 1.23: The correlation of elastic constants with T_g and T_x for rare-earth based BMGs (Wang, 2006).

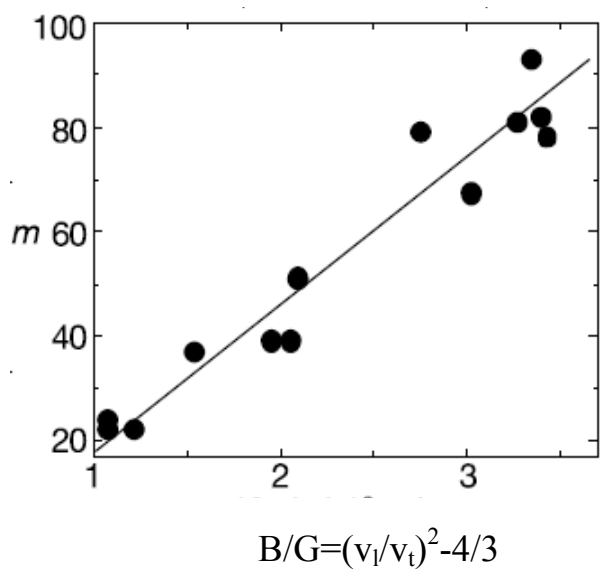

Figure 1.24: Correlation of fragility with the ratio of the bulk and shear moduli in the glassy state (Novikov, 2004).

Nd-, Mg-, Fe-, and Ho-based BMGs, and found a weak correlation between m and B/G, as shown in Figure 1.25 (Wang, 2006). A rough correlation was found between Poisson ratio ν and critical cooling rate R_c, with BMGs that display a high ν showing poor GFA. Novikov and Sokolov reported similar results, shown in Figure 1.26 (Novikov, 2006). The difference between metals and non-metals is due to the free electron gas, which leads to an additional contribution to the bulk modulus B of metallic glasses. The energy of the free electron gas E_{el} only depends on its density and is insensitive to structure rearrangements during structural relaxation at a fixed volume V. On the other hand, the shear modulus is insensitive to the free electron gas, since shear strain does not change the volume. In metallic glasses, $B=B_{el}+B_{lat}$, with B_{lat} the lattice contribution and $B_{el} = V\partial^2 E_{el} / \partial V^2$. In nonmetallic glasses, $B=B_{lat}$. Therefore, the linear correlation between m and B/G in metallic glasses has a slope that is lower than that in nonmetallic glasses by a factor $B_{lat}/(B_{lat}+B_{el})$.

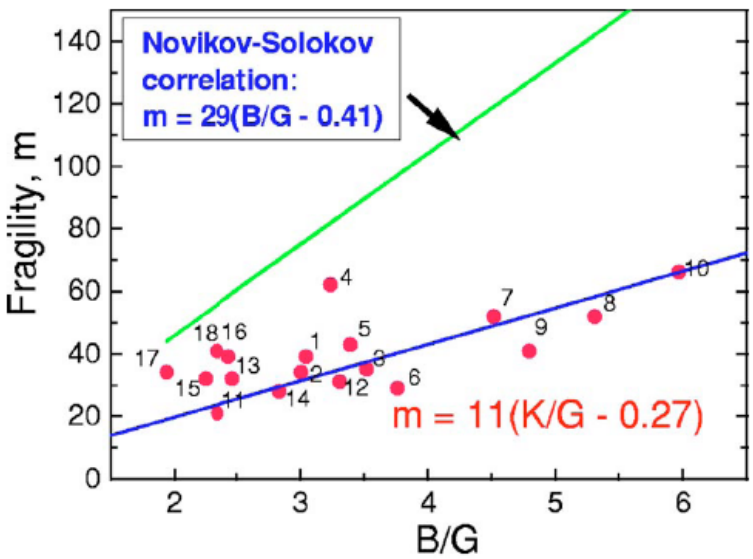

Figure 1.25: Correlation between fragility of liquids m and the ratio of instantaneous bulk to shear modulus *B/G* for metallic glasses (Wang, 2006).

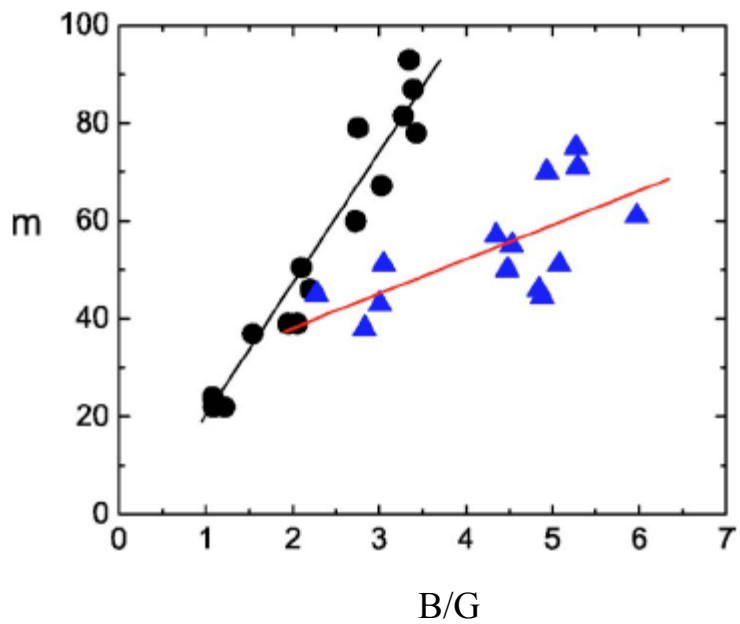

Figure 1.26: Correlation between fragility of liquids *m* and the ratio of instantaneous bulk to shear modulus *B/G* of respective glasses. Circles – data for nonmetallic glass formers. Triangles – data for metallic glass formers. Solid lines – linear fits (Novikov, 2006).

1.3.4 The physics of elastic properties

The elastic properties of a given material are linked to its atomic bonding and thermal expansion. The dependence of the potential energy U and the force F on the interatomic distance r is shown in Figure 1.27 (Kittel, 1986) (Shelby, 1997).

$$F = \frac{\partial U}{\partial r} \tag{1.23}$$

When r is large, the atoms do not exert any force on each other. With decreasing r, an attractive force acts, pulling atoms closer. When r decreases further, a repulsive force kicks in. F=0 (and U is minimized) at the equilibrium interatomic distance r_0. The energy at r_0, U_0, is the bonding energy, i.e. the energy required to separate the atoms. Typically, materials with high bonding energy also display high melting temperature. According to Hooke's law, the elastic constant C is the derivative of force and second derivative of elastic energy with respect to the interatomic distance as follow.

$$C = -\frac{\partial F}{\partial r} = -\frac{\partial^2 U}{\partial r^2} \tag{1.24}$$

With increasing temperature, the interatomic distance increases due to higher kinetic energy (see below), and the curve of the force vs. interatomic distance becomes flattened, leading to decreasing elastic constant.

The asymmetry of potential energy vs. interatomic distance leads to thermal expansion, as shown in Figure 1.28 (Mohazzabi, 1997). Adjacent atoms in a solid typically behave as if they were connected by tiny springs. The amplitude of an oscillation is taken to be the horizontal distance between two points of equal potential energy. With increasing temperature, the kinetic energy increases, and the atoms vibrate with greater amplitude. The average interatomic distance increases, leading to thermal expansion. The thermal expansion is related to elastic modulus as follows (Schreiber, 1974),

$$\alpha = \frac{\gamma_G C_P \rho}{3B_s} \tag{1.25}$$

where α is the linear expansion coefficient, B_s is the adiabatic bulk modulus, C_P is the specific heat at constant pressure, ρ is the density, and γ_G is the Grüneisen constant,

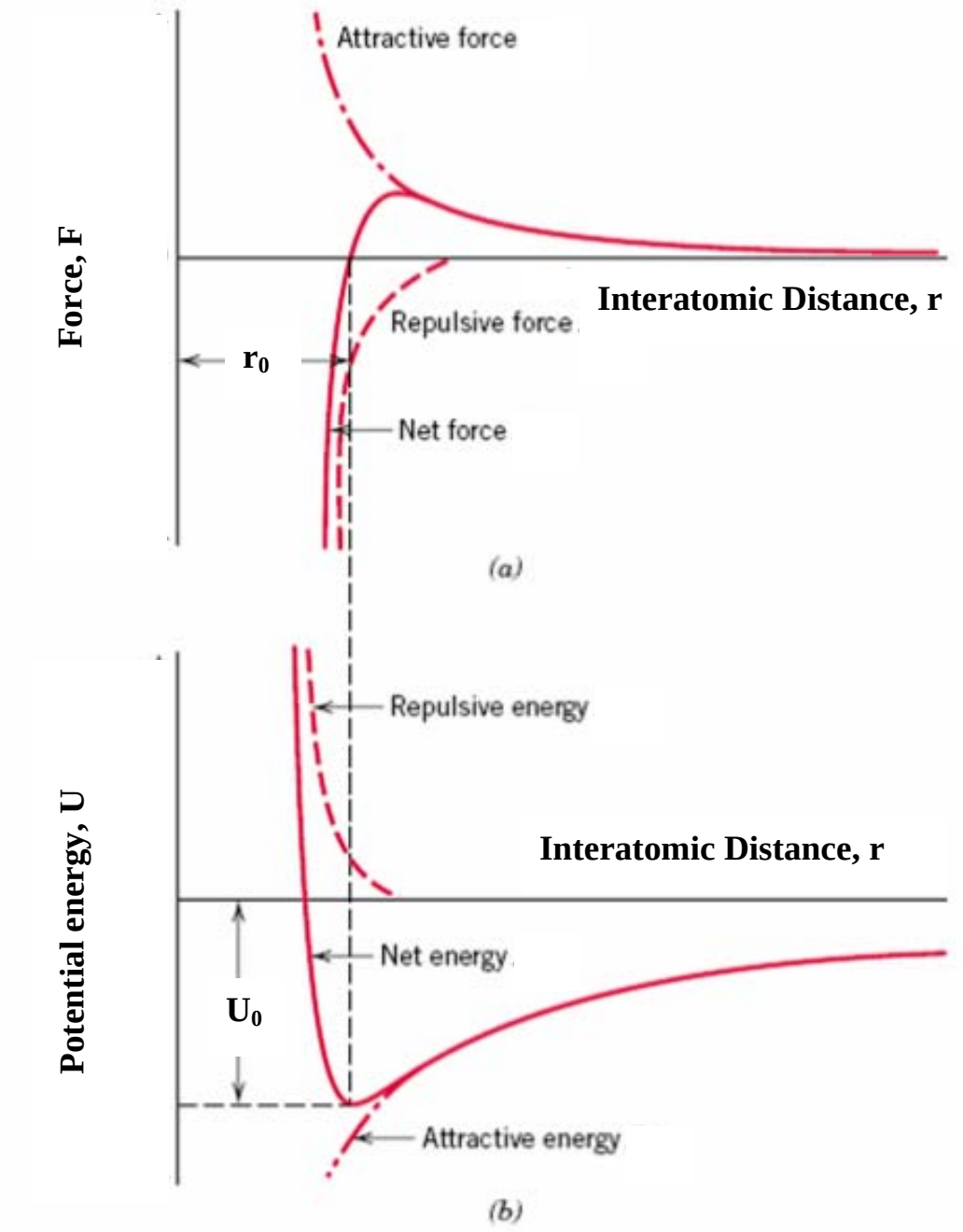

Figure 1.27: Dependence of force *F* and potential energy *U* on interatomic distance *r*. (a) *F* vs. *r*. (b) *U* vs. *r* (Kittel, 1986) (Shelby, 1997).

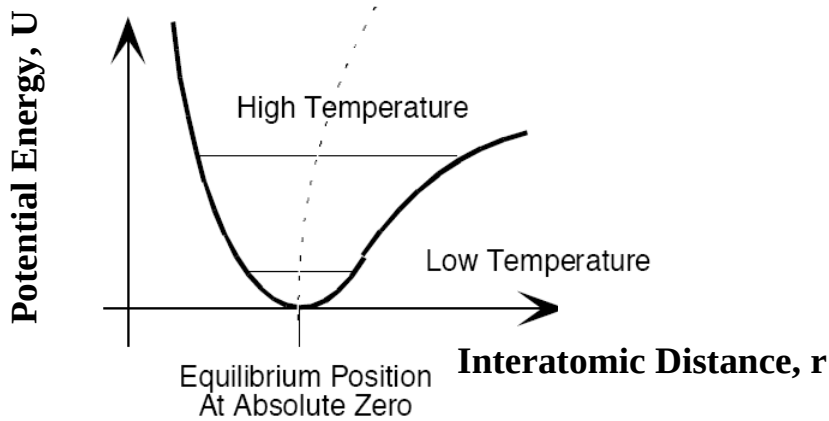

Figure 1.28: Schematic relationship between potential energy U and interatomic distance r at different temperatures (Mohazzabi, 1997).

$$\gamma_G = \frac{-d\ln\theta_D}{d\ln V} = \frac{-V}{\theta_D}\frac{d\theta_D}{dV} \tag{1.26}$$

with θ_D the Debye temperature and V the volume.

Materials with strong bonds usually display high elastic modulus. The shear modulus G is defined as follows,

$$G = \frac{\tau}{\gamma} \tag{1.27}$$

where τ is the shear stress and γ is the shear strain. It indicates the resistance to shear deformation, which involves no change in volume, only a change in shape. The bulk modulus B indicates the resistance to a volume change $\frac{\Delta V}{V}$, and it is defined as follows,

$$B = -\frac{PV}{\Delta V} \tag{1.28}$$

where P is the pressure. It provides a good link between thermodynamics and elasticity theory. The behavior of bulk modulus can be quite different from that of shear modulus; e.g. temperature has typically a much larger effect on shear modulus than on bulk modulus. The existence of free electrons in metals and alloys makes them hard to be

compressed, but easy to shear, leading to smaller changes in bulk modulus than in shear modulus.

Usually when the material is stretched in one direction, it will expand in the other two directions. The Poisson ratio is defined as,

$$\nu = -\frac{\varepsilon_x}{\varepsilon_y} \tag{1.29}$$

with ε_y the strain along the stress-applying direction and ε_x the strain along the perpendicular direction. ν is always in the range between -1 and 0.5, and is close to zero for cork, close to 0.5 for rubber and equal to 0.5 for liquid. The auxetic materials have negative Poisson ratio. The microscopic reason for Poisson's effect is due to atomic movements and stretching of bonds to accommodate the stress. When the bonds elongate in the stress direction, they shorten in the other directions. Noble metals such as Pd and Au are known to have a high Poisson ratio, ~0.39. This is due to their electronic configuration. For example, Pd has the electronic configuration, $1s^2 2s^2 2p^6 3s^2 3p^6 4s^2 3d^{10} 4p^6 5s^0 4d^{10}$, with a full d shell. The d-electrons make it hard to change volume but easy to shear, leading to high Poisson ratio.

CHAPTER 2

EXPERIMENTAL DETAILS

In this work, the elastic properties of bulk metallic glasses (BMGs) have been studied using resonant ultrasound spectroscopy (RUS). This chapter will focus on the RUS technique, including its development, principle and setup. In addition, the sample preparation and data analysis will be described.

RUS is a relatively new technique for determining the complete elastic tensor of a solid by measuring its free-body resonances (Migliori, 1993) (Migliori, 1997). The mechanical resonances can be calculated for a sample with known dimensions, density, and elastic tensor, which is known as the "forward problem". In a RUS experiment, the mechanical resonances of a freely vibrating solid of known shape are measured, and an iteration procedure is used to "match" the measured frequencies with the calculated spectrum, i.e. solving the inverse problem. This allows determination of the full elastic tensor of the solid from a single frequency scan, which clearly indicates a main advantage of RUS: there is no need for separate measurements to probe different moduli, and multiple sample remounts and temperature sweeps are avoided. Another advantage lies in the ability of RUS to work with small samples: RUS measurements can be made on mm-sized samples.

RUS is based on the measurement of the vibrational eigenmodes of samples of well defined shapes, usually parallelepipeds, cylinders or spheres. The vibrational eigenmodes of a three-dimensional object are rather complicated. Figure 2.1 shows some example of the calculated eigenmodes for a rectangular parallelepiped (Leisure, 1997). Although the methods used in RUS can be traced back to more than one hundred years ago, RUS has received wide interest only with the increasing availability of powerful computers.

The first RUS measurement was done in 1964 by Frasier and LeCraw (Fraser, 1964), who used the analytic solutions to the forward problem for a sphere of isotropic material

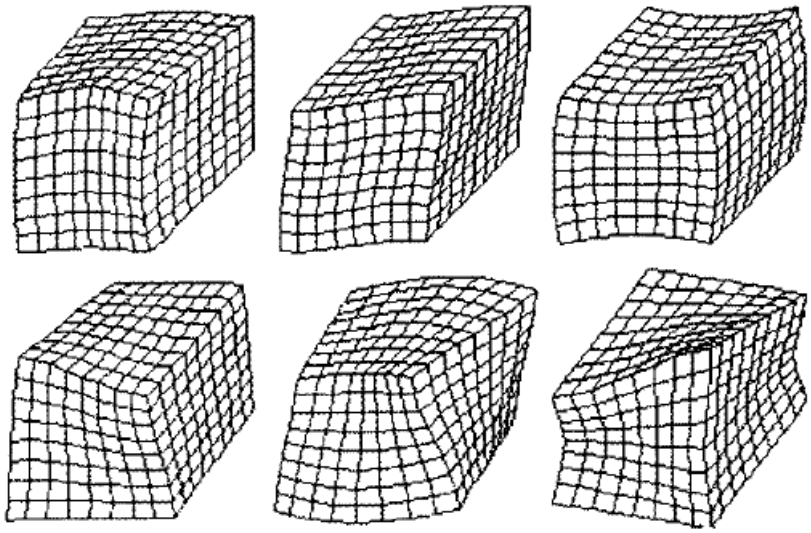

Figure 2.1: An illustration of several vibrational eigenmodes for a rectangular parallelepiped (Leisure, 1997).

and inverted graphically. In 1970, Anderson, Schreiber and their coworkers improved the method, applied it to spherical lunar rock samples and compared the observed low sound velocities to those in various cheeses (Schreiber, 1970a) (Schreiber, 1970b). In 1971, Demarest determined the elastic constants of an isotropic cube and reported that the method can be used not only for spheres of isotropic materials, but also for rectangular parallelepiped anisotropic crystalline materials (Demarest, 1971). In 1976, Ohno further improved the method and used it to determine the elastic constants of orthorhombic crystals (Ohno, 1976). Finally, Migliori, Visscher et al. extended the use of this method from the geophysics community to the general physics community, introduced the computer algorithms and proposed the term "resonant ultrasound spectroscopy" (Migliori, 1990a) (Migliori, 1990b) (Visscher, 1991) (Migliori, 1993) (Migliori, 1997).

The basic physics is generalized in Hooke's law. For the one-dimensional case,

$$\sigma = c\varepsilon = c\frac{du}{dx} \tag{2.1}$$

where σ is the applied stress, c is the elastic constant, ε is the resulting strain, and u is the displacement. For a three-dimensional case,

$$\sigma_{ij} = \sum_{k=1}^{3}\sum_{l=1}^{3} c_{ijkl}\varepsilon_{ij} \tag{2.2}$$

where c_{ijkl} is the elastic constant tensor. The number of independent elastic constants is 21 for samples with triclinic symmetry, but is reduced significantly for materials with higher symmetry: cubic materials have three independent elastic constants, and isotropic materials have only two independent elastic moduli.

The elastic constants of a material can be determined by measuring the sound velocities in it and the relations for a cubic material are as follows,

$$v_l = \sqrt{\frac{c_{11}}{\rho}} \tag{2.3}$$

$$v_{T_1} = \sqrt{\frac{c_{44}}{\rho}} \tag{2.4}$$

$$v_{T_2} = \sqrt{\frac{c_{11} - c_{12}}{2\rho}} \tag{2.5}$$

where v_l is the longitudinal sound velocity, v_{T_1} and v_{T_2} are the transverse sound velocities, c_{11} is the longitudinal modulus and c_{44} and $(c_{11}-c_{12})/2$ are the shear moduli.

For an object with a free surface S surrounding a volume V, the general form of the Lagrangian is as follows,

$$L = \int_V (KE - PE)dV = \int_V \left(\frac{1}{2}\sum_i \rho\omega^2 u_i^2 - \frac{1}{2}\sum_{i,j,k,l} c_{i,j,k,l} \frac{\partial u_i}{\partial x_j}\frac{\partial u_k}{\partial x_l} \right) dV \tag{2.6}$$

where KE is the kinetic energy, PE is the potential energy, ω is the angular frequency, ρ is the density, c_{ijkl} is the elastic tensor, u_i is the i-th component of the displacement vector and is assumed to have harmonic time dependence, i.e. $u(t)=u_0e^{i\omega t}$. When u varies arbitrarily in V and on S, the variation in L is as follows,

$$\delta L = \int_V \sum_i \left[\left(\rho\omega^2 u_i + \sum_{jkl} c_{ijkl} \frac{\partial^2 u_k}{\partial x_j \partial x_l} \right) \delta u_i \right] dV + \int_S \sum_i \left[\left(\sum_{jkl} \vec{n}_j c_{ijkl} \frac{\partial u_k}{\partial x_l} \right) \delta u_i \right] dS \tag{2.7}$$

where n_j is the outer normal of the free surface. Therefore, the minima of L with respect to unrestricted variation of u_i occur, when the elastic wave equation in V,

$$\rho\omega^2 u_i + \sum_{jkl} c_{ijkl} \frac{\partial^2 u_k}{\partial x_j x_l} = 0 \tag{2.8}$$

and the free surface boundary conditions,

$$\sum_{jkl} \vec{n}_j c_{ijkl} \frac{\partial u_k}{\partial x_l} = 0 \tag{2.9}$$

are satisfied. The corresponding angular frequencies ω are the normal mode frequencies of the free vibration of the object (Migliori, 1990a) (Visscher, 1991) (Migliori, 1993) (Migliori, 1997).

Using the Rayleigh-Ritz method (Arfken, 1970), the displacement vector is expanded in some suitable set of basis functions,

$$u_i = \sum_{\lambda} a_{i\lambda} \Phi_{\lambda} \tag{2.10}$$

with $a_{i\lambda}$ the expansion coefficient. The normalized Legendre polynomials are usually chosen to be the basis functions to make the eventual matrix elements easy to compute. Therefore,

$$u_i = \sum_{l+m+n \le N} a_{ilmn} P_l(x/b_1) P_m(y/b_2) P_n(z/b_3) \tag{2.11}$$

where P are the Legendre polynomials and $2b_1$, $2b_2$, $2b_3$ are the sample dimensions. By substituting Equation 2.11 into Equation 2.6, L is obtain as follows,

$$L = \frac{1}{2} \vec{a}^T \left(\rho\omega^2 - \Gamma \right) \vec{a} \tag{2.12}$$

where Γ is a matrix of order (N+1)(N+2)(N+3)/2, and $\vec{a}$ is the column vector $\{a_{ilmn}\}$, i=1, 2, 3, and l+m+n≤N. Maximizing Equation 2.12 with respect to a_{ilmn} yields the eigenvalue equation,

$$\Gamma \vec{a} = \rho\omega^2 \vec{a} \tag{2.13}$$

In practice, N is chosen to give a good compromise between computational accuracy and computing time and memory requirements. It is found that N=10 is a reasonable choice.

The size of the matrix is 858×858. However, the matrix can be split into blocks to save the computing time. For a rectangular parallelepiped crystal having orthorhombic or higher symmetry, a tremendous simplification takes place. The largest block is 125×125 for N=10. The eigenvalues ω^2 give the square of the resonant frequencies and the eigenvectors conveniently give the displacements (Migliori, 1990a) (Visscher, 1991) (Migliori, 1993) (Migliori, 1997).

The next step in RUS is to solve the inverse problem, i.e. to determine the elastic constants from the resonant frequencies. Since there is no analytical method, an indirect method is used. The difference between the calculated and measured resonant frequency spectrum is quantified by a figure-of-merit function as follows,

$$F = \sum_{i=1}^{n} w_i \left(\frac{f_i^{cal} - f_i^{mea}}{f_i^{mea}} \right)^2 \tag{2.14}$$

where f_i^{cal} is the i-th calculated frequency, f_i^{mea} is the i-th measured frequency, and n is the number of frequencies. w_i is a weighting factor to reflect the degree of confidence in the measured frequency f_i^{mea}, and it is usually either 0 or 1. Finally, the Levenberg-Marquardt method is used to locate the minimum of F in a multidimensional elastic-constant space (a two-dimensional space in the case of isotropic materials). F is assumed to be a quadratic function of the elastic constants near the minimum, so that the surface of constant F are ellipsoid with major axes related to the accuracy with which the corresponding elastic constants are determined. The accuracy for each elastic constant is estimated by finding the length of the corresponding semi-major axis of the ellipsoid when F exceeds the minimum by 2% (Chu, 1995).

Figure 2.2 shows a schematic diagram of the measurement setup (Chu, 1995). The parallelepiped sample is corner-mounted between two $LiNbO_3$ piezoelectric transducers. The two corners on a body diagonal of the sample touch the transducers. The sample is excited by a signal applied to one of the transducers. The frequency is swept through a range corresponding to a large number of vibrational eigenmodes of the sample. The resonant response of the sample is detected by the receiving transducer. A large response

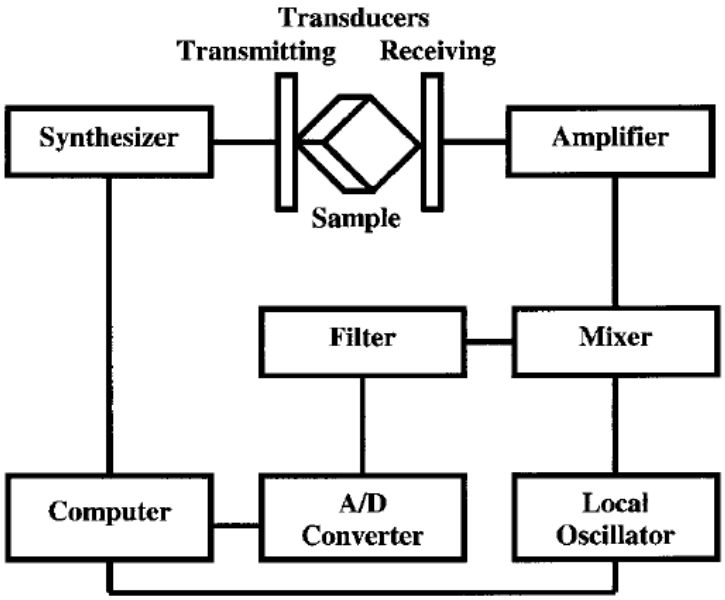

Figure 2.2: Schematic setup of resonant ultrasound spectroscopy (Chu, 1995).

is observed when the frequency of the applied signal corresponds to one of the sample's eigenfrequencies. A typical RUS scan is shown in Figure 2.3. The arrows indicate the resonant frequencies. The transducers apply some force to the sample, so the boundaries are not entirely free. However, it has been found (Migliori, 1993) that if the force applied by the transducer is 0.01 N or less, and the drive voltage is kept low, the shift in eigenfrequencies resulting from this force is of the order of parts per million.

For our studies, samples of approximately 3x3x3 mm^3 are cut from BMG ingots and then polished into rectangular parallelepipeds (RP). The mass and dimensions of each sample are measured and its density is calculated. The sample is mounted between the two transducers of the RUS probe. Measurements as a function of temperature between 5 K and 400 K are performed using a specially designed probe that fits in a Physical Property Measurement System from Quantum Design.

Figure 2.4 shows the RUS probe for corner-mounting. When the sample is corner-mounted, the restriction of its vibration is reduced to the least. However, small forces exerted on the sample may knock the sample out from between the transducers. Migliori

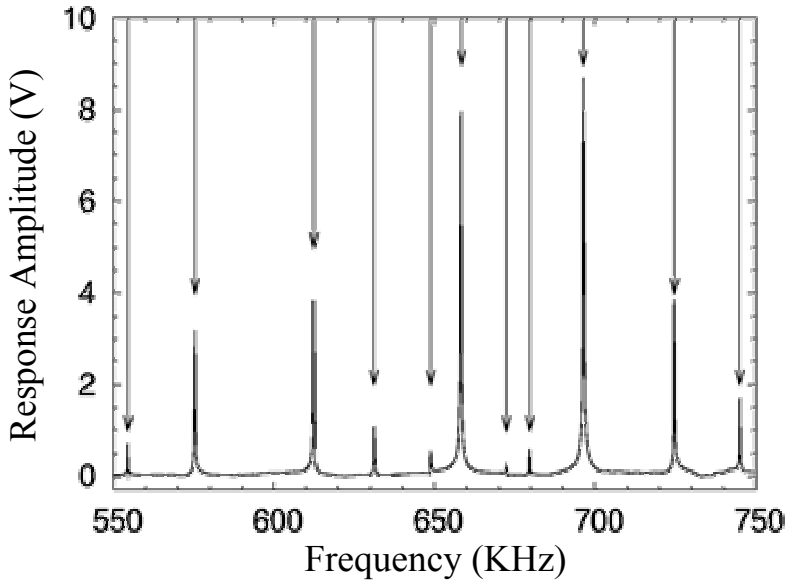

Figure 2.3: a typical RUS scan.

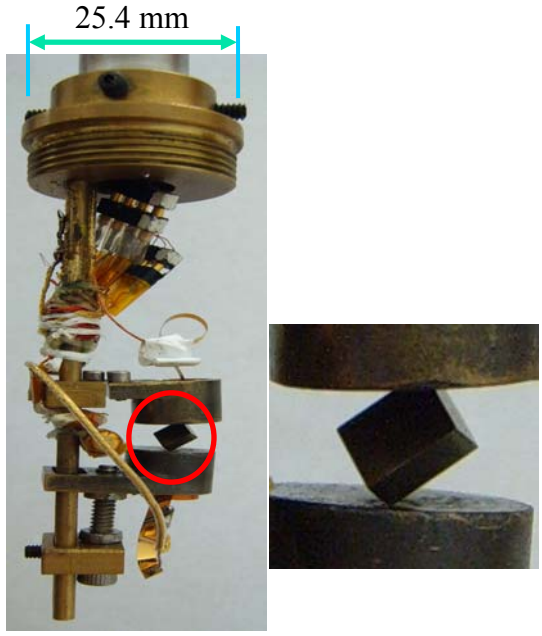

Figure 2.4: RUS probe for corner-mounting.

suggested that these problems can be avoided by flat-mounting the sample. As illustrated (and exaggerated) in Figure 2.5, when the transducers are not entirely parallel, the sample surfaces are not clamped and the sample is still allowed to vibrate freely. The RUS probe for flat-mounting is shown in Figure 2.6. Measurements at higher temperatures (up to 750 K) are performed using the high temperature apparatus developed by Gladden's group at The University of Mississippi, as shown in Figure 2.7. The sample is mounted between two buffer rods. The transducers are placed outside the furnace to maintain their function.

Only two independent elastic constants need to be determined for elastically isotropic materials such as BMGs. In crystalline solids, these two elastic constants would be labeled c_{11} and c_{44}, where the subscripts refer to the crystallographic axes. Since BMGs have no crystallographic reference axes, longitudinal (L) and shear (G) directions are used. The bulk modulus B, Young's modulus E and Poisson ratio ν, can be calculated using the equations below.

$$B = \frac{3L - 4G}{3} \tag{2.16}$$

$$E = \frac{G(3L - 4G)}{L - G} \tag{2.17}$$

$$\nu = \frac{L - 2G}{2(L - G)} = \frac{1}{2} - \frac{1}{2(\frac{B}{G} + \frac{1}{3})} \tag{2.18}$$

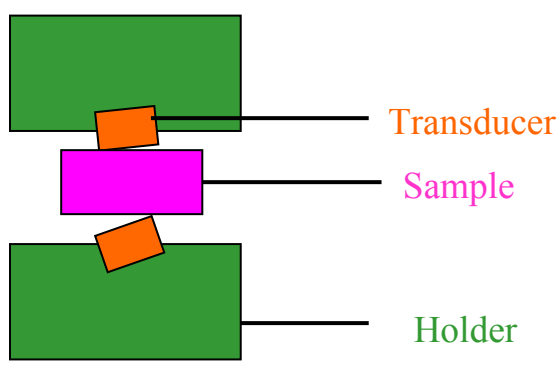

Figure 2.5: Schematic of the sample flat-mounted between the transducers.

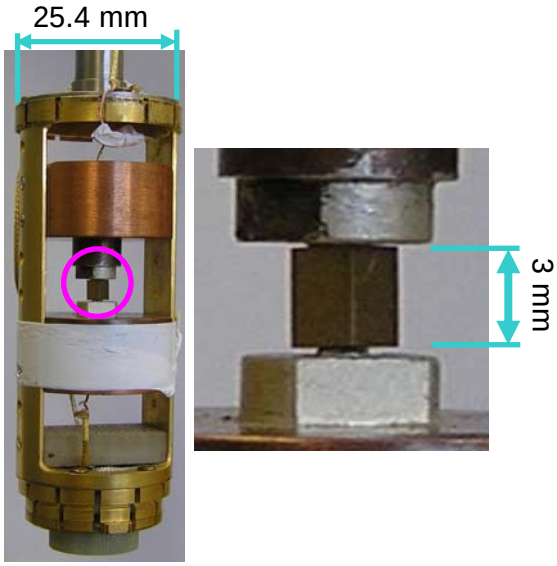

Figure 2.6: RUS probe for flat-mounting.

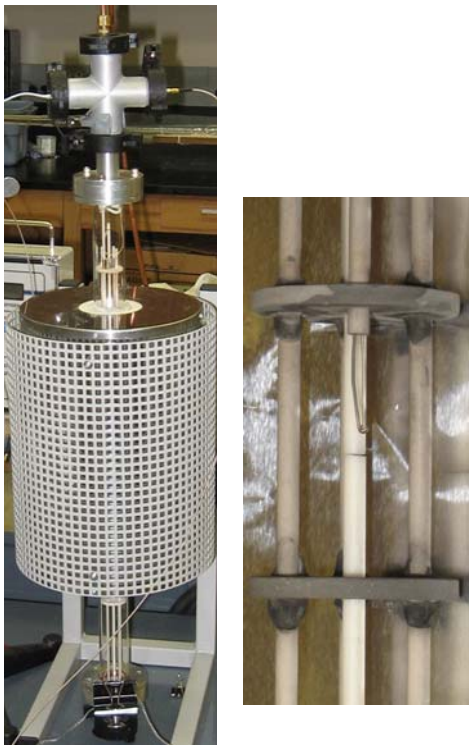

Figure 2.7: High temperature apparatus.

The Debye temperature of the solid θ_D can be obtained from the room temperature elastic moduli, with G and B the shear and bulk modulus at room temperature, M the molecular mass, ρ the physical density, h the Planck constant, k_B the Boltzmann constant, and N_A Avogadro's number (Girifalco, 1973) (Kittel, 1986) (Wang, 1999) (Wang, 2003b).

$$\theta_D = \frac{h}{k_B}\left(\frac{9N_A\rho}{4\pi M}\right)^{1/3}\left[\left(\frac{\rho}{B+4G/3}\right)^{3/2} + 2\left(\frac{\rho}{G}\right)^{3/2}\right]^{-1/3} \tag{2.19}$$

The energy dissipation (or loss) is typically expressed in terms of the quality factor Q of the resonance. It can be determined from the full width at half maximum (FWHM) of the resonant frequencies.

$$Q^{-1} = \frac{\Delta f}{f} \tag{2.20}$$

The heat capacity of BMGs reported in this work has been measured using a Physical Property Measurement System from Quantum Design. BMG samples of mass ~20 mg were mounted on the microcalorimeter platform of size 3x3mm^2 using cryogenic grease (Apiezon N Grease for T < 350 K and Apiezon H Grease for T > 350 K). High vacuum is maintained during heat capacity measurement.

CHAPTER 3

ZIRCONIUM BASED AND COPPER BASED BULK METALLIC GLASSES

Zr-based alloys have received wide interest because of their superior GFA, high strength, and relatively low cost (Yokoyama, 2003) (Inoue, 1990a) (Zhang, 1991) (Peker, 1993). However, the low ductility limits their applications as structural materials. Previously reported measurements of the mechanical properties of Zr-based alloys include tensile and compressive tests at room temperature (Liu, 1998), quasi-static uniaxial compression tests (Gu, 2003), tensile tests (Wang, 2004a), Charpy impact tests (Yokoyama, 2003) (Yokoyama, 2002) as well as fatigue behavior measurements (Wang, 2004a) (Peter, 2002) (Wang, 2004 b). Since Pd has a high Poisson ratio (~0.39), it is expected that by increasing Pd content in $Zr_{50}Cu_{40-x}Al_{10}Pd_x$, BMGs with high Poisson ratio and thus better ductility will be obtained.

Section 3.1 will focus on the elastic properties of several Zr-based BMGs, measured using resonant ultrasound spectroscopy. Our data include measurements on the recently developed $Zr_{63.8}Ni_{16.2}Cu_{15}Al_5$ alloy, which contains two amorphous phases (Du, 2007b). It shows remarkable plasticity, i.e. 30% plastic strain, at room temperature. According to the computational-thermodynamic approach, the compositions of the two liquid phases in the liquid temperature region are $Zr_{68.4}Ni_{23.9}Cu_{6.6}Al_{1.1}$ and $Zr_{61.7}Ni_{12.8}Cu_{18.8}Al_{6.7}$, respectively. As shown in Figure 3.1, scanning electron microscopy (SEM) image and X-ray diffraction (XRD) pattern confirm the glassy nature of the BMG. The transmission electron microscopy (TEM) bright-field image and the selected area-diffraction pattern illustrate the existence of two glassy phases with bright and dark contrasts, respectively. The high resolution electron microscopy (HREM) image of the interface shows that the two glassy phases combine homogeneously.

Cu-based BMGs have attracted intensive interest because of their low cost and good mechanical properties (Inoue, 2001a) (Qiao, 2007) (Duan, 2008) (Fu, 2008) (Lin, 2008).

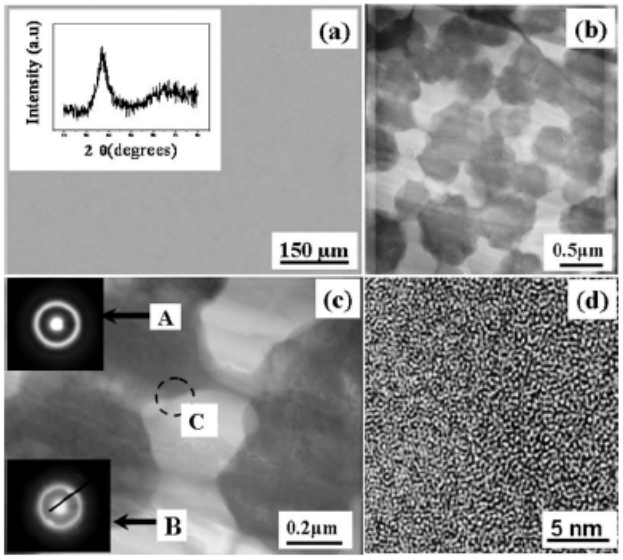

Figure 3.1: Microstructures of $Zr_{63.8}Ni_{16.2}Cu_{15}Al_5$. (a) Scanning electron microscopy image of the etched as-cast microstructure with the inserted X-ray diffraction pattern. (b) and (c) Transmission electron microscopy bright-field image. (d) High resolution electron microscopy image of the interface marked in (c) (Du, 2007b).

Their thermal properties, mechanical properties and corrosion properties have been widely studied. Section 3.2 will concentrate on the elastic properties of Cu-based BMGs.

3.1 Zr-Based BMGs

3.1.1 ZrCuAl and ZrCuAlNi (Ta, Y, Ti) BMGs

Zr-based BMGs, $Zr_{52.5}Cu_{17.9}Ni_{14.6}Al_{10}Ti_5$, $Zr_{50}Cu_{30}Ni_{10}Al_{10}$ and $Zr_{50}Cu_{40}Al_{10}$ were prepared by arc-melting pure elements in argon atmosphere (Yokoyama, 2003) (Yokoyama, 2002) (Gu, 2003). Table 3.1 summarizes the glass transition temperature T_g, crystallization temperature T_x, liquidus temperature T_l determined using differential scanning calorimetry (DSC) and differential thermal analysis (DTA). In addition, Glass Forming Ability (GFA) parameters, including the supercooled liquid region ΔT_x, reduced glass transition temperature T_{rg}, Hruby factor K_{gl}, γ and γ_m of Zr-based BMGs are also shown in Table 3.1.

Table 3.1: Glass transition temperature T_g, crystallization temperature T_x, liquidus temperature T_l, supercooled liquid region ΔT_x, reduced glass transition temperature T_{rg}, Hruby factor K_{gl}, γ and γ_m of Zr-based BMGs.

Composition	T_g (K)	T_x (K)	T_l (K)	ΔT_x (K)	T_{rg}	K_{gl}	γ	γ_m
$Zr_{50}Cu_{30}Ni_{10}Al_{10}$	708	779	1100	71	0.644	0.221	0.431	0.773
$Zr_{50}Cu_{40}Al_{10}$	706	792	1092	86	0.647	0.287	0.440	0.804
$Zr_{52.5}Cu_{17.9}Ni_{14.6}Al_{10}Ti_5$	686	740	1076	54	0.638	0.161	0.420	0.738
$Zr_{54.45}Cu_{29.7}Al_{9.9}Ni_{4.95}Y_1$	671	747		76				
$Zr_{63.8}Ni_{16.2}Cu_{15}Al_5$	647	745	1178	98	0.549	0.226	0.408	0.716
$Zr_{50}Cu_{37}Al_{10}Pd_3$	705	795	1090	90	0.647	0.305	0.443	0.812
$Zr_{50}Cu_{35}Al_{10}Pd_5$	718	793	1098	75	0.654	0.246	0.437	0.791
$Zr_{50}Cu_{33}Al_{10}Pd_7$	715	792	1110	77	0.644	0.242	0.434	0.783

Figure 3.2 (a) shows the temperature-dependence of the shear modulus G for two different samples of the Zr-based alloy $Zr_{50}Cu_{30}Ni_{10}Al_{10}$, and illustrates how the modulus increases with decreasing temperature. The small difference between both samples is most likely due to a minor difference in density, the sample with the higher density (6.88 g/cm^3) having a slightly higher modulus compared to the sample with the lower density (6.86 g/cm^3). The temperature-dependence of the shear modulus can be modeled quite well using the so-called Varshni function, with T the temperature, c_{ij}^0 the elastic constant at 0 K, and s and t fitting parameters (Varshni 1970).

$$c_{ij}(T) = c_{ij}^0 - s/(e^{t/T} - 1) \tag{3.1}$$

This function was shown by Varshni to describe the temperature-dependence of the elastic constants of many simple substances and characterizes to some extent "normal" elastic behavior. A similar temperature-dependence is observed in $Zr_{52.5}Cu_{17.9}Ni_{14.6}Al_{10}Ti_5$ and $Zr_{50}Cu_{40}Al_{10}$ BMGs, illustrated in Figure 3.2 (b). The figure clearly illustrates how all three alloys follow the "normal" Varshni-behavior, and at the same time shows how the elastic moduli of the alloys reflect changes in composition: the

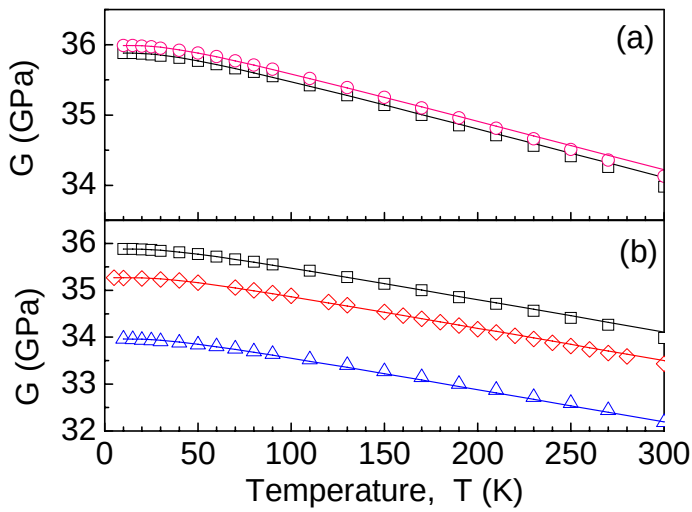

Figure 3.2: Shear modulus G as a function of temperature. (a) For two samples of $Zr_{50}Cu_{30}Ni_{10}Al_{10;}$ (b) For $Zr_{50}Cu_{30}Ni_{10}Al_{10}$ (□), $Zr_{50}Cu_{40}Al_{10}$ (◇), and $Zr_{52.5}Cu_{17.9}Ni_{14.6}Al_{10}Ti_5$ (△). The solid lines represent a fit using the Varshni model, with parameters s= 0.7 GPa and t = 100 K. c^0=36.0 GPa and 35.9 GPa for $Zr_{50}Cu_{30}Ni_{10}Al_{10}$, c^0=35.7 GPa for $Zr_{50}Cu_{40}Al_{10}$, and c^0=34.0 GPa for $Zr_{52.5}Cu_{17.9}Ni_{14.6}Al_{10}Ti_5$.

shear modulus of $Zr_{50}Cu_{30}Ni_{10}Al_{10}$ is the highest over the temperature range from 5 to 300 K, followed by that of $Zr_{50}Cu_{40}Al_{10}$. The shear modulus of $Zr_{52.5}Cu_{17.9}Ni_{14.6}Al_{10}Ti_5$ is the lowest.

Room temperature longitudinal modulus L, bulk modulus B, Young's modulus E and Poisson ratio ν are summarized in Table 3.2. Young's moduli are in good agreement with the results obtained from tensile and compression tests at room temperature for alloys with comparable composition, i.e. i.e. 86 GPa for $Zr_{52.5}Cu_{17.9}Ni_{14.6}Al_{10}Ti_5$ (Gu, 2003), 93 GPa for $Zr_{50}Cu_{43}Ni_{10}Al_{10}$ (Wang, 2004a) and 89 GPa for $Zr_{50}Cu_{40}Al_{10}$ (Wang, 2004a). In addition, the elastic constants of our Zr-based BMGs follow the trend of previously reported data for Zr-based alloys with slightly different compositions (Wang, 2004c) (Wang, 2006). $Zr_{52.5}Cu_{17.9}Ni_{14.6}Al_{10}Ti_5$ has high Poisson ratio, reaching 0.374 at room temperature.

Figure 3.3 shows the temperature dependence of the longitudinal modulus L, the bulk

Table 3.2: Room temperature elastic constants for various Zr-based BMGs.

Composition	*G* (GPa)	*L* (GPa)	*B* (GPa)	*E* (GPa)	*B/G*	ν
$Zr_{50}Cu_{30}Ni_{10}Al_{10}$	34.0	165.3	120.0	93.2	3.53	0.371
$Zr_{50}Cu_{40}Al_{10}$	33.4	157.5	112.9	91.3	3.38	0.365
$Zr_{52.5}Cu_{17.9}Ni_{14.6}Al_{10}Ti_5$	32.2	159.7	116.8	88.4	3.63	0.374
$Zr_{54.45}Cu_{29.7}Al_{9.9}Ni_{4.95}Y_1$	31.1	151.8	110.4	85.2	3.55	0.371
$Zr_{59}Cu_{18}Al_{10}Ni_8Ta_5$	30.9	143.3	102.1	84.3	3.30	0.362
$Zr_{60}Cu_{30}Al_{10}$	29.7	146.6	107.0	81.5	3.61	0.373
$Zr_{63.8}Ni_{16.2}Cu_{15}Al_5$	27.5	147.7	111.1	76.2	4.04	0.386
$Zr_{65}Cu_{17.5}Ni_{10}Al_{7.5}$	27.5	143.6	107.0	75.9	3.89	0.382
[a]$Zr_{65}Cu_{15}Ni_{10}Al_{10}$	31.0	148.0	106.7	83.0	3.52	0.367
[a]$Zr_{57}Nb_5Cu_{15.4}Ni_{12.6}Al_{10}$	32.0	150.4	107.7	87.3	3.37	0.365
[a]$Zr_{53}Ti_5Cu_{20}Ni_{12}Al_{10}$	32.1	149.6	106.8	87.6	3.32	0.363
[a]$Zr_{48}Nb_8Cu_{12}Be_{24}Fe_8$	35.2	160.3	113.4	95.7	3.22	0.359

[a] Data from (Wang, 2006).

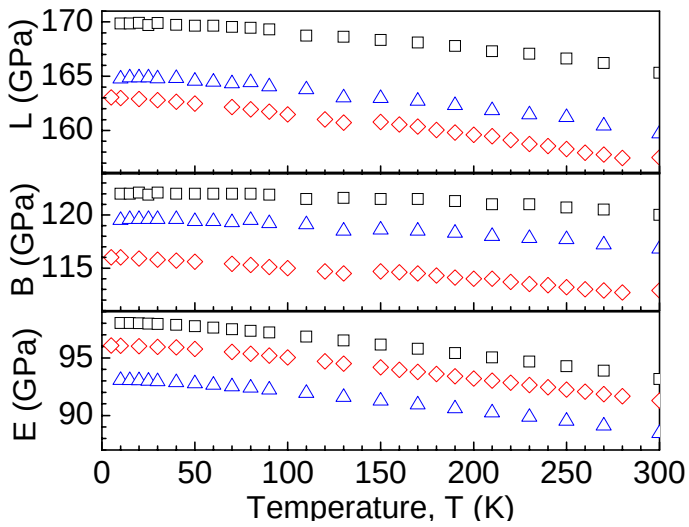

Figure 3.3: Longitudinal modulus *L*, bulk modulus *B* and Young's modulus *E* as a function of temperature for $Zr_{50}Cu_{30}Ni_{10}Al_{10}$ (□), $Zr_{50}Cu_{40}Al_{10}$ (◇), and $Zr_{52.5}Cu_{17.9}Ni_{14.6}Al_{10}Ti_5$ (△).

modulus B and Young's modulus E between 5 K and 300 K. The moduli decrease with increasing temperature. Figure 3.4 shows the temperature dependence of the Poisson ratio ν as well as the ratio of bulk modulus to shear modulus B/G. With increasing temperature, ν and B/G increase. The high Poisson ratios (and B/G values) correlate with the enhanced ductility observed in these alloys (Yokoyama, 2003) (Yokoyama, 2002), confirming the suggested link between the elastic moduli and the ductility of the alloys.

Zr-based BMGs, $Zr_{54.45}Cu_{29.7}Al_{9.9}Ni_{4.95}Y_1$, $Zr_{59}Cu_{18}Al_{10}Ni_8Ta_5$, $Zr_{60}Cu_{30}Al_{10}$, $Zr_{63.8}Ni_{16.2}Cu_{15}Al_5$ and $Zr_{65}Cu_{17.5}Ni_{10}Al_{7.5}$ were prepared by arc-melting pure elements in argon atmosphere and in situ suction casting in a copper mold (Okai, 2007) (Yokoyama, 2007) (Du, 2007b) (Okuda, 2006). The characteristic temperatures, T_g, T_x and T_l, and the GFA parameters are given in Table 3.1. Room temperature elastic constants are shown in Table 3.2. Our RUS measurements reveal that the two-glassy-phase BMG $Zr_{63.8}Ni_{16.2}Cu_{15}Al_5$ is elastically homogeneous. The striking high Poisson ratio ~0.39 at room temperature agrees with the excellent ductility found in this BMG. The high ductility is attributed to the chemical inhomogeneity on the micron scale, i.e. hard phases surrounded by soft phases, leading to extensive shear-band formation, interactions and multiplication (Du, 2007b). Figure 3.5 shows the temperature dependence of the longitudinal modulus L and the bulk modulus B for $Zr_{59}Cu_{18}Al_{10}Ni_8Ta_5$, $Zr_{60}Cu_{30}Al_{10}$, $Zr_{63.8}Ni_{16.2}Cu_{15}Al_5$ and $Zr_{65}Cu_{17.5}Ni_{10}Al_{7.5}$ between 5 K and 300 K. The temperature dependences of the shear modulus G, Young's modulus E , the ratio of bulk modulus to shear modulus B/G and Poisson ratio ν are shown in Figure 3.6 and Figure 3.7. They all show "normal" elastic behavior, i.e. L, B, G and E decrease with increasing temperature, and B/G and ν increase with increasing temperature.

3.1.2 ZrCuAlPd BMGs

$Zr_{50}Cu_{40-x}Al_{10}Pd_x$ (x=0, 1, 2, 3, 5, 6, 7, 9, 12 and 15 at.%) BMGs were prepared by high-pressure die-casting of the melt into cylindrical copper molds (Yokoyama, 2002) (Maeda, 2007) (Wang, 2007). For $Zr_{50}Cu_{40-x}Al_{10}Pd_x$ (x=0, 3, 6, 9, 12 and 15 at.%) BMGs, rods with casting diameters of 4 mm, 6 mm and 8 mm were prepared, in order to investigate

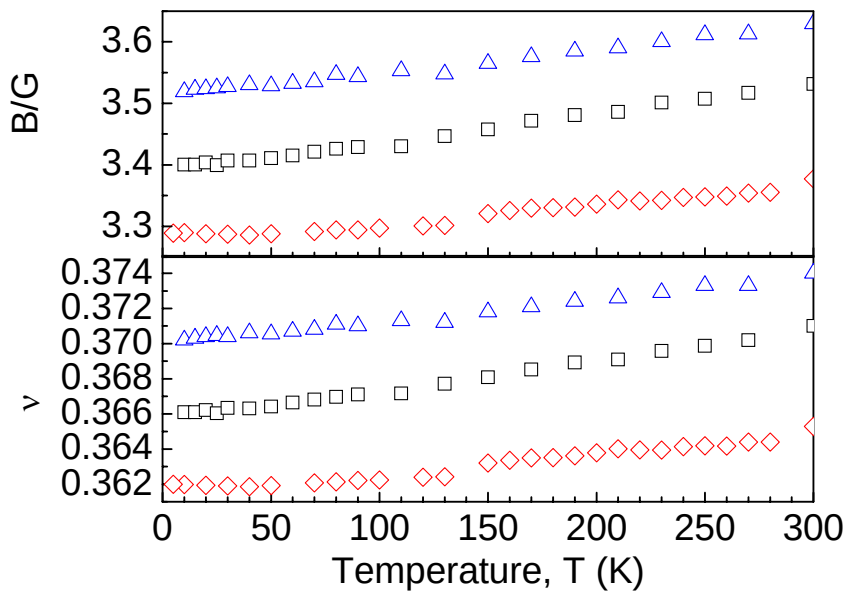

Figure 3.4: The ratio of bulk modulus to shear modulus *B/G* and the Poisson ratio ν as a function of temperature for $Zr_{50}Cu_{30}Ni_{10}Al_{10}$ (□), $Zr_{50}Cu_{40}Al_{10}$ (◇), and $Zr_{52.5}Cu_{17.9}Ni_{14.6}Al_{10}Ti_5$ (△).

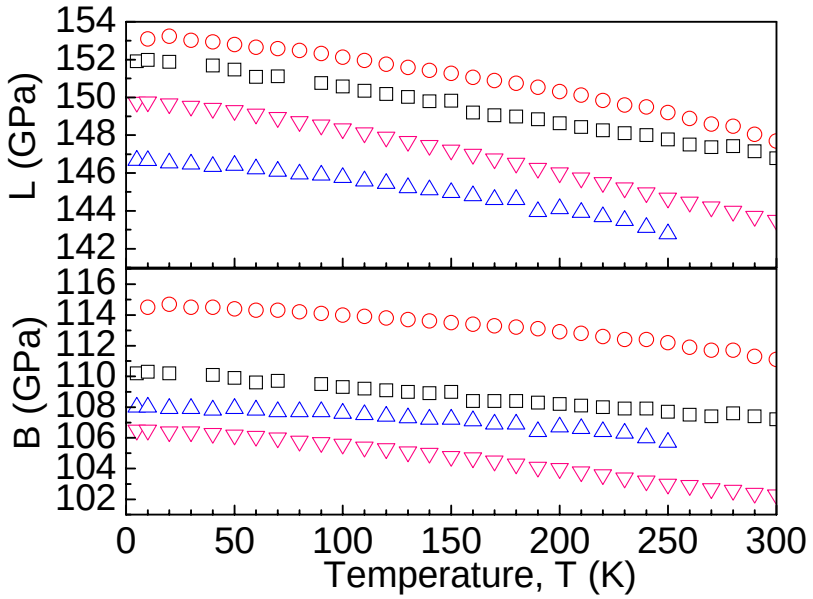

Figure 3.5: Longitudinal modulus *L* and bulk modulus *B* as a function of temperature for $Zr_{59}Cu_{18}Al_{10}Ni_8Ta_5$ (▽), $Zr_{60}Cu_{30}Al_{10}$ (□), $Zr_{63.8}Ni_{16.2}Cu_{15}Al_5$ (O), $Zr_{65}Cu_{17.5}Ni_{10}Al_{7.5}$ (△).

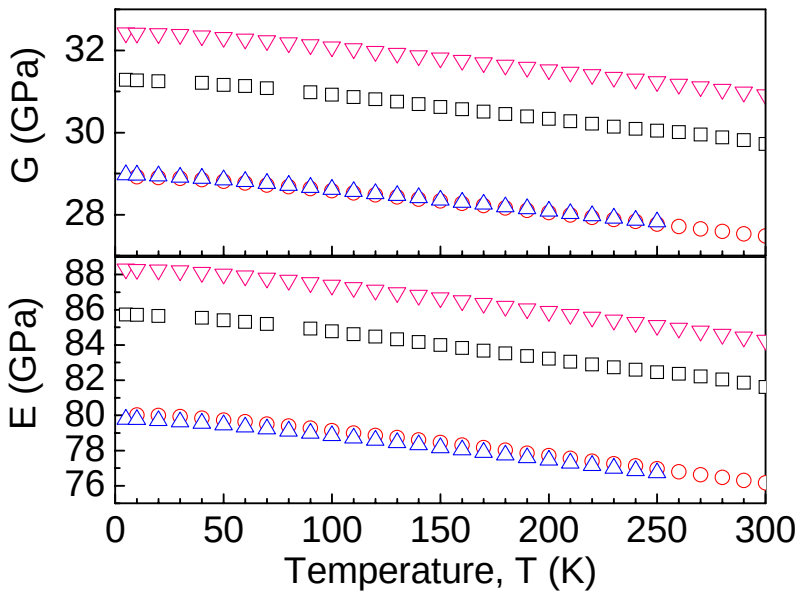

Figure 3.6: Shear modulus *G* and Young's modulus *E* as a function of temperature for $Zr_{59}Cu_{18}Al_{10}Ni_8Ta_5$ (▽), $Zr_{60}Cu_{30}Al_{10}$ (□), $Zr_{63.8}Ni_{16.2}Cu_{15}Al_5$ (O) and $Zr_{65}Cu_{17.5}Ni_{10}Al_{7.5}$ (△).

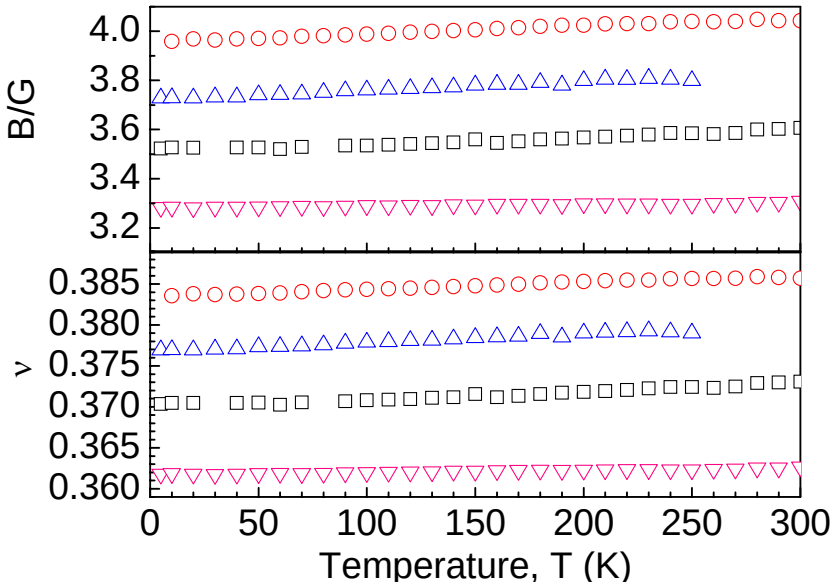

Figure 3.7: Ratio of bulk modulus to shear modulus *B/G* and Poisson ratio ν as a function of temperature for $Zr_{59}Cu_{18}Al_{10}Ni_8Ta_5$ (▽), $Zr_{60}Cu_{30}Al_{10}$ (□), $Zr_{63.8}Ni_{16.2}Cu_{15}Al_5$ (O) and $Zr_{65}Cu_{17.5}Ni_{10}Al_{7.5}$ (△).

the effect of casting diameter.

Figure 3.8 shows the longitudinal modulus L, shear modulus G and Poisson ratio ν for $Zr_{50}Cu_{40-x}Al_{10}Pd_x$ (x=0, 3, 6, 9, 12 and 15 at.%) at room temperature. The bulk modulus B and Young's modulus E are shown in Figure 3.9. The elastic moduli are plotted versus the casting diameter of the rods, illustrating that the effects of casting diameter are minor. With decreasing casting diameter, the Poisson ratio slightly increases, the shear modulus and Young's modulus slightly decrease, and the longitudinal modulus and the bulk modulus generally remain the same.

Since the changes in elastic moduli with diameter are less than 1 %, the discussion of the data for various Pd content uses moduli that are averaged over the different casting diameter. These averaged moduli for $Zr_{50}Cu_{40-x}Al_{10}Pd_x$ (x=0, 1, 2, 3, 5, 6, 7, 9, 12 and 15 at.%) are listed in Table 3.3, together with the density ρ and Debye temperature θ_D obtained for these materials. Figure 3.10 and Figure 3.11 show the room-temperature dependence of the longitudinal modulus, bulk modulus, Poisson ratio, shear modulus and Young's modulus on Pd content. With increasing Pd content (or decreasing Cu content), the longitudinal modulus, bulk modulus and Poisson ratio increase gradually. This is in agreement with what is expected since Pd has a larger longitudinal modulus, shear modulus and Poisson ratio than Cu, as shown in Table 3.4 (http://www.webelements.com/webelements/elements/). On the other hand, with increasing Pd content (or decreasing Cu content), the shear modulus and Young's modulus gradually increase, reach a maximum at 12 at.% Pd and then decrease.

The temperature dependence of longitudinal modulus L, shear modulus G, bulk modulus B, Young's modulus E and Poisson ratio ν for $Zr_{50}Cu_{40-x}Al_{10}Pd_x$ BMGs with x=0, 2, 5, 6, 7, 9, 12 and 15 at.% between 5 K and 400 K are shown in Figures 3.12-3.16. With increasing temperature, L, G, B and E decrease, and ν increases.

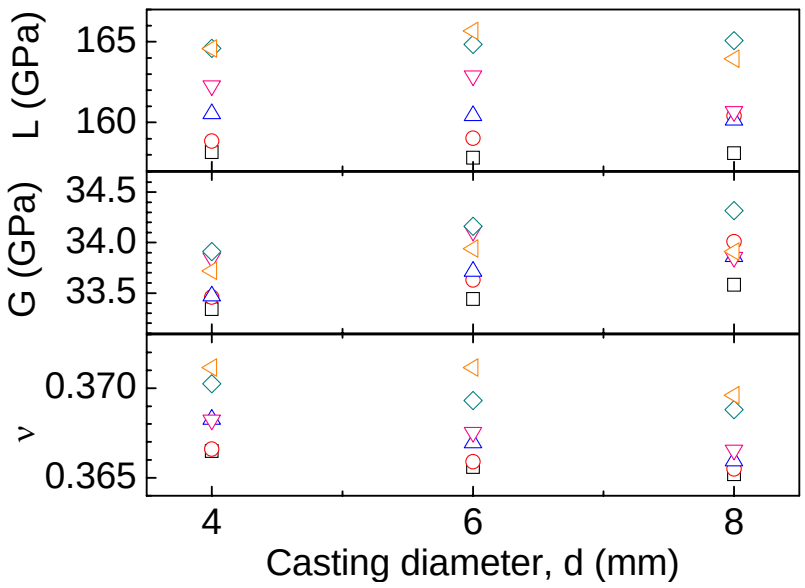

Figure 3.8: Dependence of longitudinal modulus *L*, shear modulus *G* and Poisson ratio ν on the casting diameter of the samples for $Zr_{50}Cu_{40-x}Al_{10}Pd_x$ (x=0, 3, 6, 9, 12 and 15 at.%) alloys. Pd: 0 at.% (□), 3 at.% (O), 6 at.% (△), 9 at.% (▽), 12 at.% (◇) and 15 at.% (◁).

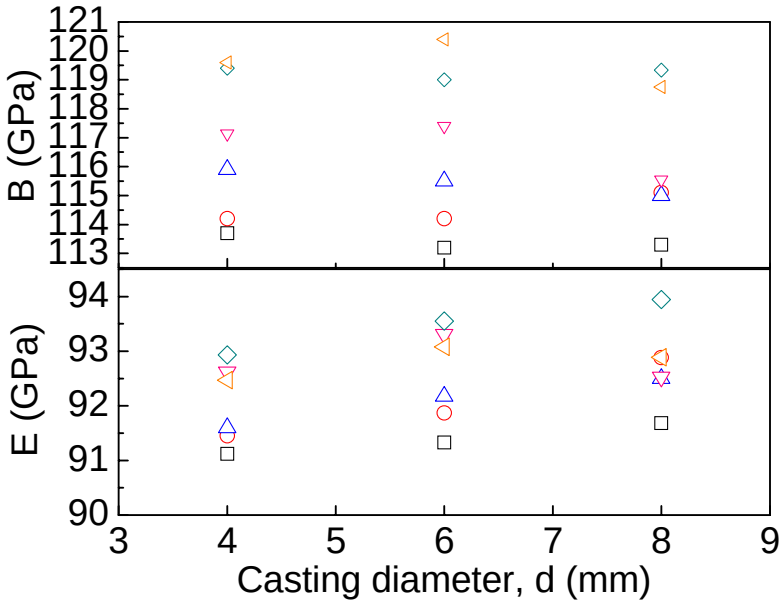

Figure 3.9: Dependence of bulk modulus *B* and Young's modulus *E* on the casting diameter of the samples for $Zr_{50}Cu_{40-x}Al_{10}Pd_x$ (x=0, 3, 6, 9, 12 and 15 at.%) alloys. Pd: 0 at.% (□), 3 at.% (O), 6 at.% (△), 9 at.% (▽), 12 at.% (◇) and 15 at.% (◁).

Table 3.3: Density ρ, shear modulus G, longitudinal modulus L, bulk modulus B, Young's modulus E, Poisson ratio ν and Debye temperature θ_D of $Zr_{50}Cu_{40-x}Al_{10}Pd_x$ (x=0, 1, 2, 3, 5, 6, 7, 9, 12 and 15 at.%) alloys.

Composition	ρ (g/cm^3)	G (GPa)	L (GPa)	B (GPa)	E (GPa)	ν	θ_D (K)
$Zr_{50}Cu_{40}Al_{10}$	6.808	33.49	159.07	114.4	91.54	0.3666	282.81
$Zr_{50}Cu_{39}Al_{10}Pd_1$	6.851	33.74	157.62	112.7	92.02	0.3639	282.91
$Zr_{50}Cu_{38}Al_{10}Pd_2$	6.868	33.84	158.95	113.8	92.37	0.3648	282.71
$Zr_{50}Cu_{37}Al_{10}Pd_3$	6.885	33.72	159.90	114.9	92.16	0.3664	281.61
$Zr_{50}Cu_{35}Al_{10}Pd_5$	6.932	33.93	159.87	114.6	92.65	0.3653	281.06
$Zr_{50}Cu_{34}Al_{10}Pd_6$	6.979	33.92	160.54	115.3	92.67	0.3661	280.20
$Zr_{50}Cu_{33}Al_{10}Pd_7$	7.008	34.09	161.79	116.4	93.16	0.3666	280.21
$Zr_{50}Cu_{31}Al_{10}Pd_9$	7.030	33.99	162.83	117.5	93.01	0.3681	278.67
$Zr_{50}Cu_{28}Al_{10}Pd_{12}$	7.141	34.15	164.88	119.4	93.54	0.3694	277.13
$Zr_{50}Cu_{25}Al_{10}Pd_{15}$	7.191	33.86	165.28	120.1	92.85	0.3712	274.21

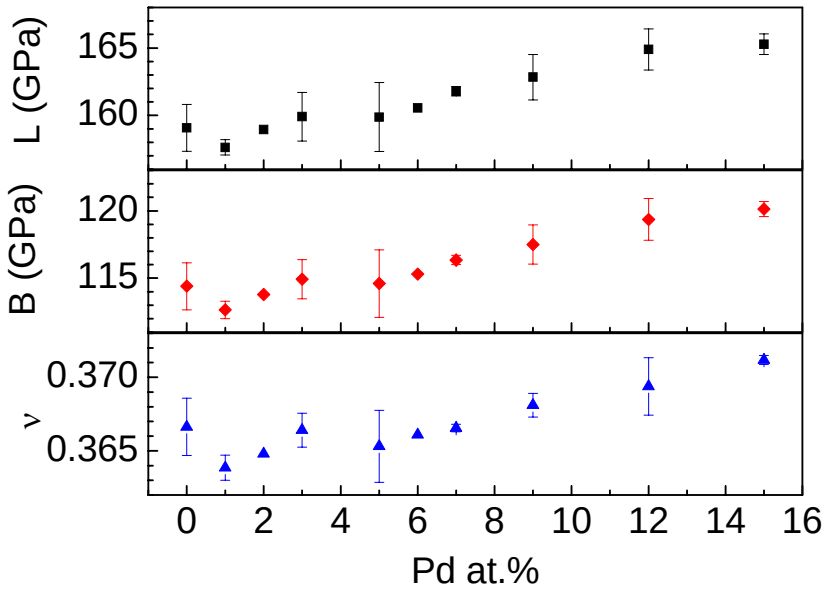

Figure 3.10: Dependence of longitudinal modulus L, bulk modulus B and Poisson ratio ν on the Pd content for $Zr_{50}Cu_{40-x}Al_{10}Pd_x$ alloys.

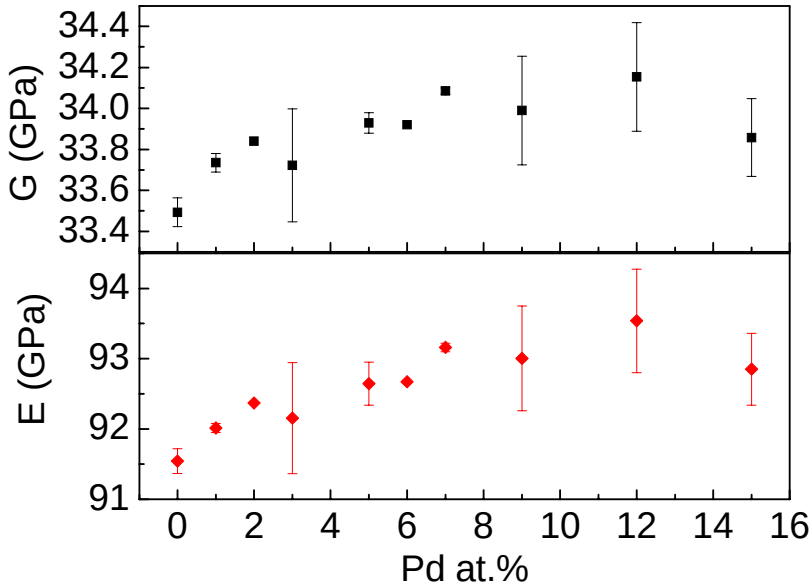

Figure 3.11: Dependence of shear modulus *G* and Young's modulus *E* on the Pd content for $Zr_{50}Cu_{40-x}Al_{10}Pd_x$ alloys.

Table 3.4: Density and elastic moduli of the elements Zr, Cu, Al and Pd (http://www.webelements.com/webelements/elements/).

Element	ρ (g/cm^3)	*G* (GPa)	*L* (GPa)	*B* (GPa)	*E* (GPa)	ν
Zr	6.511	33	136	92	68	0.34
Cu	8.920	48	204	140	130	0.34
Al	2.700	26	111	76	70	0.35
Pd	12.023	44	239	180	121	0.39

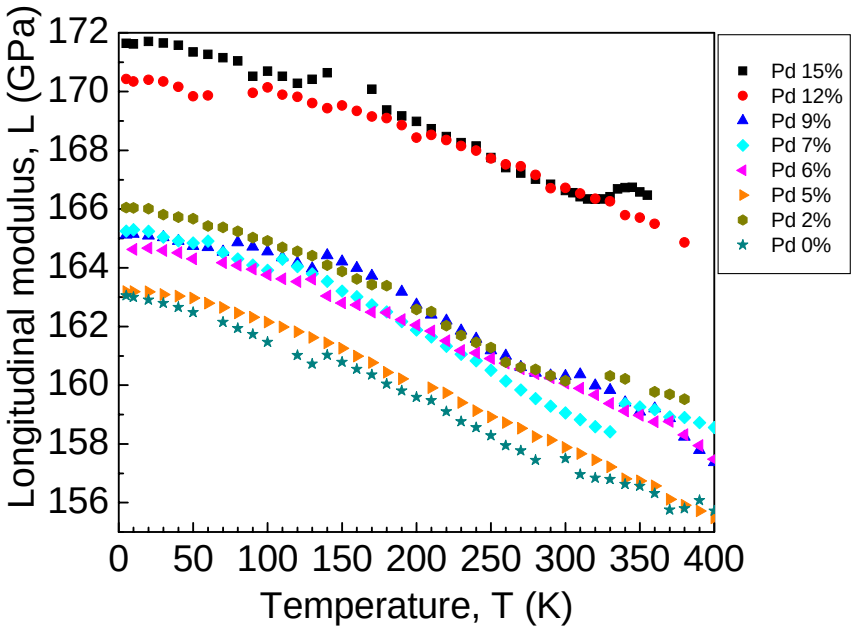

Figure 3.12: Longitudinal modulus *L* as a function of temperature for $Zr_{50}Cu_{40-x}Al_{10}Pd_x$ BMGs.

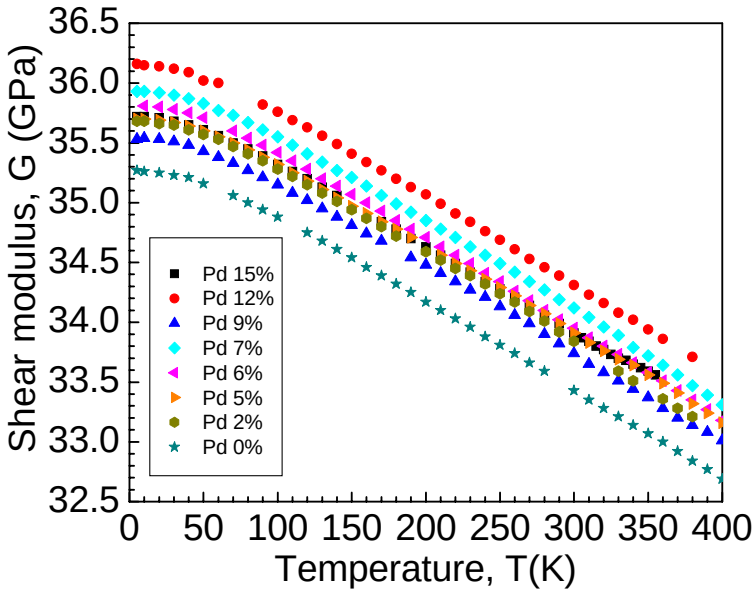

Figure 3.13: Shear modulus *G* as a function of temperature for $Zr_{50}Cu_{40-x}Al_{10}Pd_x$ BMGs.

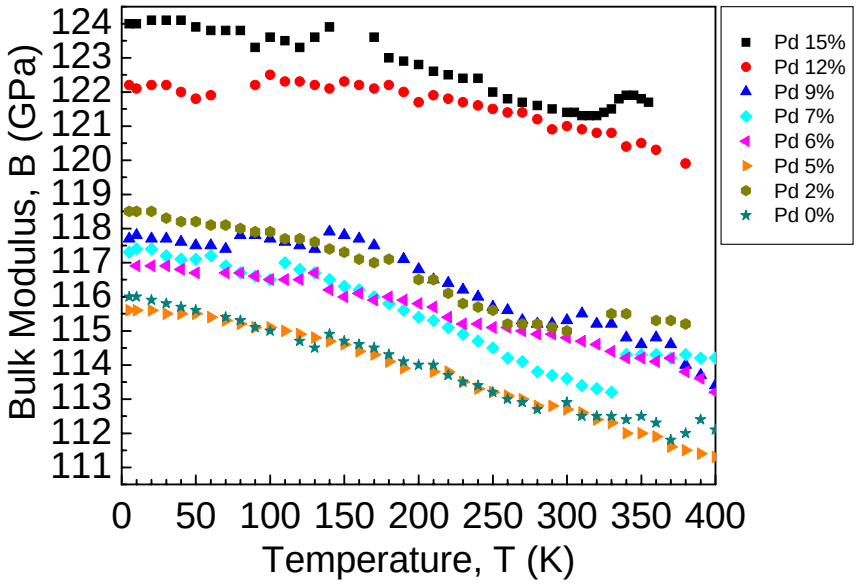

Figure 3.14: Bulk modulus *B* as a function of temperature for $Zr_{50}Cu_{40-x}Al_{10}Pd_x$ BMGs.

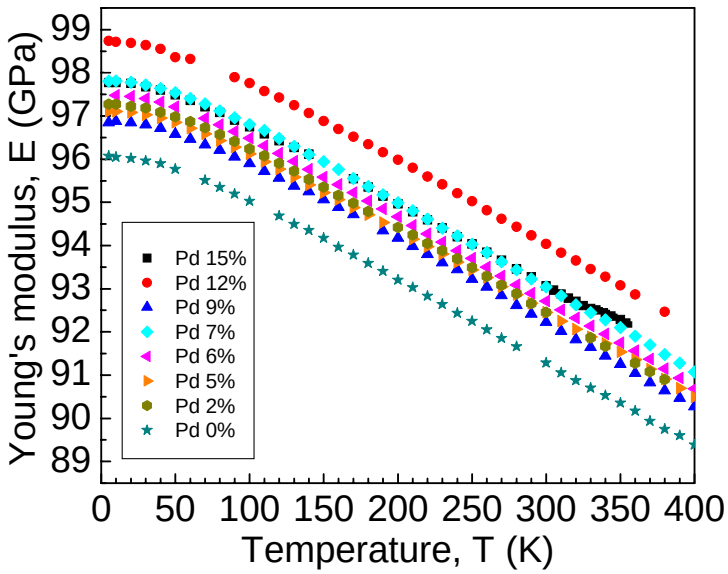

Figure 3.15: Young's modulus *E* as a function of temperature for $Zr_{50}Cu_{40-x}Al_{10}Pd_x$ BMGs.

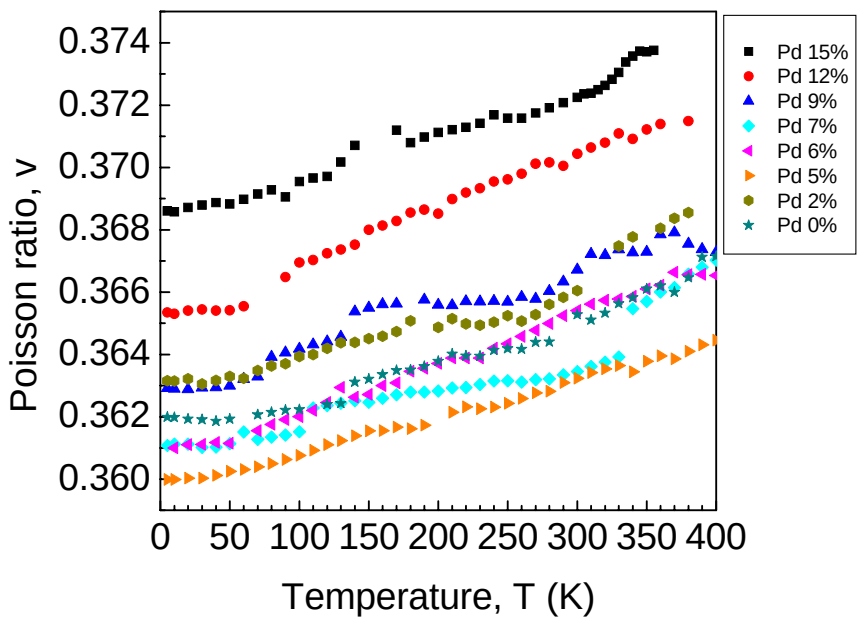

Figure 3.16: Poisson ratio ν as a function of temperature for $Zr_{50}Cu_{40-x}Al_{10}Pd_x$ BMGs.

The internal friction Q^{-1} is shown in Figure 3.17 as a function of temperature for $Zr_{50}Cu_{40-x}Al_{10}Pd_x$ BMGs with x=0, 2, 3, 6, 12 and 15 at.%. The internal friction refers to the energy dissipation (or loss). It provides valuable information about atomic displacement and has been widely studied for various bulk metallic glasses (Ichitsubo, 2003) (Hiki, 2003) (Hiki, 2008) (Yang, 2007) (Fukuhara, 2007) (Fukuhara, 2008). Figure 3.17 shows that, below 300 K, the internal friction increases slowly with increasing temperature. Above 300 K, the internal friction increases more rapidly. The increase in the internal friction is attributed to the atomic motion during relaxation, which is also known to cause a peak in Q^{-1}, as is observed in the internal friction of $Zr_{50}Cu_{38}Al_{10}Pd_2$ around 250 K. Similar results have been reported for $Zr_{45}Cu_{45}Al_5Ag_5$ (Fukuhara, 2008).

The elastic constants of $Zr_{50}Cu_{25}Al_{10}Pd_{15}$ were measured up to 730 K, above the glass transition temperature ($T_g \approx 720$ K). The temperature dependence of the shear modulus G, Young's modulus E and Poisson ratio ν are shown in Figure 3.18. The temperature dependence of the longitudinal modulus L and the bulk modulus B are shown in Figure 3.19. With increasing temperature, all moduli gradually decrease up to about 500 K. Above 500 K, a dramatic decrease in B and L is observed. G and E show an almost

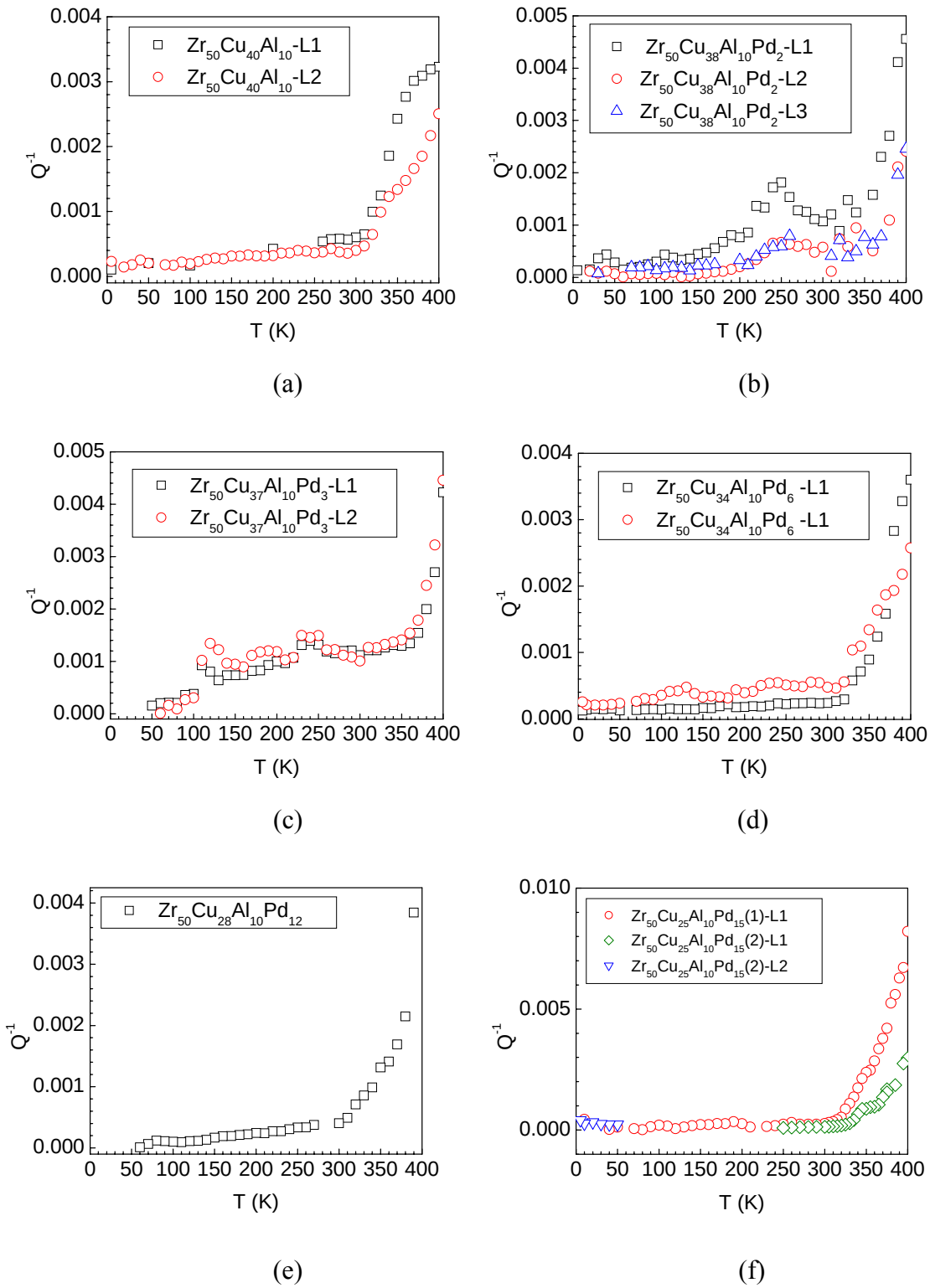

Figure 3.17: Temperature dependence of internal friction Q^{-1} for $Zr_{50}Cu_{40-x}Al_{10}Pd_x$ BMGs.

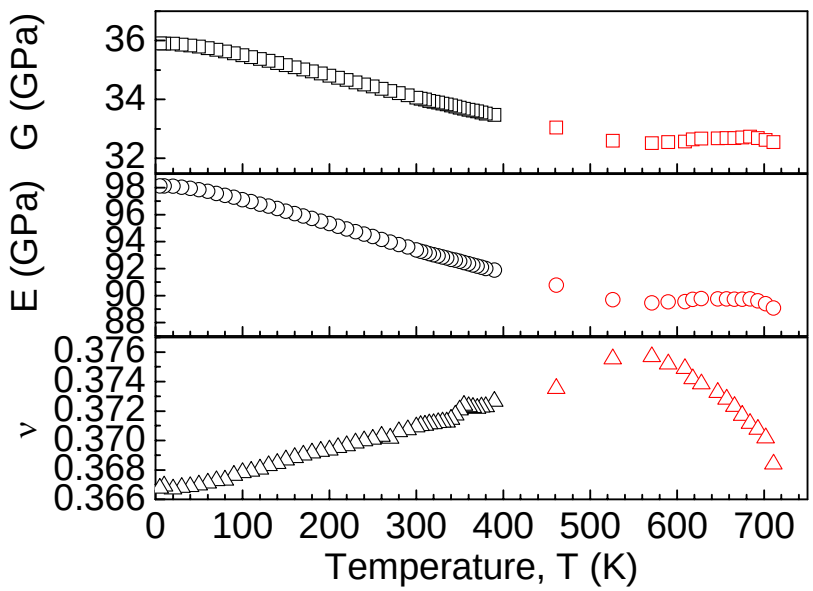

Figure 3.18: Temperature dependence of shear modulus *G*, Young's modulus *E* and Poisson ratio ν of $Zr_{50}Cu_{25}Al_{10}Pd_{15}$ up to the glass transition temperature.

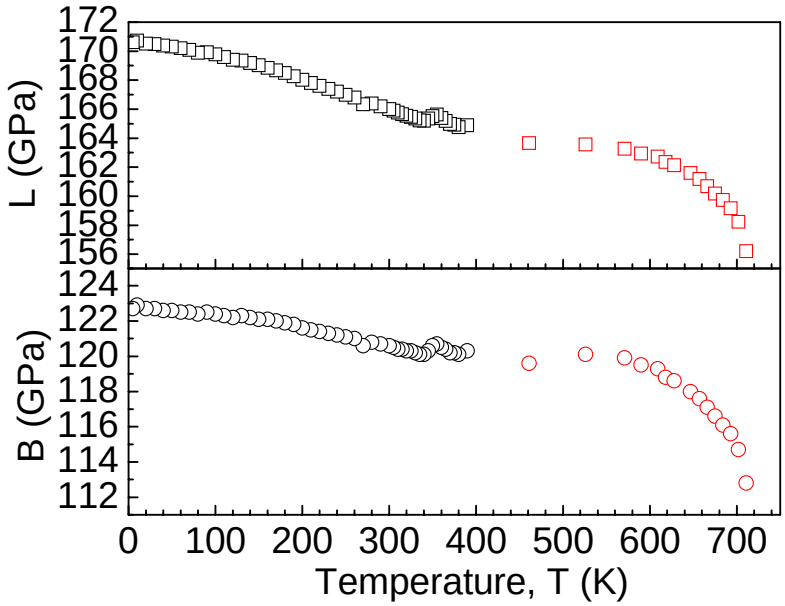

Figure 3.19: Temperature dependence of longitudinal modulus *L* and bulk modulus *B* of $Zr_{50}Cu_{25}Al_{10}Pd_{15}$ up to the glass transition temperature.

temperature-independent behavior between 500 K and 600 K. With increasing temperature, ν increases first, but starts decreasing above 550 K. These changes in elastic constants are believed to be related to the crystallization. Using high energy Synchrotron X-ray diffraction, Jiang et al. have examined the as-cast sample, which was only measured at 300 K using RUS, and the heated sample, which was measured up to 730 K using RUS (Jiang, unpublished). The indicators of crystallization have been observed in the heated sample, according to the diffraction images and peaks shown in Figure 3.20 and Figure 3.21, respectively.

3.2 Cu-Based BMGs

Recently Cu-based BMGs have attracted intensive interest because of their low cost and good mechanical properties. Cu-based BMGs, $Cu_{53.9}Zr_{39.2}Al_{4.9}Er_2$, $Cu_{47.5}Zr_{47.5}Al_5$, $Cu_{47.5}Zr_{38}Hf_{9.5}Al_5$, $Cu_{47}Zr_{47}Al_6$, $Cu_{46.25}Zr_{46.25}Al_{7.5}$, $Cu_{46.25}Zr_{45.25}Al_{7.5}Sn_1$, and $Cu_{42.5}Ti_{41.5}Ni_{7.5}Hf_5Zr_{2.5}Si_1$ were prepared by arc-melting the pure elements in argon atmosphere and then casting into a copper mold (Qiao, 2007). The glass transition temperature T_g, crystallization temperature T_x, liquidus temperature T_l, and the glass forming ability parameters are listed in Table 3.5. The density and room temperature elastic constants are listed in Table 3.6. The elastic constants of Cu-based BMGs are also sensitive to the composition of BMGs. The Poisson ratio of $Cu_{47.5}Zr_{47.5}Al_5$ reaches 0.374, indicating good ductility. Generally, the elastic constants of Cu-based BMGs are close to those of Zr-based BMGs.

The longitudinal modulus L, shear modulus G, bulk modulus B, Young's modulus E and Poisson ratio ν as a function of temperature for $Cu_{53.9}Zr_{39.2}Al_{4.9}Er_2$, $Cu_{47.5}Zr_{47.5}Al_5$, $Cu_{47.5}Zr_{38}Hf_{9.5}Al_5$ and $Cu_{47}Zr_{47}Al_6$ are shown in Figures 3.22-3.26, respectively. From 5 K to 350 K, the elastic constants show "normal" behavior, i.e. with increasing temperature L, G, E and B decrease and ν increases.

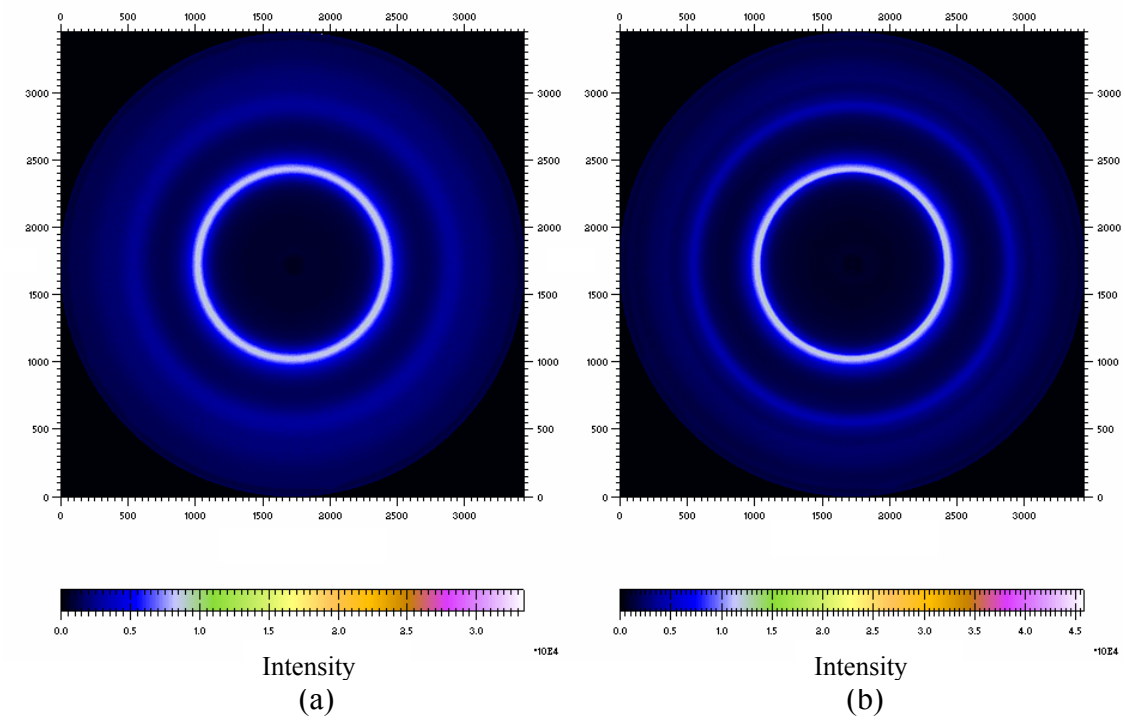

Figure 3.20: Diffraction image of $Zr_{50}Cu_{25}Al_{10}Pd_{15}$ using high energy Synchrotron X-ray diffraction. (a) as-cast sample (300 K). (b) heated sample (730 K) using the wavelength λ=0.0107480 nm. (Jiang, unpublished).

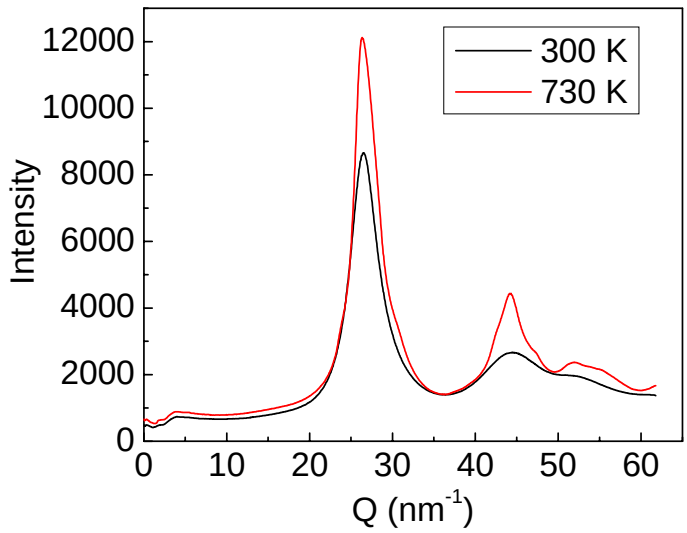

Figure 3.21: High energy Synchrotron X-ray diffraction of $Zr_{50}Cu_{25}Al_{10}Pd_{15}$ as-cast sample (300K) and heated sample (730 K) using the wavelength λ=0.0107480 nm. (Jiang, unpublished).

Table 3.5: Glass transition temperature T_g, crystallization temperature T_x, liquidus temperature T_l, supercooled liquid region ΔT_x, reduced glass transition temperature T_{rg}, Hruby factor K_{gl}, γ and γ_m of Cu-based BMGs.

Composition	T_g (K)	T_x (K)	T_l (K)	ΔT_x (K)	T_{rg}	K_{gl}	γ	γ_m
$Cu_{47.5}Zr_{47.5}Al_5$	695	756	1189	61	0.585	0.141	0.401	0.687
$Cu_{47.5}Zr_{38}Hf_{9.5}Al_5$	705	767	1189	62	0.593	0.147	0.405	0.697
$Cu_{53.9}Zr_{39.2}Al_{4.9}Er_2$	698							

Table 3.6: Density and room temperature elastic constants for various Cu-based BMGs.

Composition	ρ (g/cm^3)	L (GPa)	G (GPa)	B (GPa)	E (GPa)	ν
$Cu_{53.9}Zr_{39.2}Al_{4.9}Er_2$	6.987	155.4	32.6	111.9	89.2	0.367
$Cu_{47.5}Zr_{47.5}Al_5$	7.057	161.5	32.4	118.3	89.1	0.374
$Cu_{47.5}Zr_{38}Hf_{9.5}Al_5$	7.006	159.2	32.3	116.2	88.7	0.373
$Cu_{47}Zr_{47}Al_6$	6.972	157.2	32.2	114.3	88.3	0.371
$Cu_{46.25}Zr_{46.25}Al_{7.5}$	7.002	161.8	34.4	116.0	93.8	0.365
$Cu_{46.25}Zr_{45.25}Al_{7.5}Sn_1$	7.054	165.7	35.7	118.1	97.3	0.363
$Cu_{42.5}Ti_{41.5}Ni_{7.5}Hf_5Zr_{2.5}Si_1$	7.047	171.4	37.2	121.8	101.3	0.361

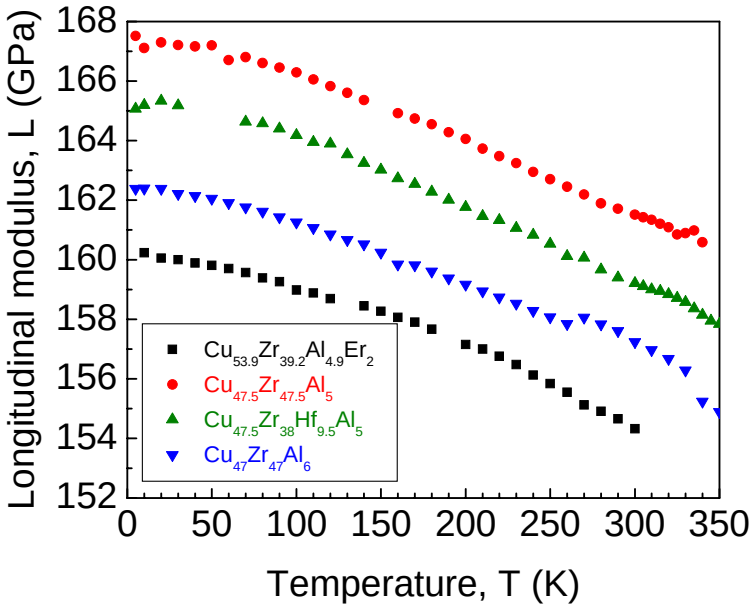

Figure 3.22: Longitudinal modulus *L* as a function of temperature for Cu-based BMGs $Cu_{53.9}Zr_{39.2}Al_{4.9}Er_2$ (■), $Cu_{47.5}Zr_{47.5}Al_5$ (●), $Cu_{47.5}Zr_{38}Hf_{9.5}Al_5$ (▲) and $Cu_{47}Zr_{47}Al_6$ (▼).

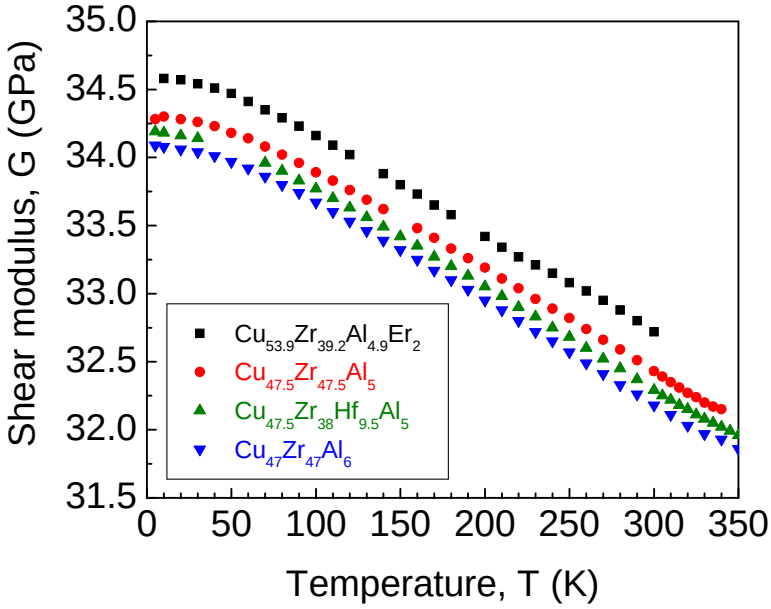

Figure 3.23: Shear modulus *G* as a function of temperature for Cu-based BMGs $Cu_{53.9}Zr_{39.2}Al_{4.9}Er_2$ (■), $Cu_{47.5}Zr_{47.5}Al_5$ (●), $Cu_{47.5}Zr_{38}Hf_{9.5}Al_5$ (▲) and $Cu_{47}Zr_{47}Al_6$ (▼).

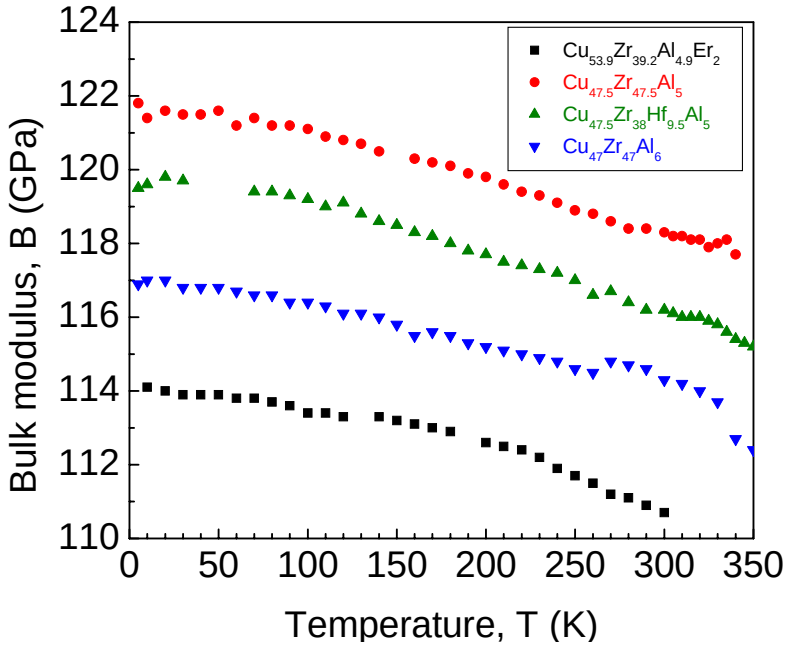

Figure 3.24: Bulk modulus *B* as a function of temperature for Cu-based BMGs $Cu_{53.9}Zr_{39.2}Al_{4.9}Er_2$ (■), $Cu_{47.5}Zr_{47.5}Al_5$ (●), $Cu_{47.5}Zr_{38}Hf_{9.5}Al_5$ (▲) and $Cu_{47}Zr_{47}Al_6$ (▼).

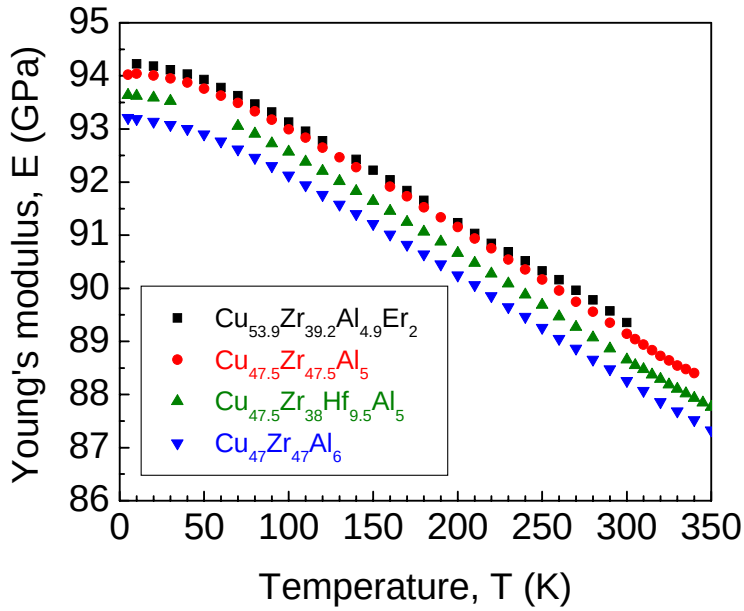

Figure 3.25: Young's modulus *E* as a function of temperature for Cu-based BMGs $Cu_{53.9}Zr_{39.2}Al_{4.9}Er_2$ (■), $Cu_{47.5}Zr_{47.5}Al_5$ (●), $Cu_{47.5}Zr_{38}Hf_{9.5}Al_5$ (▲) and $Cu_{47}Zr_{47}Al_6$ (▼).

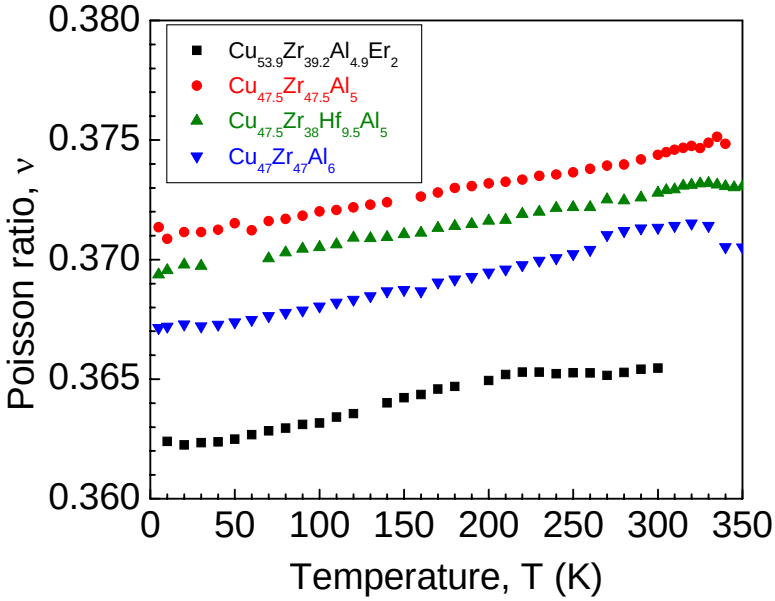

Figure 3.26: Poisson ratio ν as a function of temperature for Cu-based BMGs $Cu_{53.9}Zr_{39.2}Al_{4.9}Er_2$ (■), $Cu_{47.5}Zr_{47.5}Al_5$ (●), $Cu_{47.5}Zr_{38}Hf_{9.5}Al_5$ (▲) and $Cu_{47}Zr_{47}Al_6$ (▼).

CHAPTER 4

CALCIUM BASED BULK METALLIC GLASSES

Ca-based BMGs are a relatively new class of amorphous alloys, first reported by Amiya and Inoue in 2002 (Amiya, 2002a). Various ternary and quaternary systems, including Ca-Mg-Zn, Ca-Mg-Cu, Ca-Mg-Zn-Cu, Ca-Mg-Ag-Cu, have been successfully synthesized (Amiya, 2002a) (Amiya, 2002 b) (Guo, 2004) (Senkov, 2004a) (Senkov, 2004 b) (Park, 2004) (Park, 2005) (Senkov, 2005) (Senkov, 2006). Unique properties have been reported, such as low density (~2.0 g/cm^3) and low Young's modulus comparable to the modulus of human bones (Senkov, 2006). In addition, Ca-based BMGs have low glass transition temperatures (~390 K), which makes them very attractive for studies near the glass transition temperature.

Ca-based BMGs, $Ca_{50}Mg_{20}Cu_{30}$, $Ca_{55}Mg_{18}Zn_{11}Cu_{16}$ and $Ca_{65}Mg_{15}Zn_{20}$, were prepared by Senkov et al. using the method as follows (Senkov, 2005) (Senkov, 2006). Mixtures of pure elements (99.9 %) were induction melted in a water-cooled copper crucible in an argon atmosphere and the alloys were then re-melted in a quartz crucible and cast into a water-cooled copper mold. The characteristic temperatures (glass transition temperature T_g, crystallization temperature T_x and liquidus temperature T_l) and glass forming ability parameters of these samples are listed in Table 4.1.

The longitudinal modulus L, shear modulus G, bulk modulus B, Young's modulus E and Poisson ratio ν for Ca-based glasses with three different compositions are plotted in Figure 4.1 to Figure 4.5, respectively. A clear transition in the temperature-dependence of the elastic constants is observed at ~362 K for $Ca_{65}Mg_{15}Zn_{20}$, ~386 K for $Ca_{55}Mg_{18}Zn_{11}Cu_{16}$ and ~400 K for $Ca_{50}Mg_{20}Cu_{30}$. Below the transition temperature, all moduli decrease with increasing temperature, while the Poisson ratio increases with increasing temperature. Above the transition temperature, the rate of softening is significantly decreased or is fully arrested.

Table 4.1: Glass transition temperature T_g, crystallization temperature T_x, liquidus temperature T_l, supercooled liquid region ΔT_x, reduced glass transition temperature T_{rg}, Hruby factor K_{gl}, γ, γ_m, and critical casting thickness d_{max} for Ca-based BMGs, determined by differential scanning calorimetry (DSC) with the heating rate at 0.667 K/s.

Composition	T_g (K)	T_x (K)	T_l (K)	ΔT_x (K)	T_{rg}	K_{gl}	γ	γ_m	d_{max} (mm)
$Ca_{50}Mg_{20}Cu_{30}$	401	442	690	41	0.581	0.165	0.405	0.700	8
$Ca_{55}Mg_{18}Zn_{11}Cu_{16}$	392	441	622	49	0.630	0.271	0.435	0.788	>10
$Ca_{65}Mg_{15}Zn_{20}$	375	410	630	35	0.595	0.159	0.408	0.706	6

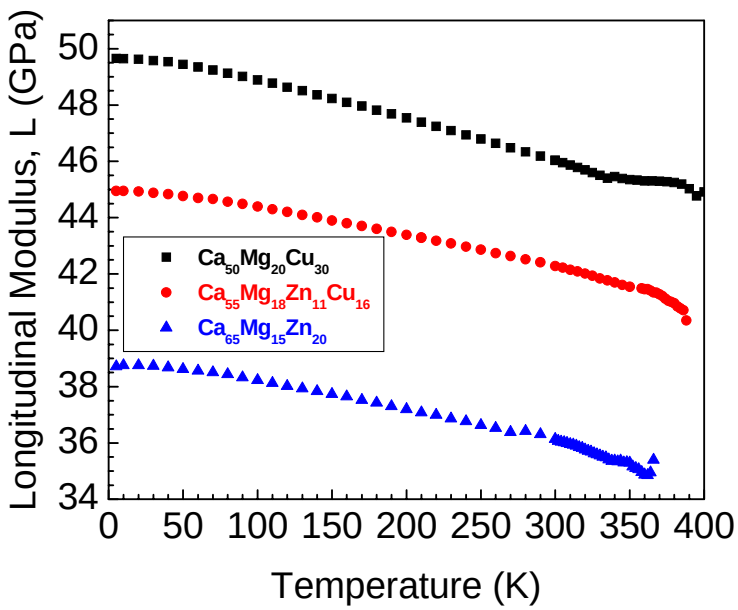

Figure 4.1: Longitudinal modulus L as a function of temperature for $Ca_{50}Mg_{20}Cu_{30}$ (■), $Ca_{55}Mg_{18}Zn_{11}Cu_{16}$ (●) and $Ca_{65}Mg_{15}Zn_{20}$ (▲).

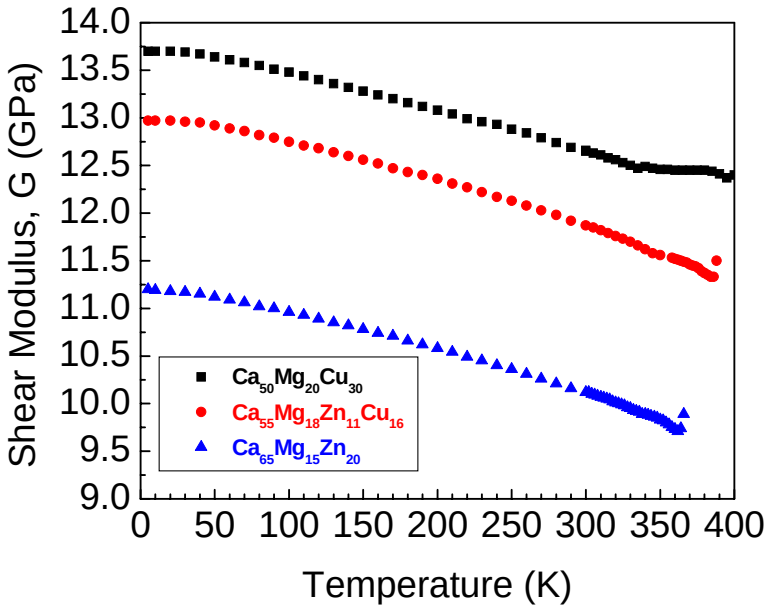

Figure 4.2: Shear modulus *G* as a function of temperature for $Ca_{50}Mg_{20}Cu_{30}$ (■), $Ca_{55}Mg_{18}Zn_{11}Cu_{16}$ (●) and $Ca_{65}Mg_{15}Zn_{20}$ (▲).

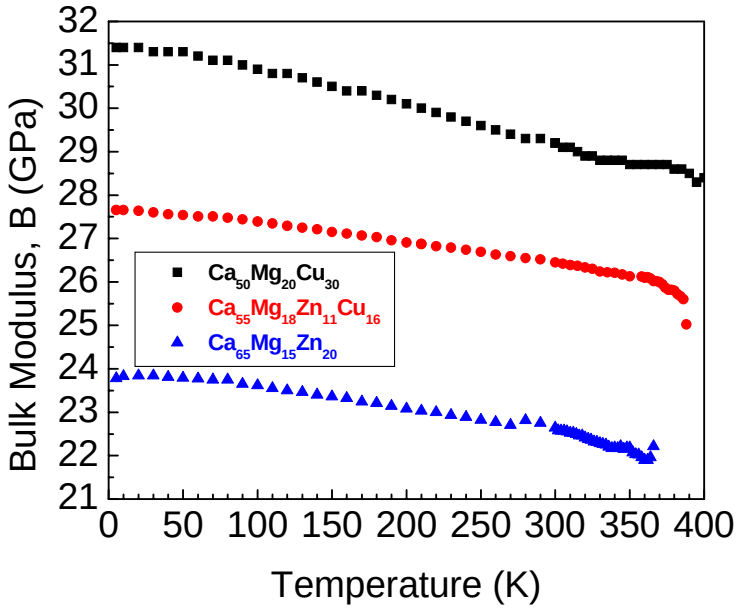

Figure 4.3: Bulk modulus *B* as a function of temperature for $Ca_{50}Mg_{20}Cu_{30}$ (■), $Ca_{55}Mg_{18}Zn_{11}Cu_{16}$ (●) and $Ca_{65}Mg_{15}Zn_{20}$ (▲).

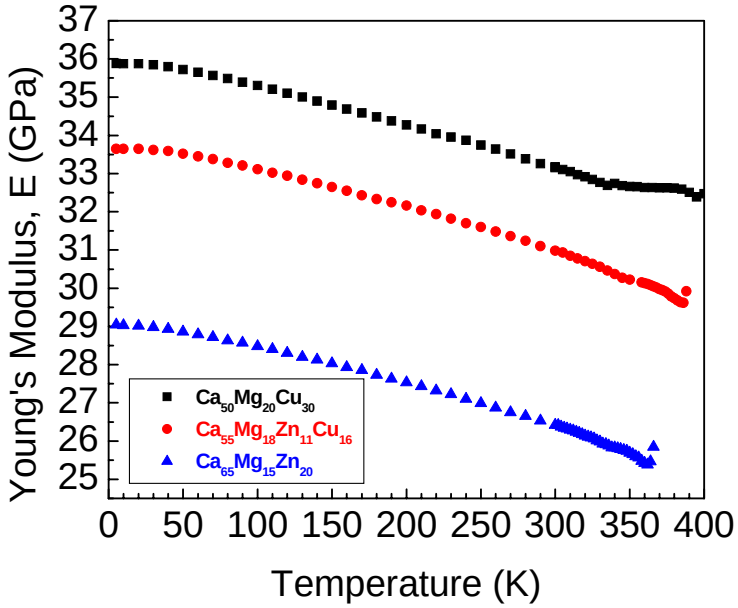

Figure 4.4: Young's modulus E as a function of temperature for $Ca_{50}Mg_{20}Cu_{30}$ (■), $Ca_{55}Mg_{18}Zn_{11}Cu_{16}$ (●) and $Ca_{65}Mg_{15}Zn_{20}$ (▲).

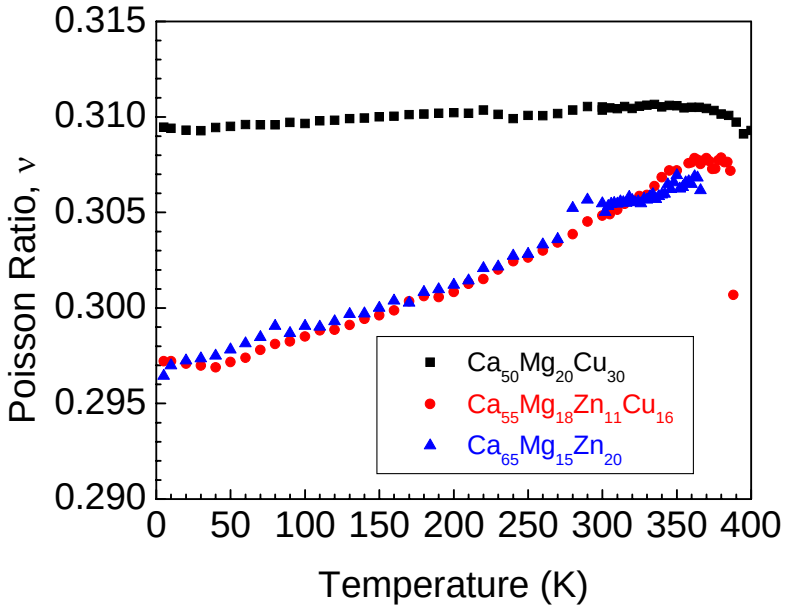

Figure 4.5: Poisson ratio ν as a function of temperature for $Ca_{50}Mg_{20}Cu_{30}$ (■), $Ca_{55}Mg_{18}Zn_{11}Cu_{16}$ (●) and $Ca_{65}Mg_{15}Zn_{20}$ (▲).

The transition temperatures observed in our data are roughly equivalent to the T_g values for the respective glasses, suggesting that structural relaxations are responsible for the observed transitions. This is also similar to observations in Zr-based BMGs, as discussed in section 3.1.2. The transitions observed in our data happen at temperatures slightly below the expected T_g. This can be explained because T_g and T_x depend on the heating rate. Table 4.2 lists the dependence of T_g and T_x on heating rate for $Ca_{65}Mg_{15}Zn_{20}$. It indicates that T_g and T_x decrease with decreasing heating rate. The heating rate is rather slow in our measurements, leading to a lower transition temperature than expected T_g.

A systematic influence of composition on elastic moduli is apparent in Figure 4.1 to Figure 4.5, where moduli increase with increasing Cu and decreasing Ca concentration. This follows the trend for the elastic properties of the constituent elements (Table 4.3) (http://www.webelements.com/webelements/elements/). The calculated moduli based on atomic fraction and volume fraction of the components are compared with the values measured by RUS at room temperature in Table 4.4. These calculations support the observed composition dependence, and estimates based on constituent volume fraction provide very good agreement with the experimental results.

Table 4.2: Dependence of glass transition temperature T_g and crystallization temperature T_x on the heating rate for $Ca_{65}Mg_{15}Zn_{20}$.

Heating rate (K/min)	T_g (K)	T_x (K)
1[a]		377.2
5[a]	355.1	387.5
40[a]	376.8	406.6
40[a]	398.0	424.1

[a] Continuous heating.

[b] Isothermal holding at 375 K for 30 min followed by continuous heating.

Table 4.3: Atomic volume, V_A, density, ρ and elastic constants of elements (http://www.webelements.com/webelements/elements/).

Element	V_A (cm^3/mol)	ρ (g/cm^3)	G (GPa)	B (GPa)	E (GPa)	ν
Ca	26.20	1.55	7.4	17	20	0.31
Mg	14.00	1.74	17	45	45	0.29
Zn	9.16	7.14	43	70	108	0.25
Cu	7.11	8.92	48	140	130	0.34

Table 4.4: Comparison of measured elastic constants (meas.) at room temperature with the calculated values based on atomic fraction ($cal_{at.}$) and volume fraction ($cal_{vol.}$) of components.

Property	$Ca_{50}Mg_{20}Cu_{30}$			$Ca_{55}Mg_{18}Zn_{11}Cu_{16}$			$Ca_{65}Mg_{15}Zn_{20}$		
	meas.	$cal_{at.}$	$cal_{vol.}$	meas.	$cal_{at.}$	$cal_{vol.}$	meas.	$cal_{at.}$	$cal_{vol.}$
G (GPa)	12.6	21.5	13.7	11.9	19.5	13.0	10.1	16.0	11.5
B (GPa)	29	60	35.9	26	48	30.8	23	32	24.4
E (GPa)	33.2	58.0	36.9	31.0	51.8	34.5	26.4	32	30.2
ν	0.311	0.315	0.310	0.305	0.305	0.306	0.306	0.295	0.303

The internal friction Q^{-1} of the Ca-based BMGs as a function of temperature is shown in Figure 4.6. The internal friction gradually increases with increasing temperature, and the increase becomes quite dramatic near the glass transition temperature. A similar increase in Q^{-1} has been observed by Ichitsubo et al. (Ichitsubo, 2003) in Zr-based BMGs.

The heat capacity of $Ca_{50}Mg_{20}Cu_{30}$, $Ca_{55}Mg_{18}Zn_{11}Cu_{16}$ and $Ca_{65}Mg_{15}Zn_{20}$, measured as a function of temperature, is shown in Figure 4.7. There is a peak at 387 K for $Ca_{55}Mg_{18}Zn_{11}Cu_{16}$ and at 364 K for $Ca_{65}Mg_{15}Zn_{20}$, respectively. The peak temperatures are consistent with the transition temperatures observed in elastic constant measurements. The difference between the peak temperatures and the glass transition temperature measured using DSC is again attributed to the difference in heating rate.

Ca-based BMGs, $Ca_{55}Mg_{15}Zn_{15}Al_{10}Cu_5$ and $Ca_{60}Mg_{15}Zn_{15}Al_{10}$ were prepared by Poon's group in University of Virginia using an induction furnace under a flowing argon atmosphere (Guo, 2004). The glass transition temperatures of $Ca_{55}Mg_{15}Zn_{15}Al_{10}Cu_5$ and $Ca_{60}Mg_{15}Zn_{15}Al_{10}$ determined using DSC are 446 K and 443 K, respectively. The density and room temperature elastic constants are listed in Table 4.5. They are close to the values for other Ca-based BMGs.

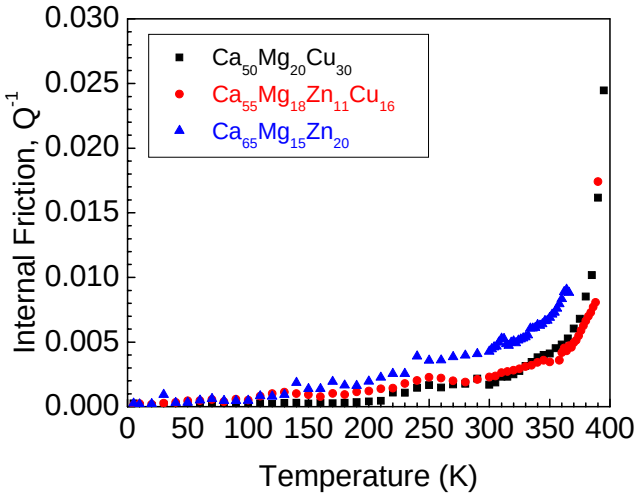

Figure 4.6: Internal friction Q^{-1} as a function of temperature for $Ca_{50}Mg_{20}Cu_{30}$ (■), $Ca_{55}Mg_{18}Zn_{11}Cu_{16}$ (●) and $Ca_{65}Mg_{15}Zn_{20}$ (▲).

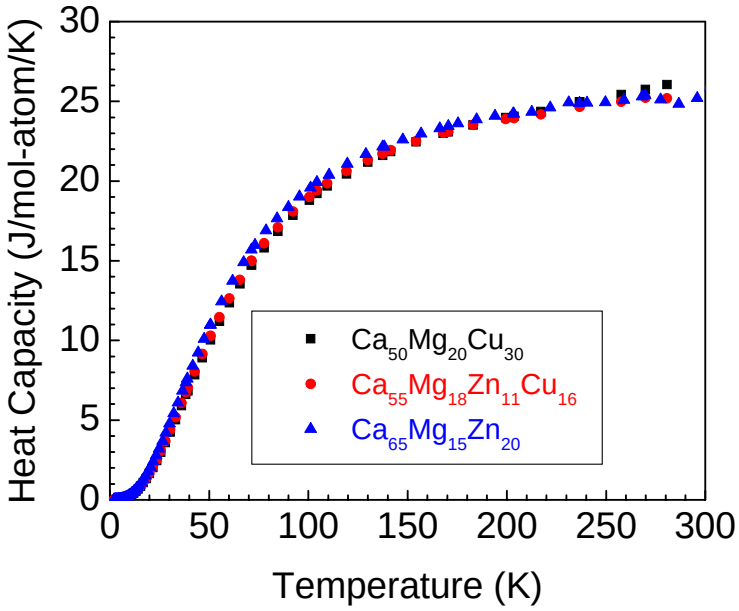

(a)

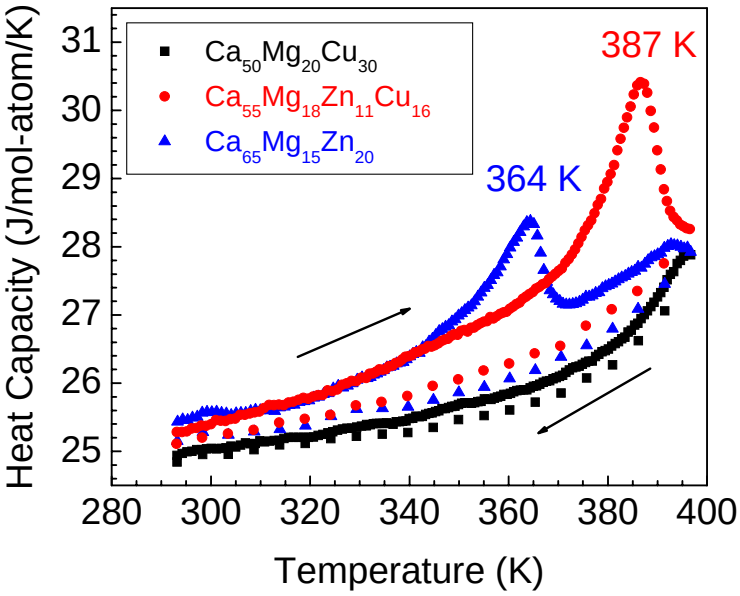

(b)

Figure 4.7: Heat capacity as a function of temperature for $Ca_{50}Mg_{20}Cu_{30}$ (■), $Ca_{55}Mg_{18}Zn_{11}Cu_{16}$ (●) and $Ca_{65}Mg_{15}Zn_{20}$ (▲). (a) 3-300 K. (b) 295-398 K.

Table 4.5: Density and room temperature elastic constants for various Ca-based BMGs.

Composition	ρ (g/cm^3)	L (GPa)	G (GPa)	B (GPa)	E (GPa)	ν
$Ca_{55}Mg_{15}Zn_{15}Al_{10}Cu_5$	2.217	48.3	13.4	30.4	35.1	0.308
$Ca_{60}Mg_{15}Zn_{15}Al_{10}$	2.056	46.2	12.5	29.5	32.9	0.314
$Ca_{50}Mg_{20}Cu_{30}$	2.584	46.0	12.7	29.2	33.2	0.311
$Ca_{55}Mg_{18}Zn_{11}Cu_{16}$	2.404	42.3	11.9	26.5	31.0	0.305
$Ca_{65}Mg_{15}Zn_{20}$	2.040	36.1	10.1	22.6	26.4	0.306

The dependence of the bulk modulus B, shear modulus G, Young's modulus E and longitudinal modulus L on the glass transition temperature T_g and the crystallization temperature T_x for Zr-based, Cu-based and Ca-based BMGs is shown in Figures 4.8 and 4.9. Linear correlations of elastic moduli with T_g and with T_x are observed, confirming results reported by Wang and Li (Wang, 2006) (Li, 2008).

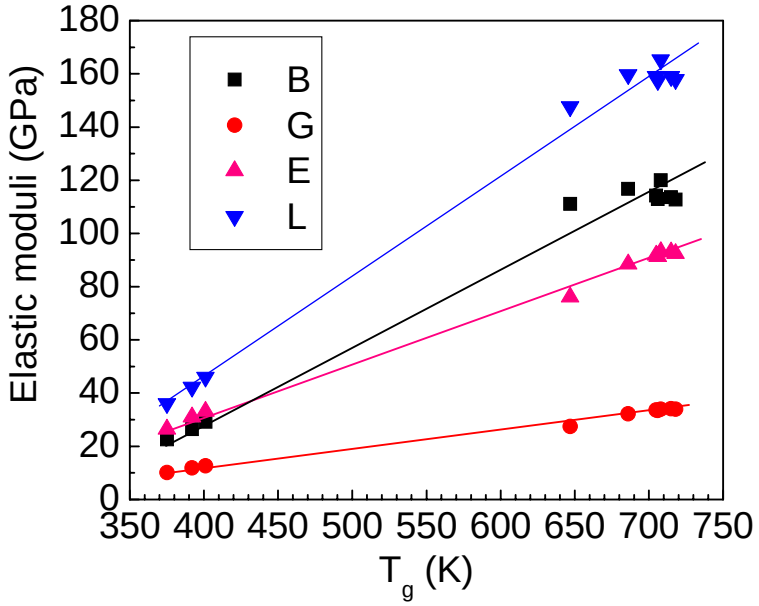

Figure 4.8: Dependence of bulk modulus *B*, shear modulus *G*, Young's modulus *E* and longitudinal modulus *L* on glass transition temperature T_g for Zr-based, Cu-based and Ca-based BMGs.

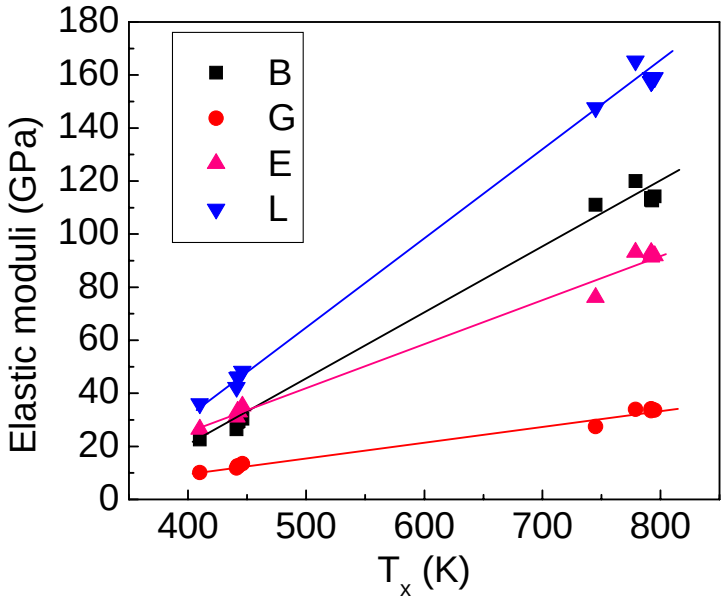

Figure 4.9: Dependence of bulk modulus *B*, shear modulus *G*, Young's modulus *E* and longitudinal modulus *L* on crystallization temperature T_x for Zr-based, Cu-based and Ca-based BMGs.

CHAPTER 5

MODEL TO PREDICT THE TEMPERATURE DEPENDENCE OF ELASTIC MODULI

In 1970, Varshni (Varshni 1970) examined the temperature dependence of 57 elastic constants for 22 substances, which led to the so-called Varshni equation (see chapter 3, Equation 3.1), describing the temperature-dependence of elastically "normal' solids. Even though this equation has only marginal theoretical justification (s and t are arbitrary fitting parameters), it has been shown to adequately model the temperature-dependence of the elastic moduli of a large variety of solids. In this chapter, we report on our attempt to take this Varshni model one step further, and eliminate the fitting parameters with the goal of developing a model that can be used to extrapolate/calculate elastic moduli measured at room temperature to lower and/or higher temperatures.

Our approach is based on two assumptions. The first assumption is inspired by Varshni's remark that in the case of metals, melting takes place when the shear modulus G is reduced to 55 % of the modulus at 0 K, i.e. $G(T_m) = (1\text{-}n_G)G_0$, with $n_G = 0.45$, T_m the melting temperature and G_0 the shear modulus at 0 K. The second assumption is to take $t = \theta_D$, the Debye temperature of the solid, which can be obtained from the room temperature elastic moduli using Equation 2.19. Using the above assumptions, the Varshni-parameter s_G can be obtained from

$$s_G = \frac{G(T_{RT})}{\dfrac{1}{n_G\left(e^{\frac{\theta_D}{T_m}}-1\right)} - \dfrac{1}{e^{\frac{\theta_D}{T_{RT}}}-1}} \tag{5.1}$$

with T_{RT} room temperature. Consequently, the entire temperature dependence of the shear modulus can be determined using

$$G(T) = G(T_{RT}) + \frac{s_G}{e^{\frac{\theta_D}{T_{RT}}}-1} - \frac{s_G}{n_G\left(e^{\frac{\theta_D}{T}}-1\right)} \tag{5.2}$$

Figure 5.1 compares this model calculation with recently obtained measurements of the temperature-dependence of the shear modulus for a variety of bulk metallic glasses (Zhang, 2007b) (Zhang, 2007c) and shows excellent agreement between our model and the experimental data for the shear modulus. The solid lines in the figure were obtained from Equation 5.1 and Equation 5.2, using the "average" melting temperature of the compound, listed in Table 5.1 together with the values for the parameters used in our calculation. The "average" melting temperature was obtained using $T_m = \sum_i x_i T_{m,i}$ with x_i the atomic fraction of component i and $T_{m,i}$ its melting temperature. The average melting temperature represents the lattice elastic energy of a multi-component system better than the real melting temperature, which is affected by subtle balance in free energy against liquid and is lowered, for instance, in the eutectic alloy system. The average melting temperature provides a good zeroth-order estimate of the relative magnitude of v_0B, with v_0 the atomic volume and B the average bulk modulus. There is good correlation (Egami, 1982) (Egami, 1984) between the average melting temperature and the glass transition temperature, which is related to the elastic moduli (Egami, 2007).

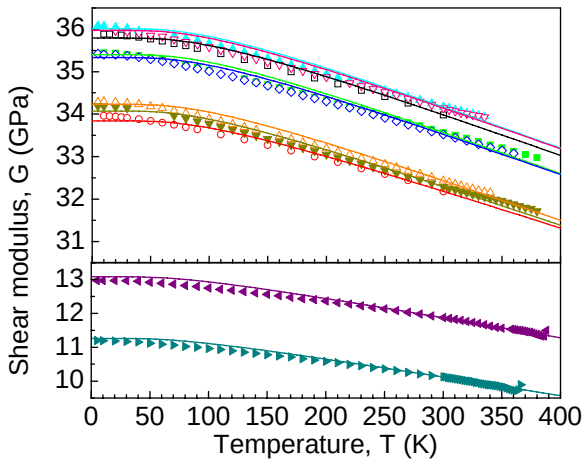

Figure 5.1: Temperature dependence of shear modulus for Zr-based BMGs, $Zr_{50}Cu_{30}Ni_{10}Al_{10}$ (□), $Zr_{50}Cu_{40}Al_{10}$ (■), $Zr_{52.5}Cu_{17.9}Ni_{14.6}Al_{10}Ti_5$ (○), $Zr_{50}Cu_{35}Al_{10}Pd_5$ (▲), $Zr_{50}Cu_{33}Al_{10}Pd_7$ (◊) and $Zr_{50}Cu_{31}Al_{10}Pd_9$ (▽), Cu-based BMGs, $Cu_{47.5}Zr_{47.5}Al_5$ (Δ) and $Cu_{47.5}Zr_{38}Hf_{9.5}Al_5$ (▼) and Ca-based BMGs, $Ca_{55}Mg_{18}Zn_{11}Cu_{16}$ (◄) and $Ca_{65}Mg_{15}Zn_{20}$ (►). The solid line is the model calculation.

Table 5.1: Averaged melting temperature T_m, density ρ, shear modulus at room temperature $G(T_{RT})$, bulk modulus at room temperature $B(T_{RT})$, Debye temperature θ_D, s_G and s_B for Zr-based, Cu-based and Ca-based BMGs.

Composition	T_m (K)	ρ (g/cm^3)	$G(T_{RT})$ (GPa)	$B(T_{RT})$ (GPa)	θ_D (K)	s_G (GPa)	s_B (GPa)
$Zr_{50}Cu_{30}Ni_{10}Al_{10}$	1737.5	6.862	33.98	120.0	285.28	2.8738	4.8302
$Zr_{50}Cu_{40}Al_{10}$	1700.5	6.714	33.56	116.1	283.83	2.8934	4.7605
$Zr_{52.5}Cu_{17.9}Ni_{14.6}Al_{10}Ti_5$	1802.9	6.632	32.18	116.8	279.73	2.5558	4.4187
$Zr_{50}Cu_{35}Al_{10}Pd_5$	1724.0	6.890	34.17	121.7	282.58	2.8866	4.8912
$Zr_{50}Cu_{33}Al_{10}Pd_7$	1733.4	6.771	33.52	107.3	279.15	2.7780	4.2308
$Zr_{50}Cu_{31}Al_{10}Pd_9$	1742.8	7.067	34.14	130.1	279.47	2.8153	5.1053
$Cu_{47.5}Zr_{47.5}Al_5$	1702.4	7.058	32.43	118.3	275.52	2.7058	4.6926
$Cu_{47.5}Zr_{38}Hf_{9.5}Al_5$	1738.3	7.006	32.29	116.2	265.73	2.5321	4.3329
$Ca_{55}Mg_{18}Zn_{11}Cu_{16}$	1072.8	2.404	11.87	26.45	236.33	1.4505	1.5019
$Ca_{65}Mg_{15}Zn_{20}$	1001.7	2.040	10.12	22.64	226.03	1.2827	1.3264

The next step is to test the validity of this model to calculate/predict other moduli as well. As discussed above, the shear modulus in metals is known to decrease about 45 % between 0 K and melting temperature. The bulk modulus, however, is not expected to change as much. It has been shown that the topology of the dense random packing structure is unstable against shear deformation, leading to obvious softening of the shear modulus of the glassy state compared to the crystalline state (Suzuki, 1985). On the other hand, the bulk modulus of the glassy state is about the same as that of the crystalline state (Egami, 1982). The distribution of the local atomic level shear modulus indicates that there are some atomic sites with vanishingly small values of shear modulus. This is not the case for the bulk modulus, leading to less softening of the bulk modulus (Egami, 1982). A careful evaluation of the available data for the bulk modulus B shows that a typical variation in B is of the order of 20-25 % in metals. We therefore took our above model with $n_B = 1-B(T_m)/B_0 = 0.22$, and compared the calculated temperature dependence to our experimental data for the bulk modulus, shown in Figure 5.2. Very good agreement is reached for the various alloys.

In a final test, we calculated the temperature-dependence of the longitudinal modulus, Young's modulus and Poisson ratio using Equation 2.16, Equation 2.17 and Equation 2.18 and the parameters obtained from the calculated shear and bulk modulus (Table 5.1). Results are shown in Figure 5.3, Figure 5.4 and Figure 5.5. Adequate agreement is reached for all moduli for this large variety of alloys: the differences between the predicted values and the experimental results are less than 1 %. The excellent agreement between the model calculation and the experimental data indicates that our attempt to eliminate the arbitrary Varshni parameters using two basic assumptions is quite successful. However, it needs to be pointed out that using the model for BMGs with various compositions may require slight modification of n_B for bulk modulus.

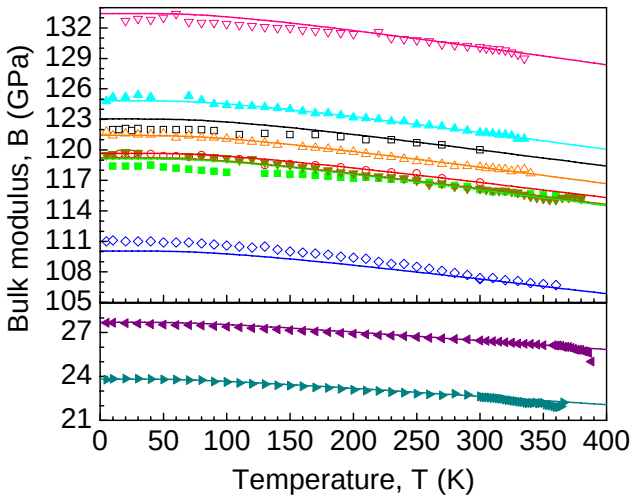

Figure 5.2: Temperature dependence of bulk modulus for Zr-based BMGs, $Zr_{50}Cu_{30}Ni_{10}Al_{10}$ (□), $Zr_{50}Cu_{40}Al_{10}$ (■), $Zr_{52.5}Cu_{17.9}Ni_{14.6}Al_{10}Ti_5$ (○), $Zr_{50}Cu_{35}Al_{10}Pd_5$ (▲), $Zr_{50}Cu_{33}Al_{10}Pd_7$ (◊) and $Zr_{50}Cu_{31}Al_{10}Pd_9$ (▽), Cu-based BMGs, $Cu_{47.5}Zr_{47.5}Al_5$ (Δ) and $Cu_{47.5}Zr_{38}Hf_{9.5}Al_5$ (▼) and Ca-based BMGs, $Ca_{55}Mg_{18}Zn_{11}Cu_{16}$ (◄) and $Ca_{65}Mg_{15}Zn_{20}$ (►). The solid line is the model calculation.

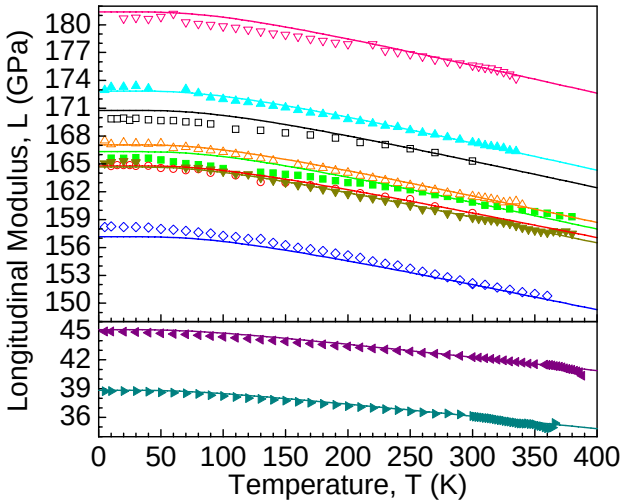

Figure 5.3: Temperature dependence of longitudinal modulus for Zr-based BMGs, $Zr_{50}Cu_{30}Ni_{10}Al_{10}$ (□), $Zr_{50}Cu_{40}Al_{10}$ (■), $Zr_{52.5}Cu_{17.9}Ni_{14.6}Al_{10}Ti_5$ (○), $Zr_{50}Cu_{35}Al_{10}Pd_5$ (▲), $Zr_{50}Cu_{33}Al_{10}Pd_7$ (◊) and $Zr_{50}Cu_{31}Al_{10}Pd_9$ (▽), Cu-based BMGs, $Cu_{47.5}Zr_{47.5}Al_5$ (Δ) and $Cu_{47.5}Zr_{38}Hf_{9.5}Al_5$ (▼) and Ca-based BMGs, $Ca_{55}Mg_{18}Zn_{11}Cu_{16}$ (◄) and $Ca_{65}Mg_{15}Zn_{20}$ (►). The solid line is the model calculation.

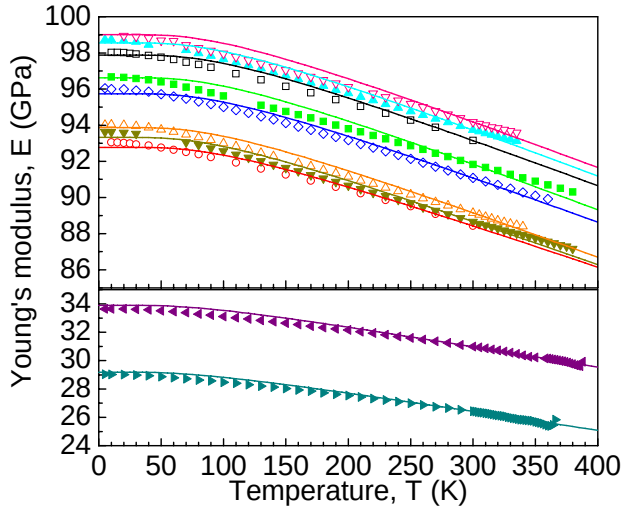

Figure 5.4: Temperature dependence of Young's modulus for Zr-based BMGs, $Zr_{50}Cu_{30}Ni_{10}Al_{10}$ (□), $Zr_{50}Cu_{40}Al_{10}$ (■), $Zr_{52.5}Cu_{17.9}Ni_{14.6}Al_{10}Ti_5$ (○), $Zr_{50}Cu_{35}Al_{10}Pd_5$ (▲), $Zr_{50}Cu_{33}Al_{10}Pd_7$ (◊) and $Zr_{50}Cu_{31}Al_{10}Pd_9$ (▽), Cu-based BMGs, $Cu_{47.5}Zr_{47.5}Al_5$ (Δ) and $Cu_{47.5}Zr_{38}Hf_{9.5}Al_5$ (▼) and Ca-based BMGs, $Ca_{55}Mg_{18}Zn_{11}Cu_{16}$ (◄) and $Ca_{65}Mg_{15}Zn_{20}$ (►). The solid line is the model calculation.

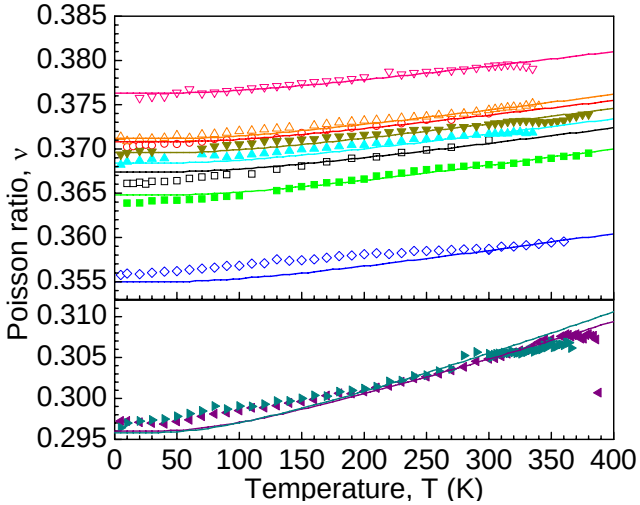

Figure 5.5: Temperature dependence of Poisson ratio for Zr-based BMGs, $Zr_{50}Cu_{30}Ni_{10}Al_{10}$ (□), $Zr_{50}Cu_{40}Al_{10}$ (■), $Zr_{52.5}Cu_{17.9}Ni_{14.6}Al_{10}Ti_5$ (○), $Zr_{50}Cu_{35}Al_{10}Pd_5$ (▲), $Zr_{50}Cu_{33}Al_{10}Pd_7$ (◊) and $Zr_{50}Cu_{31}Al_{10}Pd_9$ (▽), Cu-based BMGs, $Cu_{47.5}Zr_{47.5}Al_5$ (Δ) and $Cu_{47.5}Zr_{38}Hf_{9.5}Al_5$ (▼) and Ca-based BMGs, $Ca_{55}Mg_{18}Zn_{11}Cu_{16}$ (◄) and $Ca_{65}Mg_{15}Zn_{20}$ (►). The solid line is the model calculation.

CHAPTER 6

CORRELATION WITH OTHER WORK AND PERSPECTIVES FOR FUTURE WORK

The fracture strength, fatigue limit and Vickers hardness of Zr-based, Cu-based and Ca-based BMGs are listed in Table 6.1. Their correlations with elastic moduli are shown in Figures 6.1, 6.2 and 6.3, respectively. Elastic moduli increase with increasing fracture strength and Vickers hardness. Similar observations have been reported by Inoue (Inoue, 2002). For Zr-based and Cu-based BMGs, which have a fatigue limit between 0.2 and 1.0 GPa, the elastic moduli are barely dependent on the fatigue limit. Ca-based BMGs have much lower fatigue limit than Zr-based and Cu-based BMGs, and they also display lower elastic moduli. The dependence of fracture strength and fatigue limit on the Poisson ratio is shown in Figure 6.4. BMGs with higher Poisson ratio tend to display higher fracture strength. Weak correlation is shown between the fatigue limit and the Poisson ratio. The dependence of the ratio of fatigue limit to fracture strength on the Poisson ratio is shown in Figure 6.5.

Table 6.1: Fracture strength, fatigue limit and Vickers hardness of Zr-based, Cu-based and Ca-based BMGs.

Composition	Fracture strength, σ_{frac} (GPa)	Fatigue limit, σ_{fati} (GPa)	Vickers harness, H_v (GPa)	Reference
$Zr_{50}Cu_{40}Al_{10}$	1.821	0.752	506	(Wang, 2004a)
$Zr_{50}Cu_{30}Ni_{10}Al_{10}$	1.900	0.865	504	(Wang, 2004a)
$Zr_{50}Cu_{37}Al_{10}Pd_3$	1.899	0.983		(Wang, 2007)
$Cu_{47.5}Zr_{47.5}Al_5$	1.85	0.224		(Qiao, 2007)
$Cu_{47.5}Zr_{38}Hf_{9.5}Al_5$	1.59	0.378		(Qiao, 2007)
$Ca_{65}Mg_{15}Zn_{20}$	0.364	0.140	1.42	(Wang, unpublished)

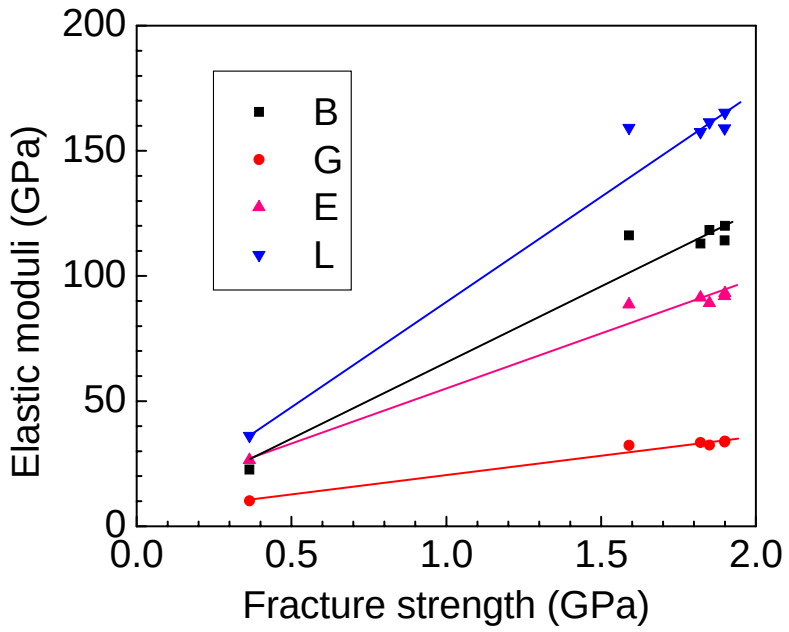

Figure 6.1: Correlation of elastic moduli with fracture strength.

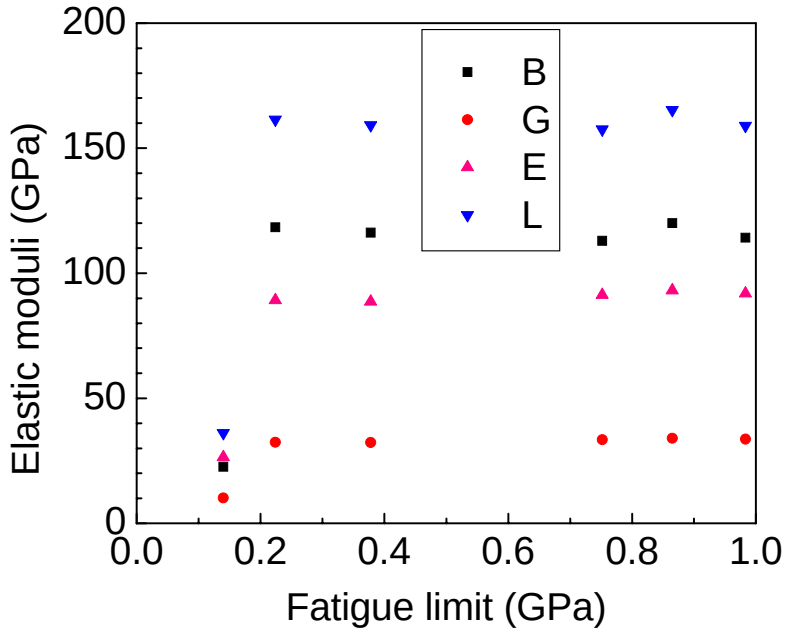

Figure 6.2: Correlation of elastic moduli with fatigue limit.

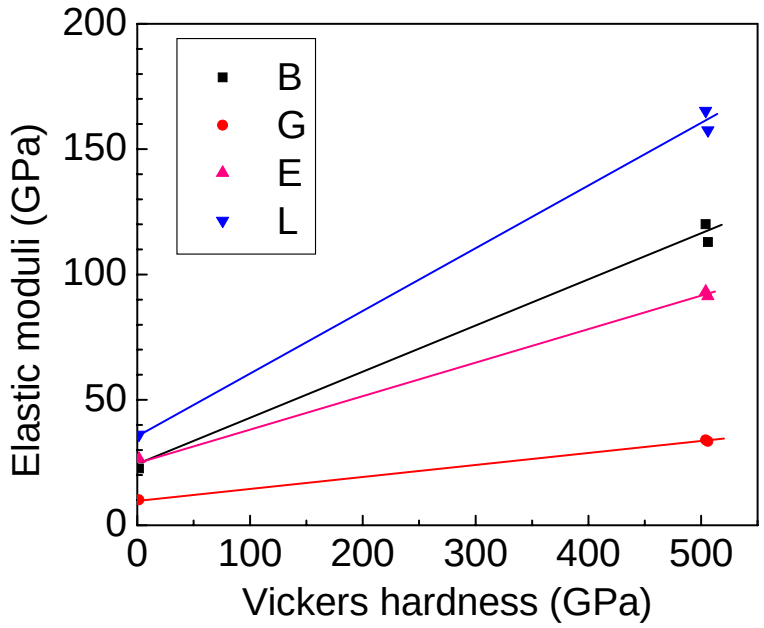

Figure 6.3: Correlation of elastic moduli with Vickers hardness.

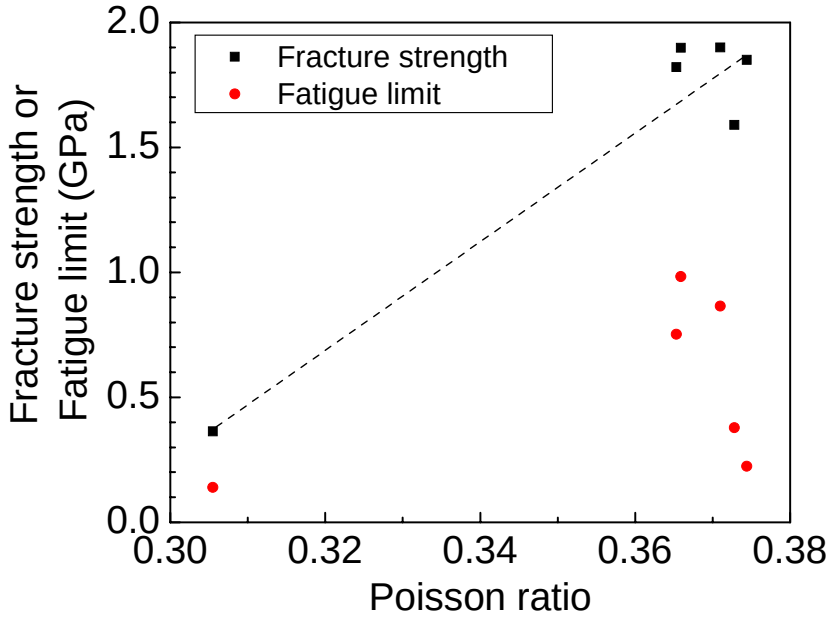

Figure 6.4: The dependence of fatigue limit and fracture strength on the Poisson ratio.

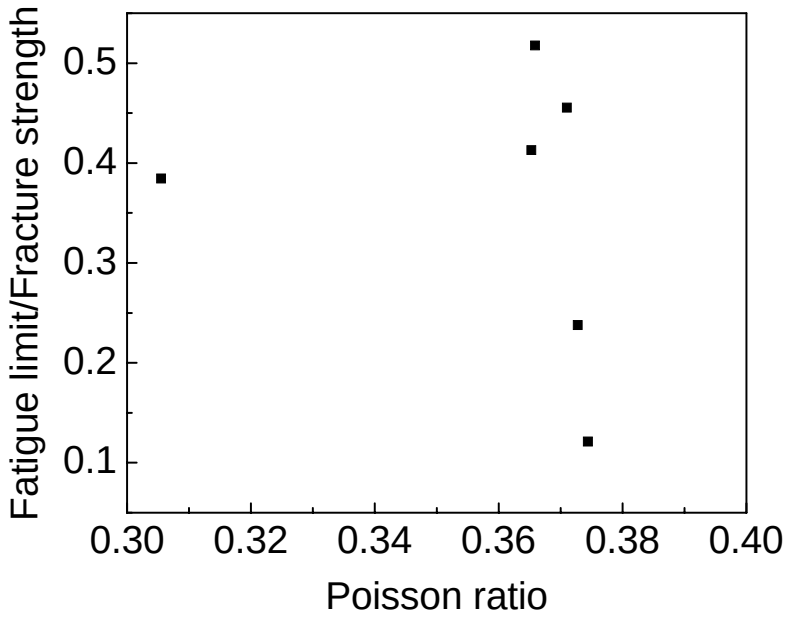

Figure 6.5: The dependence of the ratio of fatigue limit to fracture strength on the Poisson ratio.

Wang et al. reported that the ratio of fatigue limit to fracture strength tends to increase with increasing Poisson ratio (Wang, 2007). This claim is not confirmed by our results.

Limited data of elastic constants and mechanical properties are available for various BMGs. In the future, more data point can be added in above figures to carefully study the correlation between elastic constants and mechanical properties. For instance, more work can be done to investigate BMGs with Poisson ratio between 0.31 and 0.36, and Vickers hardness between 2 and 500 GPa. Furthermore, it needs to be pointed out that the mechanical properties of BMGs reported in literature are usually obtained under various conditions, leading to the scattering in the data. In the future, a systematic study is needed.

CONCLUSIONS

Elastic properties of Zr-based, Cu-based and Ca-based BMGs were investigated. Below the glass transition temperature, elastic constants show "normal behavior", i.e. with increasing temperature, longitudinal modulus, shear modulus, bulk modulus and Young's modulus decrease but Poisson ratio increases. Above the glass transition temperature, changes in the trends occur due to structural relaxation and crystallization. The elastic properties of BMGs are sensitive to their compositions. Reasonable estimation of elastic properties of BMGs can be obtained from the elastic constants of the constituent elements. A simple model is developed to provide fast and good estimate of the temperature dependence of elastic constants of BMGs.

BIBLIOGRAPHY

BIBLIOGRAPHY

Angell C.A., Spectroscopy simulation and scattering and the medium range order problem in glass, J. Non-Cryst. Solids 73 (1985) 1. (Angell, 1985).

Angell C.A., Formation of glasses from liquids and biopolymers, Science 267 (1995) 1924. (Angell, 1995).

Amiya K., Inoue A., Formation, thermal stability and mechanical properties of Ca-based bulk glassy alloys, Mater. Trans. JIM 43 (2002) 81. (Amiya, 2002a).

Amiya K., Inoue A., Formation and thermal stability of Ca-Mg-Ag-Cu bulk glassy alloys, Mater. Trans. JIM 43 (2002) 2578. (Amiya, 2002 b).

Arfken G., *Mathematical Methods for Physicists*, 2nd ed. (New York, Academic Press, 1970), 800. (Arfken, 1970).

Battezzati L., Is there a link between melt fragility and elastic properties of metallic glasses, Mat. Trans. JIM 46 (2005) 2915. (Battezzati, 2005).

Busch R., Liu W., Johnson W.L., Thermodynamics and kinetics of the $Mg_{65}Cu_{25}Y_{10}$ bulk metallic glass forming liquid, J. Appl. Phys. 83 (1998) 4134. (Busch, 1998).

Busch R., Masuhr A., Johnson W.L., Thermodynamics and kinetics of Zr-Ti-Cu-Ni-Be bulk metallic glass forming liquid, Mater. Sci. Eng. A 304-306 (2001) 97. (Busch, 2001).

Chen H.S., Thermodynamic considerations on the formation and stability of metallic glasses, Acta Metall. 22 (1974) 1505. (Chen, 1974).

Chen H.S., The influence of structural relaxation on the density and Young's modulus of metallic glasses, J. Appl. Phys. 49 (1978) 3289. (Chen, 1978).

Chu F., He Y., Thoma D.J., Mitchell T.E., Elastic constants of the C15 laves phase compound $NbCr_2$, Scr. Metall. Mater. 33 (1995) 1295. (Chu, 1995).

Conner R.D., Rosakis A.J., Johnson W.L., Owen D.M., Fracture toughness determination for a beryllium-bearing bulk metallic glass, Scr. Mater. 37 (1997) 1737. (Conner, 1997).

Debenedetti P.G., Stillinger F.H., Supercooled liquids and the glass transition, Nature 410 (2001) 260. (Debenedetti, 2001).

Demarest H.H. Jr., Cube-resonance method to determine the elastic constants of solids, J. Acoust. Soc. Am. 49 (1971) 768. (Demarest, 1971).

Drehman A.J., Greer A.L., Turnbull D., Bulk formation of a metallic glass: $Pd_{40}Ni_{40}P_{20}$, Appl. Phys. Lett. 41 (1982) 615. (Drehman, 1982).

Drehman A.J., Greer A.L., Kinetics of crystal nucleation and growth in $Pd_{40}Ni_{40}P_{20}$ glass, Acta Metall. 32 (1984) 323. (Drehman, 1984).

Du X.H., Huang J.C., Liu C.T., Lu Z.P., New criterion of glass forming ability for bulk metallic glasses, J. Appl. Phys. 101 (2007) 086108. (Du, 2007a).

Du X.H., Huang J.C., Hsieh K.C., Lai Y.H., Chen H.M., Jang J.S.C., Liaw P.K., Two-glassy-phase bulk metallic glass with remarkable plasticity, Appl. Phys. Lett. 91 (2007) 131901. (Du, 2007b).

Duan G., Lind M.L., Demetriou M.D., Johnson W.L., Goddard III W.A., Cagin T., Samwer K., Strong configurational dependence of elastic properties for a binary model metallic glass, Appl. Phys. Lett. 89 (2006) 151901. (Duan, 2006).

Duan G., Lind M.L., Blauwe K.D., Wiest A., Johnson W.L., Thermal and elastic properties of Cu-Zr-Be bulk metallic glass forming alloys, App. Phys. Lett. 90 (2007) 211901. (Duan, 2007).

Duan G., Blauwe K.D., Lind M.L., Schramm J.P., Johnson W.L., Compositional dependence of thermal, elastic and mechanical properties in Cu-Zr-Ag bulk metallic glasses, Scripta Mater. 58 (2008) 159. (Duan, 2008).

Egami T., Srolovitz D., Local structural fluctuations in amorphous and liquid metals: a simple theory of the glass transition, J. Phys. F: Met. Phys., 12 (1982) 2141. (Egami, 1982).

Egami T., Magnetic amorphous alloys: physics and technological applications, Rep. Prog. Phys. 47 (1984) 1601. (Egami, 1984).

Egami T., Universal criterion for metallic glass formation, Mater. Sci. Eng. A 226-228 (1997) 261. (Egami, 1997).

Egami T., Poon S.J., Zhang Z., Keppens V., Glass transition in metallic glasses: a microscopic model of topological fluctuations in the bonding network, Phys. Rev. B 76 (2007) 024203. (Egami, 2007).

Elliott H.A., An analysis of the conditions for rupture due to griffth cracks, Proc. Phys. Soc. 59 (1947) 208. (Elliott, 1947).

Fraser D.B., LeCraw R.C., Novel method of measuring elastic and anelastic properties of solids, Rev. Sci. Instrum. 35 (1964) 1113. (Fraser, 1964).

Fu H.M., Zhang H.F., Wang H., Hu Z.Q., Cu-based bulk amorphous alloy with larger glass-forming ability and supercooled liquid region, J. Alloys Compd. 458 (2008) 390. (Fu, 2008).

Fukuhara M., Wang X., Inoue A., Thermal elasticity in glassy alloys based on topology of metallic clusters, Appl. Phys. Lett. 91 (2007) 171908. (Fukuhara, 2007).

Fukuhara M., Kawashima A., Zhang W., Inoue A., Yin F., Low temperature dependence of elastic parameters and internal frictions for glassy alloy $Cu_{45}Zr_{45}Al_5Ag_5$, J. Appl. Phys. 103 (2008) 013503. (Fukuhara, 2008).

Fulcher G.S., Analysis of recent measurements of the viscosity of glasses, J. Am. Ceram. Soc. 8 (1925) 339. (Fulcher, 1925).

Gilbert C.J., Ritchie R.O., Johnson W.L., Fracture toughness and fatigue-crack propagation in a Zr-Ti-Ni-Cu-Be bulk metallic glass, Appl. Phys. Lett. 71 (1997) 476. (Gilbert, 1997).

Girifalco L.A., *Statistical Physics of Materials* (Wiley, New York, 1973, p78). (Girifalco, 1973).

Glade S.C., Busch R., Lee D.S., Johnson W.L., Thermodynamics of $Cu_{47}Ti_{34}Zr_{11}Ni_8$, $Zr_{52.5}Cu_{17.9}Ni_{14.6}Al_{10}Ti_5$ and $Zr_{57}Cu_{15.4}Ni_{12.6}Al_{10}Nb_5$ bulk metallic glass forming alloys, J. Appl. Phys. 87 (2000) 7242. (Glade, 2000).

Golding B., Bagley B.G., Hsu F.S.L., Soft transverse phonons in a metallic glass, Phys. Rev. Lett. 29 (1072) 68. (Golding, 1972).

Gorsse S., Orveillon G., Senkov O.N., Miracle D.B., Thermodynamic analysis of glass-forming ability in a Ca-Mg-Zn ternary alloys system, Phys. Rev. B 73 (2006) 224202. (Gorsse, 2006).

Greer A.L., Confusion by design, Nature 366 (1993) 303. (Greer, 1993).

Greer A.L., Metallic glasses, Science 267 (1995) 1947. (Greer, 1995).

Gu X., Jiao T., Kecskes L.J., Woodman R.H., Fan C., Ramesh K.T. and Hufnagel T.C., Crystallization and mechanical behavior of (Hf, Zr)-Ti-Cu-Ni-Al metallic glasses, J. Non-Cryst. Solids 317 (2003) 112. (Gu, 2003).

Gu X.J., McDermott A.G., Poon S.J. and Shiflet G.J., Critical Poisson's ratio for plasticity in Fe-Mo-C-B-Ln bulk amorphous steel, Appl. Phys. Letters 88 (2006) 211905. (Gu, 2006).

Guo F.Q., Poon S.J., Shiflet G.J., CaAl-based bulk metallic glasses with high thermal stability, Appl. Phys. Lett. 84 (2004) 37. (Guo, 2004).

Harms U., Jin O., Schwarz R.B., Effects of plastic deformation on the elastic modulus and density of bulk amorphous $Pd_{40}Ni_{40}Cu_{30}P_{20}$, J. Non-Cryst. Solids, 317 (2003) 200. (Harms, 2003).

Hecker S.S., Rohr D.L., Stein D.F., Brittle fracture in iridium, Metall. Trans. A 9 (1978) 481. (Hecker, 1978).

Hiki Y., Yagi T., Aida T., Takeuchi S., Low-frequency high-temperature internal friction of bulk metallic glasses, J. Alloys Compd. 355 (2003) 42. (Hiki, 2003).

Hiki Y., Tanahashi M., Takeuchi S., Temperature, frequency, and amplitude dependence of internal friction of metallic glass, J. Non-Cryst. Solids 354 (2008) 994. (Hiki, 2008).

Hruby A., Evaluation of glass-forming tendency by means of DTA, Czech. J. Phys. B 22 (1972) 1187. (Hruby, 1972).

Ichitsubo T., Kai S., Ogi H., Hirao M., Tanaka K., Elastic and anelastic behavior of $Zr_{55}Al_{10}Ni_5Cu_{30}$ bulk metallic glass around the glass transition temperature under ultrasonic excitation, Scripta Mater. 49 (2003) 267. (Ichitsubo, 2003).

Inoue A., Zhang T., Masumoto T., Al-La-Ni amorphous alloys with a wide supercooled liquid region, Mater. Trans. JIM 30 (1989) 965. (Inoue, 1989).

Inoue A., Zhang T. and Masumoto T., Zr-Al-Ni amorphous alloys with high glass transition temperature and significant supercooled liquid region, Mater. Trans., JIM 31 (1990) 177. (Inoue, 1990a).

Inoue A., Zhang T., Masumoto T., Production of amorphous cylinder and sheet of $La_{55}Al_{25}Ni_{20}$ alloy by a metallic mold casting method, Mater. Trans. JIM 31 (1990) 425. (Inoue, 1990 b).

Inoue A., Nakamura T., Nishiyama N., Masumoto T., Mg-Cu-Y bulk amorphous alloys with high tensile strength produced by a high-pressure die casting method, Mater. Trans. JIM 33 (1992) 937. (Inoue, 1992).

Inoue A., Zhang T., Nishiyama N., Ohba K., Masumoto T., Preparation of 16 mm diameter rod of amorphous $Zr_{65}Al_{7.5}Ni_{10}Cu_{17.5}$ alloy, Mater. Tran. JIM 34 (1993) 1234. (Inoue, 1993a).

Inoue A., Zhang T., Masumoto T., Glass-forming ability of alloys, J. Non-Cryst. Solids 156-158 (1993) 473. (Inoue, 1993b).

Inoue A., High strength bulk amorphous alloys with low critical cooling rates, Mater. Trans. JIM 36 (1995) 866. (Inoue, 1995).

Inoue A., Nishiyama N., Matsuda T., Preparation of bulk glassy $Pd_{40}Ni_{10}Cu_{30}P_{20}$ alloy of 40 mm in diameter by water quenching, Mater. Tran. JIM 37 (1996) 181. (Inoue, 1996).

Inoue A., Nishiyama N., Extremely low critical cooling rates of new Pd-Cu-Pd base amorphous alloys, Mater. Sci. Eng. A 226-228 (1997) 401. (Inoue, 1997a).

Inoue A., Nishiyama N., Kimura H., Preparation and thermal stability of bulk amorphous $Pd_{40}Cu_{30}Ni_{20}P_{20}$ alloy cylinder of 72 mm in diameter, Mater. Tran. JIM 38 (1997) 179. (Inoue, 1997b).

Inoue A., Zhang T., Koshiba H., Makino A., New bulk amorphous Fe-(Co,Ni)-M-B (M=Zr, Hf, Nb, Ta, Mo, W) alloys with good soft magnetic properties, J. Appl. Phys. 83 (1998) 6326. (Inoue, 1998).

Inoue A., Zhang T., Stabilization of supercooled liquid and bulk glassy alloys in ferrous and non-ferrous systems, J. Non-Cryst. Solids 250-252 (1999) 552. (Inoue, 1999).

Inoue A., Stabilization of metallic supercooled liquid and bulk amorphous alloys, Acta Mater. 48 (2000) 279. (Inoue, 2000).

Inoue A., Zhang W., Zhang T., Kurosaka K., High strength Cu-based bulk glassy alloys in Cu-Zr-Ti and Cu-Hf-Ti ternary systems, Acta Mater. 49 (2001) 2645. (Inoue, 2001a).

Inoue A., Zhang W., Zhang T., Kurosaka K., Formation and mechanical properties of Cu-Hf-Ti bulk glassy alloys, J. Mater. Res. 16 (2001) 2836. (Inoue, 2001b).

Inoue A., Takeuchi A., Recent progress in bulk glassy alloys, Mater. Tran. JIM 43 (2002) 1892. (Inoue, 2002).

Irwin G.R., Analysis of stresses and strains near end of crack traversing plaste, J. Appl. Mech. 24 (1957) 361. (Irwin, 1957).

Jiang F., Wang Y.D., Liaw P.K., Zhang Z., Keppens V., unpublished work. (Jiang, unpublished).

Johari G.P., On Poisson's ratio of glass and liquid vitrification characteristics, Philos. Mag. 86 (2006) 1567. (Johari, 2006).

Johnson W.L., Samwer K., A universal criterion for plastic yielding of metallic glasses with a $(T/T_g)^{2/3}$ temperature dependence, Phys. Rev. Lett. 95 (2005) 195501. (Johnson, 2005).

Kelly A., Tyson W.R., Cottrell A.H., Ductile and brittle crystals, Philos. Mag. 15 (1967) 567. (Kelly, 1967).

Kittel C., *Introduction to Solid State Physics*, 6th ed. (New York, Wiley, 1986). (Kittel, 1986).

Klement W., Willens R.H., Duwez P., Non-crystalline structure in solidified gold-silicon alloys, Nature 187 (1960) 869. (Klement, 1960).

Knott J.F. *Fundamentals of fracture mechanics*, (New York, Wiley, 1973), p108. (Knott, 1973).

Knuyt G., Schepper L.D., Stals L.M., Calculation of elastic constants for an amorphous metal and the influence of relaxation, J. Phys. F: Met. Phys. 16 (1986) 1989. (Knuyt, 1986).

Knuyt G., Stals L.M., Calculation of some metallic-glass properties, based on the use of a Gaussian distribution for the nearest-neighbour distance. III elastic constants, Philos. Mag. 64 (1991) 299. (Knuyt, 1991).

Kui W.H., Greer A.L., Turnbull D., Formation of bulk metallic glass by fluxing, Appl. Phys. Lett. 45 (1984) 615. (Kui, 1984).

Lee M.C., Kendall J.M., Johnson W.L., Spheres of the metallic glass $Au_{55}Pb_{22.5}Sb_{22.5}$ and their surface characteristics, Appl. Phys. Lett. 40 (1982) 382. (Lee, 1982).

Leisure R.G., Willis F.A., Resonant ultrasound spectroscopy, J. Phys.: Condens. Matter 9 (1997) 6001. (Leisure, 1997).

Lewandowski J.J., Wang W.H. and Greer A.L., Intrinsic plasticity or brittleness of metallic glasses, Philos. Mag. Lett. 85 (2005) 77. (Lewandowski, 2005).

Li S., Wang R.J., Pan M.X., Zhao D.Q., Wang W.H., Formation and properties of $RE_{55}Al_{25}Co_{20}$ (RE=Y, Ce, La, Pr, Nd, Gd, Tb, Dy, Ho and Er) bulk metallic glasses, J. Non-Cryst. Solids 354 (2008) 1080. (Li, 2008).

Lin H.M., Wu J.K., Wang C.C., Lee P.Y., The corrosion behavior of mechanically alloyed Cu-Zr-Ti bulk metallic glasses, Mater. Lett. 62 (2008) 2995. (Lin, 2008).

Lin X.H., Johnson W.L., Formation of Ti-Zr-Cu-Ni bulk metallic glasses, J. Appl. Phys. 78 (1995) 6514. (Lin, 1995).

Lind M.L., Duan G., Johnson W.L., Isoconfigurational elastic constants and liquid fragility of a bulk metallic glass forming alloy, Phys. Rev. Lett. 97 (2006) 015501. (Lind, 2006).

Liu C.T., Heatherly L., Easton D.S., Carmicheal C.A., Schneibel J.H., Chen C.H., Wright J.L., Yoo M.H., Horton J.A. and Inoue A., Test environments and mechanical properties of Zr-Base bulk amorphous alloys, Metall. Mater. Trans. A 29 A (1998) 1811. (Liu, 1998).

Loffler J.F., Bulk metallic glasses, Intermetallics 11 (2003) 529. (Loffler, 2003).

Lu Z.P., Liu C.T., A new glass-forming ability criterion for bulk metallic glasses, Acta. Mater. 50 (2002) 3501. (Lu, 2002).

Lu Z.P., Liu C.T., Glass formation criterion for various glass-forming systems, Phys. Rev. Lett. 91 (2003) 115505. (Lu, 2003).

Maeda S., Yamasaki T., Yokoyama Y., Okai D., Fukami T., Kimura H.M. and Inoue A., Viscosity measurements of $Zr_{55}Cu_{30}Al_{10}Ni_5$ and $Zr_{50}Cu_{40-x}Al_{10}Pd_x$ (x=0, 3 and 7 a.t.%) supercooled liquid alloys by using a penetration viscometer, Mater. Sci. Eng., A 449-451 (2007) 203. (Maeda, 2007).

Migliori A., Visscher W.M., Brown S.E., Fisk Z., Cheong S.W., Alten B., Ahrens E.T., Kubat-Martin K.A., Maynard J.D., Huang Y., Kirk D.R., Gillis K.A., Kim H.K., Chan M.H.W., Elastic constants and specific-heat measurements on single crystals of La_2CuO_4, Phys. Rev. B 41 (1990) 2098. (Migliori, 1990a).

Migliori A., Visscher W.M, Wong S., Brown S.E., Tanaka I., Kojima H., Allen P.B., Complete elastic constants and giant softening of c_{66} in superconducting $La_{1.86}Sr_{0.14}CuO_4$, Phys. Rev. Lett. 64 (1990) 2458. (Migliori, 1990b).

Migliori A., Sarrao J.L., Visscher W.M., Bell T.M., Lei M., Fisk Z., Leisure R.G., Resonant ultrasound spectroscopic techniques for measurement of the elastic moduli of solids, Physica B 183 (1993) 1. (Migliori, 1993).

Migliori A., Sarrao J.L., *Resonant Ultrasound Spectroscopy: Applications to Physics, Materials Measurements and Nondestructive Evaluation*, (New York, Wiley, 1997). (Migliori, 1997).

Mohazzabi P., Behroozi F., Thermal expansion of solids: a simple classical model, Eur. J. Phys. 18 (1997) 237. (Mohazzabi, 1997).

Murty B.S., Hono K., Formation of nanocrystalline particles in glassy matrix in melt-spun Mg-Cu-Y based alloys, Mater. Tran. JIM 41 (2000) 1538. (Murty, 2000).

Nascimento M.L.F., Souza L.A., Ferreira E.B., Zanotto E.D., Can glass stability parameters infer glass forming ability, J. Non-Cryst. Solids 351 (2005) 3296. (Nascimento, 2005).

Novikov V.N., Sokolov A.P., Poisson's ratio and the fragility of glass-forming liquids, Nature 431 (2004) 961. (Novikov, 2004).

Novikov V.N., Sokolov A.P., Correlation of fragility and Poisson's ratio: difference between metallic and nonmetallic glass formers, Phys. Rev. B 74 (2006) 064203. (Novikov, 2006).

Ohno I., Free vibration of a rectangular parallelepiped crystal and its application to determination of elastic constants of orthorhombic crystals, J. Phys. Earth 24 (1976) 355. (Ohno, 1976).

Okai D., Nanbu A., Fukami T., Yamasaki T., Zhang T., Yokoyama Y., Motoyama G., Oda Y., Kimura H.M., Inoue A., Temperature dependence of electrical resistivity of Zr-Cu-Al-Ni-Nb bulk metallic glasses below 300 K, Mater. Sci. Eng. A 449-451 (2007) 548. (Okai, 2007).

Okuda H., Murase I., Kurosaki R., Nakagawa E., Oshiai S., Yokoyama Y., Saida J., Inoue K., Nanoscopic fluctuation in quenched Zr-Cu-Ni-Al metallic glasses and their welds examined by ASAXS at Zr-K edge, Intermetallics 14 (2006) 1038. (Okuda, 2006).

Park E.S., Kim D.H., Formation of Ca-Mg-Zn bulk glassy alloy by casting into cone-shaped copper mold, J. Mater. Res. 19 (2004) 685. (Park, 2004).

Park E.S., Kim W.T., Kim S.H., Effect of alloy composition on the glass forming ability in Ca-Mg-Zn alloys system, Mater. Sci. Forum 475-479 (2005) 3415. (Park, 2005).

Peker A. and Johnson W.L., A highly processable metallic glass: $Zr_{41.2}Ti_{13.8}Cu_{12.5}Ni_{10.0}Be_{22.5}$, Appl. Phys. Lett. 63 (1993) 2342. (Peker, 1993).

Peter W.H., Liaw P.K., Buchanan R.A., Liu C.T., Brooks C.R., Horton Jr. J.A., Carmicheal Jr. C.A.and Wright J.L., Fatigue behavior of $Zr_{52.5}Al_{10}Ti_5Cu_{17.9}Ni_{14.6}$ bulk metallic glass, Intermetallics 10 (2002) 1125. (Peter, 2002).

Pugh S.F., Relations between the elastic moduli and the plastic properties of polycrystalline pure metals, Philos. Mag. 45 (1954) 823. (Pugh, 1954).

Qiao D.C., Fan G.J., Liaw P.K., Choo H., Fatigue behaviors of the $Cu_{47.5}Zr_{47.5}Al_5$ bulk-metallic glass (BMG) and $Cu_{47.5}Zr_{38}Hf_{9.5}Al_5$ BMG composite, Int. J. Fatigue 29 (2007) 2149. (Qiao, 2007).

Rice J.R., Thomson R., Ductile versus brittle behavior of crystals, Philo. Mag. 29 (1974) 73. (Rice, 1974).

Schreiber E., Anderson O.L., Sogat N., Warren N., Scholz C., Sound velocity and compressibility for lunar rocks 17 and 46 and for glass spheres from the lunar soil, Science 167 (1970) 732. (Schreiber, 1970a).

Schreiber E., Anderson O.L., Properties and composition of lunar materials: earth analogies, Science 26 (1970) 1579. (Schreiber, 1970b).

Schreiber E., Anderson O.L., Soga N., *Elastic Constants and Their Measurements*, Mc Graw-Hill, New York, 1974. (Schreiber, 1974).

Schroers J. and Johnson W.L., Ductile bulk metallic glass, Phys. Rev. Lett. 93 (2004) 255506. (Schroers, 2004).

Senkov O.N. Scott J.M., Specific criteria for selection of alloy compositions for bulk metallic glasses, Scr. Mater. 50 (2004) 449. (Senkov, 2004a).

Senkov O.N., Scott J.M., Formation and thermal stability of Ca-Mg-Zn and Ca-Mg-Zn-Cu bulk metallic glasses, Mater. Lett. 58 (2004) 1375. (Senkov, 2004 b).

Senkov O.N., Scott J.M., Glass forming ability and thermal stability of ternary Ca-Mg-Zn bulk metallic glasses, J. Non-Cryst. Solids 351 (2005) 3087. (Senkov, 2005).

Senkov O.N., Miracle D.B., Scott J.M., Development and characterization of Ca-Mg-Zn-Cu bulk metallic glasses, Intermetallics 14 (2006) 1055. (Senkov, 2006).

Senkov O.N., Correlation between fragility and glass-forming ability of metallic alloys, Phys. Rev. B 76 (2007) 104202. (Senkov, 2007).

Shelby J.E., *Introduction to Glass Science and Technology*, Royal Society of Chemistry, Cambridge, 1997. (Shelby, 1997).

Shen T.D., He Y., Schwarz R.B., Bulk amorphous Pd-Ni-Fe-P alloys: preparation and characterization, J. Mater. Res. 14 (1999) 2107. (Shen, 1999a).

Shen T.D., Schwarz R.B., Bulk ferromagnetic glasses prepared by flux melting and water quenching, Appl. Phys. Lett. 75 (1999) 49. (Shen, 1999b).

Suzuki Y., Egami T., Shear deformation of glassy metals: breakdown of Cauchy relationship and anelasticity, J. Non-Cryst. Solids, 75 (1985) 361. (Suzuki, 1985).

Tammann G., Glasses as supercooled liquids, J. Glass Techno. Soc. 35 (1925) 166. (Tammann, 1925).

Tanaka H., Relationship among glass-forming ability, fragility and short-range bond ordering of liquids, J. Non-Cryst. Solids 351 (2005) 678. (Tanaka, 2005).

Tarumi R., Ogi H., Hirao M., Ichitsubo T., Matsubara E., Saida J., Low-temperature acoustic properties and quasiharmonic analysis for Cu-based bulk metallic glasses, Mater. Sci. Forum 539-543 (2007) 1932. (Tarumi, 2007).

Turnbull D., Under what conditions can a glass be formed, Contemp. Phys. 10 (1969) 473. (Turnbull, 1969).

Varshni Y.P., Temperature dependence of the elastic constants, Phys. Rev. B 2 (1970) 3952. (Varshni 1970).

Visscher W.M., Migliori A., Bell T.M. Reinert R.A., On the normal modes of free vibration of inhomogeous and anisotropic elastic objects, J. Acoust. Soc. Am. 90 (1991) 2154. (Visscher, 1991).

Vogel H., The law of viscosity change with temperature, Phys. Zeit. 22 (1921) 645. (Vogel, 1921).

Wang G.Y., Liaw P.K., Peter W.H., Yang B., Freels M., Yokoyama Y., Benson M.L., Green B.A., Saleh T.A., McDaniels R.L., Steward R.V., Buchanan R.A., Liu C.T., and

Brooks C.R., Fatigue behavior and fracture morphology of $Zr_{50}Al_{10}Cu_{40}$ and $Zr_{50}Al_{10}Cu_{30}Ni_{10}$ bulk-metallic glasses, Intermetallics 12 (2004) 1219. (Wang, 2004a).

Wang G.Y., Liaw P.K., Peter W.H., Yang B., Yokoyama Y., Benson M.L., Green B.A., Kirkham M.J., White S.A., Saleh T.A., McDaniels R.L., Steward R.V., Buchanan R.A., Liu C.T.and Brooks C.R., Fatigue behavior of bulk-metallic glasses, Intermetallics 12 (2004) 885. (Wang, 2004 b).

Wang G.Y., Liaw P.K., Yokoyama Y., Peker A., Peter W.H., Yang B., Freels M., Zhang Z.Y., Keppens V., Hermann R., Buchanan R.A., Liu C.T., Brooks C.R., Studying fatigue behavior and Poisson's ratio of bulk-metallic glasses, Intermetallics 15 (2007) 663. (Wang, 2007).

Wang G.Y., Liaw P.K., Yokoyama Y., unpublished work. (Wang, unpublished).

Wang L.M., Wang W.H., Wang R.J., Zhan Z.J., Dai D.Y., Sun L.L., Wang W.K., Ultrasonic investigation of $Pd_{39}Ni_{10}Cu_{30}P_{21}$bulk metallic glass upon crystallization, Appl. Phys. Lett. 77 (2000) 1147. (Wang, 2000).

Wang R.J., Li F.Y., Wang J.F., Wang W.H., Response of glassy structure and properties to pressure and devitrification, Appl. Phys. Lett. 83 (2003) 2814. (Wang, 2003a)

Wang W.H., Wang R.J., Li F.Y., Zhao D.Q., Pan M.X., Elastic constants and their pressure dependence of $Zr_{41}Ti_{14}Cu_{12.5}Ni_9Be_{22.5}C_1$ bulk metallic glass, Appl. Phys. Lett. 74 (1999) 1803. (Wang, 1999).

Wang W.H., Wen P., Zhao D.Q., Pan M.X., Wang R.J., Relationship between glass transition temperature and Debye temperature in bulk metallic glasses, J. Mater. Res. 18 (2003) 2747. (Wang, 2003b).

Wang W.H., Dong C. and Shek C.H., Bulk metallic glasses, Mater. Sci. and Eng. R 44 (2004) 45. (Wang, 2004 c).

Wang W.H., Elastic moduli and behaviors of metallic glasses, J. Non-Cryst. Solids 351 (2005) 1481. (Wang, 2005).

Wang W.H., Correlations between elastic moduli and properties in bulk metallic glasses, J. Appl. Phys. 99 (2006) 093506. (Wang, 2006).

Waniuk T.A., Schroers J., Johnson W.L., Critical cooling rate and thermal stability of Zr-Ti-Cu-Ni-Be alloys, Appl. Phys. Lett. 78 (2001) 1213. (Waniuk, 2001).

Wesseling P., Nieh T.G., Wang W.H., Lewandowski J.J., Preliminary assessment of flow, notch toughness, and high temperature behavior of $Cu_{60}Zr_{20}Hf_{10}Ti_{10}$ bulk metallic glasses, Scripta Mater. 51 (2004) 151. (Wesseling, 2004).

Xi X.K., Zhao D.Q., Pan M.X., Wang W.H., Wu Y., Lewandowski J.J., Fracture of brittle metallic glasses: brittleness or plasticity, Phys. Rev. Lett. 94 (2005) 125510. (Xi, 2005).

Yang K.W., Jia E.G., Shui J.P., Zhu Z.G., Crystallization study of amorphous $Pd_{43}Ni_{10}Cu_{27}P_{20}$ alloy by internal friction measurement, Phys. Stat. Sol. A 204 (2007) 3297. (Yang, 2007).

Yannopoulos S.N., Johari G.P., Poisson's ratio and liquid's fragility, Nature 443 (2006) E7. (Yannopoulos, 2006).

Yokoyama Y., Fukaura K. and Inoue A., Cast structure and mechanical properties of Zr-Cu-Ni-Al bulk glassy alloys, Intermetallics 10 (2002) 1113. (Yokoyama, 2002).

Yokoyama Y., Ductility improvement of Zr-Cu-Ni-Al glassy alloy, J. Non-Cryst. Solids 316 (2003) 104. (Yokoyama, 2003).

Yokoyama Y., Fukaura K., Inoue A., Formation and mechanical properties of Zr-Cu-Al bulk glassy alloys, Mater. Sci. Eng. A 375-377 (2004) 427. (Yokoyama, 2004).

Yokoyama Y., Yamasaki T., Liaw P.K., Buchanan R.A., Inoue A., Glass-structure changes in tilt-cast Zr-Cu-Al glassy alloys, Mater. Sci. Eng. A 449-451 (2007) 621. (Yokoyama, 2007).

Zhang B., Wang R.J., Zhao D.Q., Pan M.X., Wang W.H., Properties of Ce-based bulk metallic glass-forming alloys, Phys. Rev. B 70 (2004) 224208. (Zhang, 2004).

Zhang B., Wang R.J., Wang W.H., Response of acoustic and elastic properties to pressure and crystallization of Ce-based bulk metallic glass, Phys. Rev. B 72 (2005) 104205. (Zhang, 2005).

Zhang T., Inoue A. and Masumoto T., Amorphous Zr-Al-TM (TM=Co, Ni, Cu) alloys with significant supercooled liquid region of over 100 K, Mater. Trans., JIM 31 (1991) 1005. (Zhang, 1991).

Zhang Y., Greer A.L., Correlations for predicting plasticity or brittleness of metallic glasses, J. Alloys Compd. 434-435 (2007) 2. (Zhang, 2007a).

Zhang Z., Wang R.J., Xia L., Wei B.C., Zhao D.Q., Pan M.X. and Wang W.H., Elastic behaviour and microstructural characteristics of $Nd_{60}Al_{10}Fe_{20}Co_{10}$ bulk metallic glass investigated by ultrasonic measurement under pressure, J. Phys.: Condens. Matter. 15 (2003) 4503. (Zhang, 2003).

Zhang Z., Keppens V., Liaw P.K., Yokoyama Y. and Inoue A., Elastic properties of Zr-based bulk metallic glasses studied by resonant ultrasound spectroscopy, J. Mater. Res. 22 (2007) 364. (Zhang, 2007b).

Zhang Z., Keppens V., Senkov O.N., Miracle D.B., Elastic properties of Ca-based bulk metallic glasses studied by resonant ultrasound spectroscopy, Mater. Sci. Eng., A 471 (2007) 151. (Zhang, 2007c).

VITA

Zhiying Zhang was born on June 13, 1977 in Honghu City, Hubei Province, China. After graduating from Honghu City No.1 High School, she entered Beijing University of Aeronautics and Astronautics in 1993. She obtained Bachelor degree in Corrosion and Protection in 1997 and Master degree in Materials Science in 2000. Then she studied in University of Alberta, Canada and obtained Master degree in Materials Engineering in 2003. After graduation, she worked in China Academy of Railway Sciences, Metals and Chemistry Research Institute. She started Ph. D. study in University of Tennessee, Knoxville in 2004 and obtained Ph. D. degree in Materials Science and Engineering in 2008.